A University of Sussex PhD thesis

Available online via Sussex Research Online:

http://sro.sussex.ac.uk/

UNIVERSITY OF SUSSEX

PHD THESIS

Long range coherence of Bose gases in variable dimensionality

Author:
Robert SHAH

Supervisors:
Dr F. ORUČEVIĆ
Professor P. KRÜGER

Examiners:
Professor T. SCHUMM
Professor J. DUNNINGHAM

US

**UNIVERSITY
OF SUSSEX**

*A thesis submitted in fulfilment of the requirements
for the degree of Doctor of Philosophy*

in the

Quantum Systems and Devices Group
School of Mathematical and Physical Sciences

April 2021

Declaration of Authorship

I hereby declare that this thesis has not been and will not be, submitted in whole or in part to another University for the award of any other degree.

Signed:

_____

Date: 30/04/2021

_____

Long range coherence of Bose gases in variable dimensionality

Robert SHAH

Abstract

This thesis reports on our experimental investigation into the properties of condensed Bose gases across the 1D-3D regime. We review known theoretical models of quasi-condensates (1D) and the less understood crossover regime (the 3D regime being the Bose-Einstein condensate) and test them against our experimental findings. We use density ripples (a well-known phenomenon that occurs in quasi-condensates) as a tool to probe phase coherence of gases across the 1D-3D crossover. We have compared our results with simulations based on the theoretical models and find evidence that supports a hybrid model. There are a number of candidates (aspect ratio of the trapping potential, and dimensionless energies of chemical potential and temperature) proposed that determine "1D-ness" which we investigate and propose that the dimensionless chemical potential parameter is the most important. The experiment we have built also contains novel additions such as atom trapping printed circuit boards and 3D printed structures, which I report on this thesis.

Acknowledgements

There are many people I'd like thank who helped me through the past four years and made this all possible. First I'd like to thank my supervisors Peter and Fedja for supporting me through my studies, and also answering my physics questions no matter how stupid, or wherever the location, be it lab, pub, or airport! You're both great teachers, and I am very grateful for the time I've spent working with you two. Peter I have to give extra thanks for also supervising me through my undergraduate (even through unpromising times..), and giving me the chance to take on a PhD.

Big shout out to Tom, the amount of time you've given to talk me through things has been immense. I still get surprised by the random bits of knowledge you've acquired, from electronics to Fourier analysis to Alan Partridge quotes. To Mark and Will the QSDCC thank you, I look forward to playing Will's left arm slow soon, probably not Mark's smelly swing though. Julia big thank you for the massive help in setting up the Green lab, and also your rum parties! To the rest of QSD, thanks for putting up with my eccentricities no matter how loud, you've all been good friends as well as colleagues.

To Em my partner, thank you for being there this whole time, putting up with me moving down south - the land of not enough gravy, during all the physics and football conversations in the pub, and my many manic moments. I am lucky to have you in my life.

To my sisters, thank you for reminding me when my beard needs a trim. Finally to my parents, Nick and Sue, thank you for everything, without your care and support I'm not sure I would have ever been interested in Physics.

To COVID-19 please dial 0121 do 1.

Contents

Chapter 1

Introduction

Physical systems in low dimensions (one or two-dimensions, 1D/2D) can display highly intriguing behaviour, their properties can be dramatically different to their three-dimensional (3D) counterpart. Theoretically low-dimensional systems are interesting as they often simplify the 3D model and can lead to analytical solutions. Application of the famous Bethe-ansatz [1] is one such example, which was created to solve the 1D Heisenberg model, allowing the exact eigenvalues and eigenvectors to be calculated. Since its original application, the Bethe-ansatz has been extended to a number of other 1D systems, including systems that can be realised in ultracold atom experiments.

In the past two decades ultracold atom experiments have allowed us to experimentally study low-dimensional systems in the many-body quantum regime, by using the phenomenon of Bose-Einstein condensation (BEC). This gives rise to coherent states of matter where the thermal de Broglie wavelength of individual particles becomes larger than their separation, forming a single macroscopic wavefunction, and is considered the matterwave equivalent of a single mode laser. BECs composed of dilute vapours of alkali atoms were first realised in 1995 [2–4]. These first experiments produced examples of three-dimensional condensates. Later, confining potentials were manipulated such that examples of two-[5–8] and one-dimensional gases [5, 9–13] were realised, however at finite temperature such systems do not display long range order and cannot be called true Bose-Einstein condensates (though at zero temperature formation of a BEC is possible in 2D systems) [14]. These systems are however quantum degenerate and display properties akin to a BEC, and for this reason they have been named quasi-condensates. In 2D there exists a superfluid phase transition at sufficiently low temperature known as the Berezinskii–Kosterlitz–Thouless (BKT) transition [15], and 1D systems can posses the property of superfluidity at zero temperature [16].

Understanding the coherence properties in low dimensional Bose gases, is not only interesting in the field itself, but can provide insight into other areas of research such as high temperature superconductors where in certain scenarios coherence can be increased in reduced dimensions [17]. A feature of quasi-condensates is the fluctuation of phase and/or density, it has been pointed out that such systems display behaviour analogous to the fluctuations observed during the early expansion of the

universe [18, 19]. This thesis focuses on 1D and 3D systems, and how they transition from one or the other. The crossover regime between 1D and 3D is of significant interest as many atom chip [20] experiments often will produce condensates within this regime. Due to the geometry of trapping the trapping wires, atom chips lend themselves towards "1D-like" cigar shaped potentials (long axially, but short in the transverse direction). Even though this regime is commonly encountered experimentally, to the best of our knowledge a thorough experimental study throughout chemical crossover has not been reported.

In 1968 Elliott H. Lieb and Werner Liniger, used the Bethe-ansatz to solve a 1D model of Bosons with repulsive contact interactions, now known as the Lieb-Liniger model [21, 22]. Whilst early interest in this model was purely academic it became of particular interest recently as it was possible to recreate such a system in the laboratory with ultracold atoms. One of the intriguing properties of the 1D system is that the interactions actually increase with decreasing density. The interaction strength in this model is characterised by the dimensionless quantity γ, now more famously known as the Lieb-Liniger parameter. With this parameter the model defines two regimes, the strongly interacting regime $\gamma > 1$, and the weakly interacting regime $\gamma \ll 1$. In the strongly interacting regime, the repulsive interactions are so strong that atoms can no longer share the same position and "fermionisation" occurs. The systems operating in such particular regime are known as Tonk-Girardeau gases [23], and were experimentally realised in [9, 10]. The 1D Bose-gas model was also solved for finite-temperature at equilibrium with the Yang-Yang formalism [24], via the application of a thermodynamic Bethe-ansatz. It was found to accurately predict the density profile of a 1D gas in equilibrium [25], and density fluctuations in the strong [26] and weakly [27, 28] interacting regimes.

From early theoretical studies in 1967 phase fluctuations were expected to be present in 1D quasi-condensates [29, 30], in contrast to a true condensate where the phase does not fluctuate. Much later in 2001 similar behaviour was predicted to occur in elongated 3D condensates (long in the axial dimension and short in the transverse dimensions) [31]. It was found that whilst a system may be considered 3D in the sense that there are transverse degrees of freedom, the phase can fluctuate over length scales (the phase coherence length l_ϕ) shorter than the axial length of the gas. Phase-fluctuating elongated 3D condensates were observed experimentally that same year [32, 33], and later in other early experimental studies (early 2000s) [13, 34–37]. The research reported in this thesis investigates the change in coherence as a 3D system transforms into 1D, through indirect measurements of the phase fluctuations. We manipulate the cloud parameters, atom number, temperature, and trapping potential, and examine the parameters that drive changes to the coherence throughout the 3D-1D crossover. We also study the effect of interactions during time of flight, an effect which is known to interfere with the measurement process but presumed negligible in 1D. We ascertain that the effect of interactions are significant towards the

3D regime and that they are qualitatively reproduced by the theoretical predictions of [32, 33]. Intriguingly we find that previously accepted "1D parameters" (aspect ratio λ, the ratio of system size to thermal phase coherence length L/λ_T, thermal transverse degeneracy $k_\text{B}T/\hbar\omega_\perp$, and chemical transverse degeneracy $\mu/\hbar\omega_\perp$) do not all appear to be important in driving the crossover and, perhaps most interestingly, we observe $k_\text{B}T/\hbar\omega_\perp$ to be weakly correlated. Our findings are important to experiments that desire or require fully coherent gases, such as atom interferometers and atom optics, and may have more far reaching significance in other fields where dimensionality is studied.

1.1 Overview

The aim of this thesis was to experimentally map out the 3D-1D crossover regime, and understand the controlling parameters, and assess the validity of known theoretical models. At the start of my PhD the group had just moved over from the University of Nottingham, and so the experiment was built from scratch. Much of the design was based on the previous experiment in Nottingham, and details of this set-up can be found in Dr Thomas Barrett's thesis [38]. Also, Dr William Evans was the major contributor in the design and installation of the control system and the 2D MOT, his work can be found in his thesis [39]. Here, I will summarise the content of my thesis.

Chapter 2 presents an overview of the essential theoretical background. It is split into two parts, first we focus on the important experimental techniques required to produce a BEC in the laboratory. Second, we discuss the important the physics relevant to the experiment performed in Chapter 4, we look into the coherence properties of Bose gases in three and one dimensions, and the fluctuations that arise in these systems.

Chapter 3 gives details on the experimental set-up. A substantial amount of time was spent building the experiment during the course of my PhD, hence this chapter will be large contribution to the content of my thesis. It includes my significant contributions to the set-up, and features that are relevant to the measurements taken in Chapter 4.

Chapter 4, in this chapter the main experimental results are presented, the details of the acquisition and analysis procedure are included. Along with the measurements, four different theoretical models are described, each model is incorporated into a simulation and their results are compared to experimental measurements. A discussion of the results and our findings is given at the end of this chapter.

Chapter 5 summarises the work conducted in this thesis, and also provides an outlook, including potential improvements and possible extensions to this research.

Chapter 2

Bose-Einstein condensation and phase coherence

This chapter first gives an overview of the fundamental principles behind magnetic trapping and cooling of neutral atoms, these are important techniques that allow us to produce Bose-Einstein condensates (BEC) in the laboratory. A vital step in the experimental process is laser cooling which is a precursor to evaporative cooling, however as this is not directly relevant to the experimental study in Chapter 4 it is not included in this chapter and instead I refer to the literature [40–42]. Next I discuss some of the important properties of a BEC, in particular the coherence properties. The experiment in this thesis also investigates gases that are not true BECs but condensation-like behaviour occurs, for this reason these gases are referred to as quasi-condensates. The final part of this chapter describes the different regimes of quasi-condensation, how they can be created experimentally, and how their properties differ.

2.1 Classical to quantum gases

This section addresses the theoretical background to the experimental steps that are required to transfer a gas of atoms from a classical state into a quantum degenerate state. First I will describe the interaction between atoms and magnetic fields, and how a trapping potential can be formed. I will then discuss how 3D trapping structures have been mapped onto planar devices. Then the evaporative cooling process will be described, and finally, I will outline the quantum degenerate state known as a Bose-Einstein condensate, and some of its important features.

2.1.1 Magnetic trapping

First, in order to produce a BEC from an atomic gas, one must select a suitable atom. Alkali metals are a popular choice amongst ultracold atom experiments, located in group one of the periodic table they have one valence electron and an odd number of protons in the nucleus. Isotopes with an even number of neutrons will then combine to form a composite boson. The single valence electron occupies an outer s-orbital

above a number of closed shells, this validates use of a relatively simple model of energy levels. Notably the electronic ground and excited states can be addressed with optical frequencies, meaning powerful techniques such as laser cooling [43] and absorption imaging 3.3.1 can be used. Nowadays the appropriate lasers are commercially available. Secondly the interaction of the electron's magnetic moment with a static magnetic field is strong enough to make magnetic trapping feasible. Our experiment uses ^{87}Rb atoms, the electronic structure is shown in Fig. 2.1.
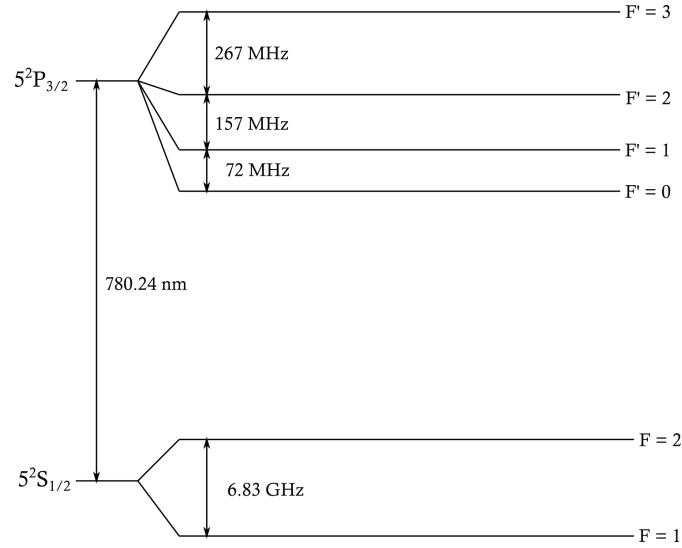
FIGURE 2.1: ^{87}Rb D$_2$ line [44]. The ground to excited state transition is $5^2S_{1/2} \rightarrow 5^2P_{3/2}$, the corresponding wavelength $\lambda = 780.24$ nm.

Other commonly used alkali atoms include, ^{7}Li, ^{23}Na, ^{39}K, ^{41}K, ^{85}Rb, and ^{133}Cs [45]. In this section we are concerned with the interaction with a static magnetic field **B**. The Hamiltonian is [42],

$$H_B = -\boldsymbol{\mu} \cdot \mathbf{B} \tag{2.1}$$

where μ is the total magnetic moment of the atom given by,

$$\boldsymbol{\mu} = -\frac{g_J \mu_B}{\hbar} \mathbf{J} + \frac{g_I \mu_N}{\hbar} \mathbf{I}. \tag{2.2}$$

Here, $\mathbf{J} = \mathbf{L} + \mathbf{S}$ is the total electron angular momentum, the sum of the orbital **L** and spin **S** angular momenta, μ_B and μ_N are the Bohr and nuclear magnetons, g_J is the Landé g-factor, and g_N is the nuclear g-factor. Since $\mu_B \gg \mu_N$ the second term in Eq. (2.2) can typically be neglected for describing magnetic trapping experiments. If the field interaction is smaller than the hyperfine interaction $A_{\text{hfs}}\mathbf{I} \cdot \mathbf{J}$ (where A_{hfs} is the magnetic dipole constant for Rb^{87} in the 5^2S$_{1/2}$ state $A_{\text{hfs}} = h \cdot 3.417$ GHz) then m_I and m_J are not good quantum numbers, but F ($\mathbf{F} = \mathbf{J} + \mathbf{I}$) and m_F are [42]. The total angular momentum **F** precesses about the magnetic field which we will define along

the z-axis, projecting $\mathbf{J}$ along $\mathbf{F}$ we get the result,

$$H_B = \frac{g_F \mu_B}{\hbar} B_z F_z, \tag{2.3}$$

where,

$$g_F = g_J \frac{F(F+1) - I(I+1) + J(J+1)}{2F(F+1)}. \tag{2.4}$$

Calculating the the expectation value of Eq. (2.3) we get arrive at the weak field *Zeeman Effect*,

$$\langle F, m_F | H_B | F, m_F \rangle = \Delta E_B = g_F m_F \mu_B B_z. \tag{2.5}$$

The frequency of precession about the magnetic field is the Larmor frequency $\omega_L = \mu_B B/\hbar$, if this is much faster than the change in direction of the field the magnetic moment will follow the direction of the field adiabatically [46] and the energy shift will be proportional to field strength $\Delta E_B = g_F m_F \mu_B |\mathbf{B}|$. In the presence of a spatially varying field then atoms with $g_F m_F \neq 0$ will experience a force $\propto \frac{\mathrm{d}B}{\mathrm{d}z}$, atoms with $g_F m_F > 0$ are often referred to as low field seekers and atoms with $g_F m_F < 0$ high field seekers. Wing's theorem [47] states that for a static magnetic field in source free space it is possible to have a field minimum, however field maxima are forbidden. This means that only low field seekers can be trapped (high seekers can be held in a stable orbit about a source, known as a Kepler trap [46]), in our experiment the atoms are in the $5^2S_{1/2} |F = 2, m_F = +2\rangle$ state (see Fig. 2.1) for which $g_F = 1/2$.
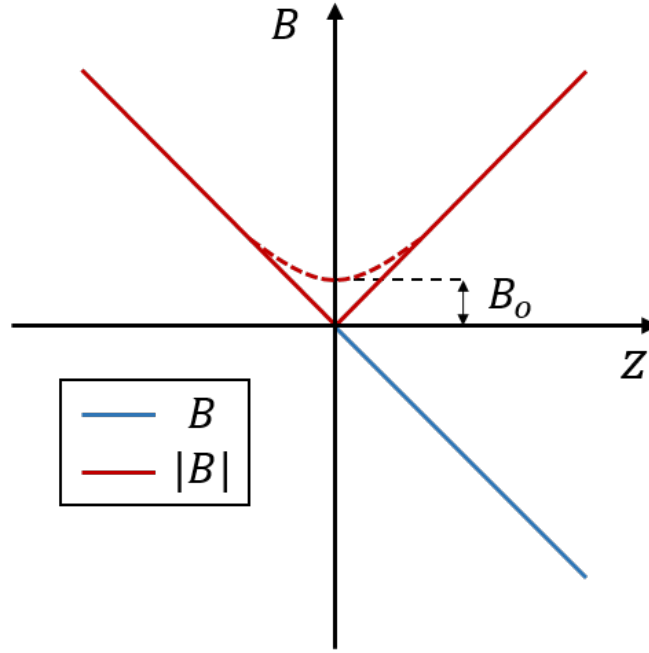
FIGURE 2.2: A plot showing the potential seen by a low field seeking atom. The magnetic field has a constant linear gradient that changes direction at the position $z = 0$, as the potential is proportional to $|B_z|$ the atom would see the red line and be attracted towards the position $z = 0$. To avoid Majorana transitions a constant offset field is applied in a direction perpendicular to the z-axis.

To trap low field seekers we need to create a minimum in magnetic field, Fig. 2.2 is a simple schematic that shows how field passing through zero can create a trapping potential. Note that at zero field the m_F states become degenerate and atoms can transition to non-trapped m_F states, to prevent this an additional offset field B_0 is used to "plug the hole". This must be in a direction perpendicular to z as any additional field along z would only move the zero point. The originally linear trap becomes harmonic at the minimum, and hence can be characterised by a frequency ω_z. For the adiabaticity condition to remain valid $\omega_z \ll \omega_L$, otherwise the atom's magnetic moment cannot follow the change in field direction and will project onto a different m_F state and potentially become untrapped, this is a type of spin-flip loss is known as a *Majorana transition* [48]. As a rule of thumb experimentalists often set the offset field to a minimum of $\sim 1\,\text{G}$, this ensures that the trap bottom is not resonant with typical sources of ambient laboratory noise. Another less common method that avoids Majorana transitions uses a time-orbiting potential or TOP trap, the first experimental observation of a BEC used such a configuration [2]. The basic principle of the technique is that by rapidly moving the position of the zero point, the atom sees a time averaged effective potential without a zero point. The principle of creating a non-zero minimum in the magnitude of magnetic field $|\mathbf{B}|$, underpins almost all of the trapping configurations employed in our laboratory.

Ioffe-Pritchard trap

Most ultracold atom experiments that utilise magnetic traps have field configurations based on the Ioffe-Pritchard (IP) trap [49]. The field configuration for an IP trap is given by the following [50],

$$
\mathbf{B}(x, y, z) = B_0 \begin{pmatrix} 0 \\ 0 \\ 1 \end{pmatrix} + \frac{B''}{2} \begin{pmatrix} -xz \\ -yz \\ z^2 - \frac{1}{2}\left(x^2 + y^2\right) \end{pmatrix} + B' \begin{pmatrix} x \\ -y \\ 0 \end{pmatrix},
$$

where the first two terms contains the axial confinement (z-axis) shown in Fig. 2.3a, and the last term is a 2D quadrupole that provides radial confinement ($x - y$ plane) and can be seen in Fig. 2.3b.
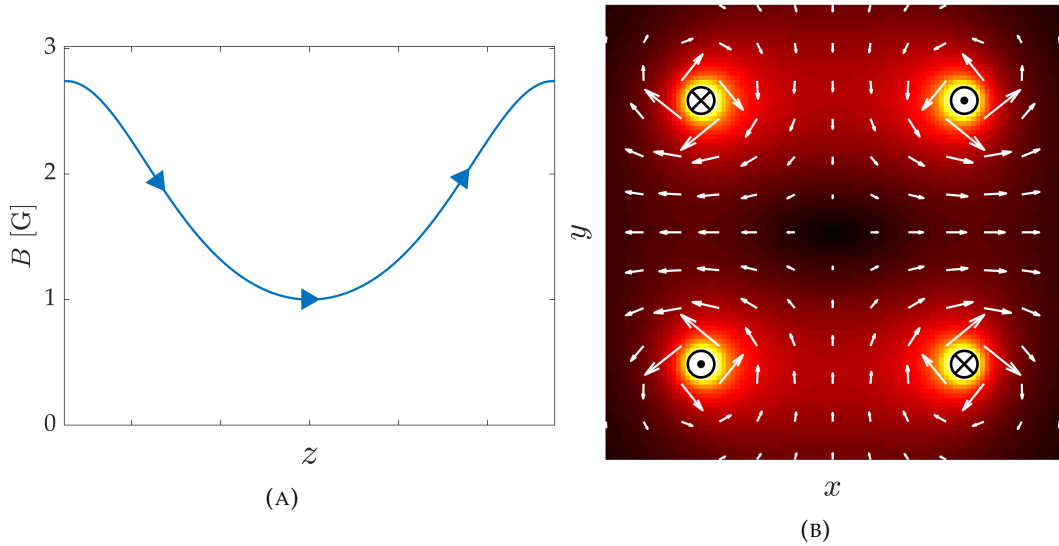
FIGURE 2.3: (A) Axial confinement provided by two coils running in parallel separated by a distance larger than their radius. This also provides the offset field B_0 to prevent Majorana transitions, and its direction defines a quantisation axis often referred to as the *Ioffe field*. The trapped atom's magnetic moment will be aligned to this direction. (B) Depiction of the radial confinement field produced from the Ioffe coils which form a 2D quadrupole. The relative magnitude of the field is given by the colorscale where black is zero field, and yellow is high field, and the white arrows show the direction of the field.

The field near the minimum can be approximated to,

$$
|\mathbf{B}| \simeq B_0 + \frac{B''}{2} z^2 + \frac{1}{2}\left(\frac{B'^2}{B_0} - \frac{B''}{2}\right)\left(x^2 + y^2\right). \tag{2.6}
$$

Substituting this expression for $|\mathbf{B}|$ into Eq. (2.5), we get the potential energy,

$$
U(x, y, z) = g_F m_F \mu_{\mathrm{B}} |\mathbf{B}| = g_F m_F \mu_{\mathrm{B}} B_0 + \frac{1}{2}\left(\omega_x^2 x^2 + \omega_y y^2 + \omega_z z^2\right), \tag{2.7}
$$

where m is the mass of the atom, and ω_i are the trap frequencies. Since the configuration exhibits radial symmetry we refer to the trap frequencies as radial $\omega_\perp = \omega_x = \omega_y$ and axial $\omega_\parallel = \omega_z$ which are given by

$$\omega_\perp = \sqrt{\frac{g_F m_F \mu_B}{m}\left(\frac{B'^2}{B_0} - \frac{B''}{2}\right)} \tag{2.8}$$

$$\omega_\parallel = \sqrt{\frac{g_F m_F \mu_B}{m}B''}. \tag{2.9}$$

The radial trap frequency can be tuned by changing the offset field B_0, this can be done by applying a bias field in an opposing direction to the Ioffe field, this field is known as the *anti-Ioffe field*.

Planar wire traps

Initial realisations of the IP trap were achieved using large external 3D coils, and sometimes required hundreds of amps to create the desired fields, usually because of the large distance from the trapping region to the field source. These types of set-ups consumed lots of power, and often required water cooling, making the set-up even bulkier. It was pointed out that significant gains could be made using micro-traps as the magnetic field, gradient, and curvature scale as I/S, I/S^2, and I/S^3 respectively, where I is the current in the wires and S is their characteristic size [51]. Initially free standing single wires or *atom wires* inside the vacuum chamber were used [46, 52, 53], this allowed atoms to be trapped very close to the surface of the field source. However, these wires were often very delicate and could easily be deformed by external forces, and their fragility only gets worse the smaller the wire is, ultimately limiting S. The wire being free standing in the vacuum means that heat created from joule heating can only be channelled away via conduction through the wire itself, limiting its current capacity and hence the field strength produced. A major step in progress was the advent of the *atom chip* [20, 54], in which micron scale wires were deposited onto a substrate as opposed to standing freely. Placing the wires onto a substrate not only made them more robust (allowing them to be made much smaller) but also supplied an extra conduction path for heat to flow, which greatly improved heat dissipation and thus increased the current capacity and in turn the field strength. Initial fabrication techniques used electroplating, however this gave relatively large surface roughness and led to severe fragmentation of the cloud [55] (see Section 3.2.3) limiting the trapping distances to on the order of $100\,\mu$m. Later, fabrication methods moved to gold evaporation which gave a much improved surface roughness and allowed for trapping distances of a few micrometres [56, 57].

To understand how the 3D IP trap can be recreated on a 2D surface let us consider first the magnetic field **B** produced at point **r** by a single current carrying wire, which

can be calculated using the Biot-Savart law,

$$\mathbf{B}(\mathbf{r}) = \frac{\mu_0}{4\pi} \int_V \mathbf{j}(\mathbf{r}') \times \frac{\mathbf{r} - \mathbf{r}'}{|\mathbf{r} - \mathbf{r}'|^3} \mathrm{d}V', \tag{2.10}$$

where $\mathbf{j}$ is the current density, V is the volume of the wire, V' is the volume element, and $\mathbf{r}'$ is a point within that volume. The volume integral is simplified to a line integral by approximating the wire as infinitely thin, which gives,

$$\mathbf{B}(\mathbf{r}) = \frac{\mu_0}{4\pi} \int_C I \mathrm{d}l \times \frac{\mathbf{r} - \mathbf{r}'}{|\mathbf{r} - \mathbf{r}'|^3}, \tag{2.11}$$

where C is wire path, and $\mathrm{d}l$ is the length element of the wire. For an infinitely long wire the solution is

$$\mathbf{B}(\mathbf{r}) = \frac{\mu_0 I}{2\pi d}, \tag{2.12}$$

where d is the distance from point r to the wire. The magnetic field gradient, and curvature are then given by,

$$\mathbf{B}(\mathbf{r})' = -\frac{\mu_0 I}{2\pi d^2}, \quad \text{and} \quad \mathbf{B}(\mathbf{r})'' = \frac{\mu_0 I}{\pi d^3}. \tag{2.13}$$

Radial [1] confinement can be achieved by applying an opposing bias field, B_{bias}, this is shown in Fig. 2.4. The bias field will cancel the field produced by the wire at a position

$$r_0 = \frac{\mu_0 I}{2\pi B_{\text{bias}}}. \tag{2.14}$$
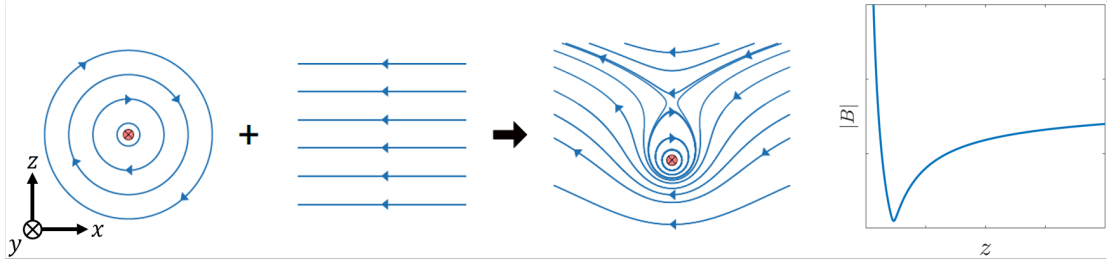
FIGURE 2.4: Single wire guide potential, this provides a 2D quadrupole along the axis of the wire and is radially symmetric. The position of the minimum is determined by Eq. (2.14). The plot shows the magnitude of the field $|\mathbf{B}|$ as function of z which represents the vertical distance from the surface of the wire. Note the minimum does not go to zero as an offset field is provided by the axial potential in Fig. 2.5.

To create axial confinement two parallel *leg* wires carry current in parallel or anti-parallel. The parallel case is depicted in Fig. 2.5, this not only creates a confining potential along y but also provides the Ioffe field (preventing Majorana transitions

---

[1]For consistency with Fig. 2.6 and Fig. 3.18 I will now define the radial coordinates as x and z and the axial coordinate as y.

and defining a quantisation axis). The magnitude of the Ioffe field is determined by trap position r_0 and the leg wire current I_{leg}.
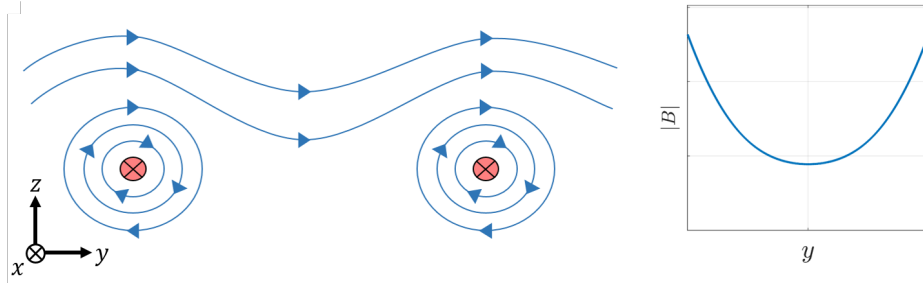
FIGURE 2.5: Diagram showing how two parallel wires (or leg wires) combine to form a confining potential along the y-axis.

Some common wire configurations are shown in Fig. 2.6. In our experiment we use a modified U-trap [58] to produce the magneto optical trap (MOT) fields, a Z-trap for magnetic trapping of thermal clouds, and a H-trap for BECs. Though the H-trap requires more wires and an extra layer than the Z-trap, its advantage is that the current in the legs is independent of the current in the central wire. This means $\omega_{\parallel}$ and $\omega_{\perp}$ are decoupled, giving greater flexibility in tuning the aspect ratio $\lambda = \omega_{\perp}/\omega_{\parallel}$ which was a key free parameter for our experiment in Chapter 4. For this reason we chose a H-trap to create the final trapping potential, however for practical reasons the initial magnetic trap we chose was the Z-trap. The initial fields require a very high current (100 A) for the reasons stated in Section 3.2.1, supplying this level of current requires expensive and bulky power supplies, thus using a Z-trap saves us space, money, and also simplifies the set-up.

FIGURE 2.6: (Left to right) Z, H, and U trap. The Z and H traps produce IP traps, the trap bottom B_0 can be tuned with the anti-Ioffe field B_{AI}. A Z-trap can be made from a single wire but the H-trap requires three wires and two planes. The counter-propagating current flow in the U-trap legs creates a quadrupole field in the y direction and is typically used for MOT fields as the field flips direction t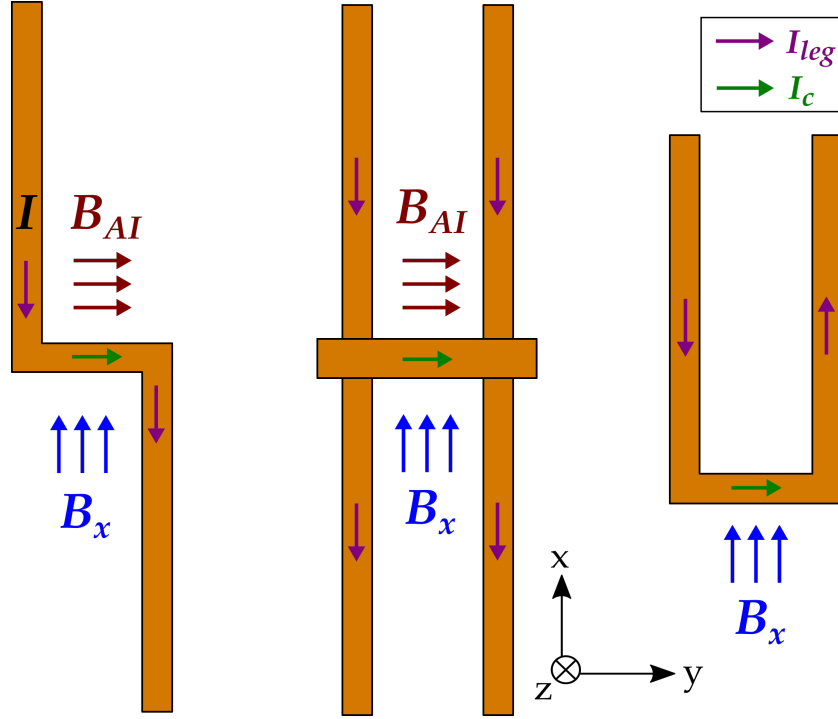hrough the minimum which is necessary for laser cooling [43], and the zero-field is not an issue as hot atoms are less sensitive to Majorana transitions.

Though not shown in Fig. 2.6 quadrupole fields can also be created by two-wire guides [46, 59]. There is great flexibility in the wire patterns that can be constructed and hence myriad complex field configurations can be produced, which are also sometimes used to transport atoms [60–62]. However, the four mentioned in this section are the most commonly used.

An undesirable effect of the Z and H-traps is a rotation of the isopotential about the z-axis. This arises from the asymmetry in vertical fields produced by the leg and central wires, an illustration of the fields can be seen in Fig. 2.7. The eigenaxes (x', y', z') of the trap can be found by diagonalising the Hessian matrix at r_0 [38]. The angle of rotation θ increases with the relative contribution of the leg wires to the potential, which can happen by increasing I_{leg} or r_0. This is important as increasing either parameter will typically decrease the aspect ratio i.e.

$$\theta \propto 1/\lambda. \tag{2.15}$$

Section 3.3.3 outlines how θ can be detrimental to our detection method. As λ is a control variable in our experiment in Chapter 4, not accounting for θ would lead to systematic errors.
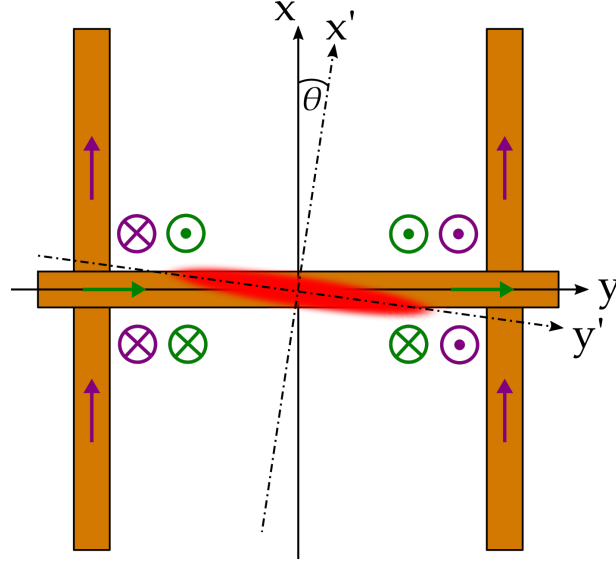
FIGURE 2.7: Rotation of the potential in an H-trap, this arises due the vertical fields produced by the leg and central wires, represented in purple and green respectively. Analysing the fields at the four inner corners it been seen that cancellation occurs along the diagonal. Here, θ is the angle of rotation about the z-axis, x and y are the principal axes of the wire structure, and x' and y' are the eigenaxes of the trapping potential.

We use a numerical simulation of our trapping structures (see Section 3.2) that calculates the Hessian matrix at the minimum, this lets us obtain a value for θ, and since the eigenvalues of the Hessian matrix correspond to the curvature of the field the trap frequencies can also be obtained through,

$$\omega_i = 2\pi \times \sqrt{\frac{g_F m_F \mu_{\mathrm{B}}}{m} \frac{\partial^2 |\mathbf{B}|}{\partial r_i'^2}}. \tag{2.16}$$

Experimentally, precise measurements of θ were not possible, however measuring ω_i is relatively simple Fig. 3.42. Measurements of ω_i gave good agreement with our simulations to within $5\,\%$, we therefore assume that the simulated value of θ can be trusted.

2.1.2 Evaporative cooling

For a dilute atomic gas to condense the phase space density, $\rho_{\mathrm{PSD}} = n(0)\lambda_{\mathrm{DB}}^3$ must be on the order of 1 [45] here $n(0)$ is the peak atomic density and $\lambda_{\mathrm{DB}} = \sqrt{2\pi\hbar^2/mk_{\mathrm{B}}T}$ is the thermal de Broglie wavelength. Phase space density is increased with reducing temperature, as mentioned previously laser cooling a powerful cooling tool that can increase ρ_{PSD} from 10^{-13} to 10^{-6} [63], however this still falls short by six orders of magnitude . Evaporative cooling is a key step to increase ρ_{PSD} by a factor of 10^6, this process was used in the first realisation of atomic BECs [2, 3] and has been used ever since. The complete model is complex, so this section will not go into too much detail

but instead introduce the important concepts and parameters, for further reading, a quantitative model can be found in [64, 65]. The basic principle is to remove particles with energy higher than the average from the trap, and after the cloud has rethermalised, the resulting ensemble will have a lower temperature. For clouds with $\rho_{\mathrm{PSD}} \ll 1$, the effects of quantum statistics can be neglected, and the particles can be assumed to obey Maxwell-Boltzmann statistics (since the condition of $\rho_{\mathrm{PSD}} \sim 1$ is only satisfied at the end of the cooling the model assumes only Maxwell-Boltzmann statistics). The process can interpreted as the removal of the high-energy tail of the distribution, the energy at which the tail is removed is related to the temperature of the gas by the truncation parameter, $\eta = \epsilon_{\mathrm{cut}}/k_{\mathrm{B}}T$. The truncated distribution has the form [64]

$$f(\epsilon) = n(0)\lambda_{\mathrm{DB}}^3 \exp\left(\frac{-\epsilon}{k_{\mathrm{B}}T}\right) \Theta(\epsilon_{\mathrm{cut}} - \epsilon). \tag{2.17}$$

Here, $\Theta(\epsilon_{\mathrm{cut}} - \epsilon)$ is the Heaviside step function, which is equal to zero for $\epsilon > \epsilon_{\mathrm{cut}}$. Visualisation of the truncation process is displayed in Fig. 2.8.
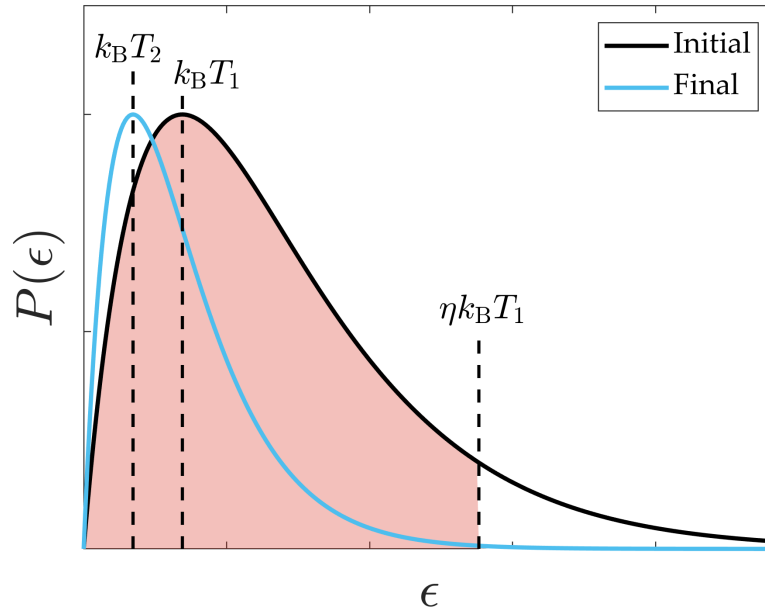
FIGURE 2.8: A gas of thermal atoms with temperature T_1 has a Maxwell-Boltzmann distribution, where the most probable energy is $k_{\mathrm{B}}T_1$. The cooling process removes particles with energy higher than $\eta k_{\mathrm{B}}T_1$, the remaining particles collide and *rethermalise* to a lower temperature and fewer atoms.

Once the truncated distribution has rethermalised ϵ_{cut} has to be reduced to prevent η from increasing, this continual reduction in trap depth is known as forced evaporation. Thus ϵ_{cut} is time dependent and has to be tuned specifically to the experimental sequence. Cooling efficiency can described by the parameter α, which is

the reduction in temperature per atoms lost [65],

$$\alpha = \frac{d(\ln T)}{d(\ln N)} = \frac{\dot{T}/T}{\dot{N}/N}, \tag{2.18}$$

the larger α the more efficient the cooling process is. A measurement of the cooling efficiency for our experiment is shown in Fig. 3.40. Efficient cooling, or runaway evaporation, can only occur if the rethermalisation time τ_{el} is shorter than the timescale of losses due to background collisions τ_{bg}. Rethermalisation occurs through elastic collisions between the atoms and are often referred to as "good" collisions (each atom on average must undergo ~ 4 scattering events for the cloud to rethermalilse [66]), whereas the collisions with background are bad collisions. The parameter R is the ratio of good to bad collisions $R = \tau_{\mathrm{bg}}/\tau_{\mathrm{el}}$. The condition for runaway evaporation can be expressed in terms of R (for a harmonic trapping potential) [65],

$$R \geq R_{\min} = \frac{\tau_{\mathrm{ev}}}{\tau_{\mathrm{el}}} \frac{1}{\alpha - 1} \tag{2.19}$$

where τ_{ev} is the time scale for evaporation given by,

$$1/\tau_{\mathrm{ev}} = -\frac{\dot{N}}{N} = n(0)\sigma_{\mathrm{el}}\bar{v}\eta\mathrm{e}^{-\eta}. \tag{2.20}$$

The time scale of elastic collisions τ_{el} is determined by the elastic collision rate γ_{el},

$$1/\tau_{\mathrm{el}} = \gamma_{\mathrm{el}} = n(0)\sigma_{\mathrm{el}}\bar{v}\sqrt{2}, \tag{2.21}$$

where σ_{el} is elastic collision cross-section, and $\bar{v}\sqrt{2}$ is the average relative velocity between two atoms [65]. The peak density $n(0)$ of a thermal cloud in a spherically symmetric harmonic potential (i.e. $\omega_x = \omega_y = \omega_z$) is given by,

$$n(0) = N\omega^3 \left(\frac{m}{2\pi k_{\mathrm{B}}T}\right)^{3/2} \tag{2.22}$$

this means that adiabatically compressing the trap is advantageous as it increases the γ_{el}. A typical cooling sequence will compress the trap whilst reducing ϵ_{cut}. For good efficiency (large α) τ_{ev} needs to be increased, however this also increases $R_{\min}$ and decreases R. There is a trade-off between the efficiency and the speed of the ramp (the rate at which ϵ_{cut} is reduced), too fast and there are insufficient collisions to rethermalise properly, too slow and too many atoms are lost to background collisions.

Radio-frequency evaporation

To selectively remove high energy atoms from the trap we use radio-frequency radiation, this method was used in the first BEC experiments [2] and is still used by almost all experiments with BECs of alkali atoms. Radio-frequency radiation is

applied that is resonant with Zeeman splitting Eq. (2.5) between the m_F states, due to the spatially varying magnetic field of the trapping potential $\hbar\omega_{\mathrm{RF}}$ is only resonant in a particular region of space. Resonant atoms will be transferred into the lower m_F states eventually transitioning to a high field seeking state and are repelled from the trap. Larger distances from the trap centre are only accessible by hotter atoms, thus by tuning $\hbar\omega_{\mathrm{RF}}$ hotter atoms can be selectively removed from the trap.
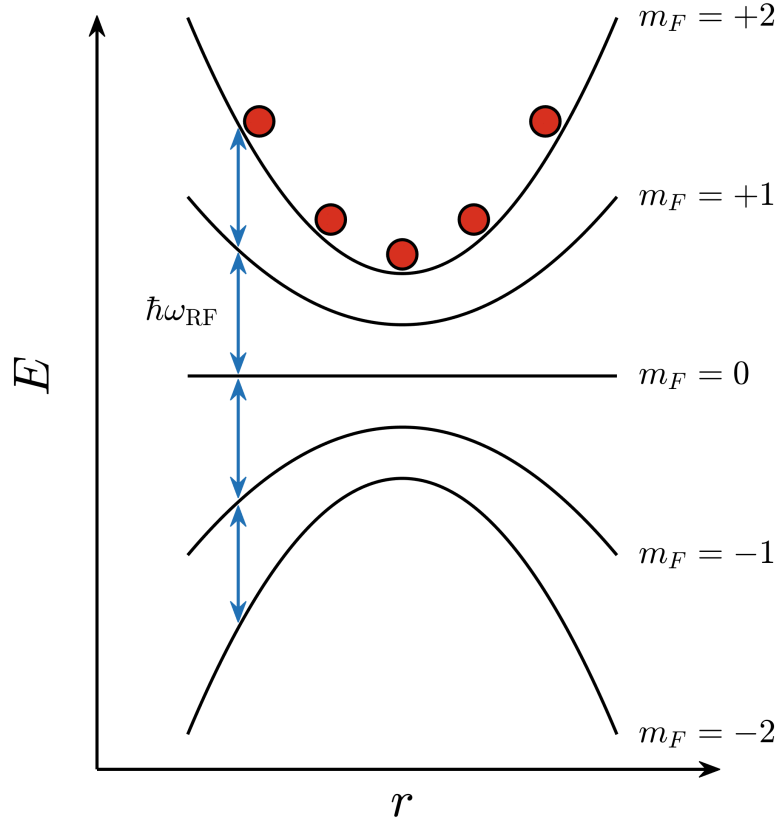
FIGURE 2.9: Principle of radio-frequency cooling, when $\hbar\omega_{\mathrm{RF}} = g_F\mu_{\mathrm{B}}|\mathbf{B}(\mathbf{r})|\Delta m_F$ atoms will undergo a cascade of transitions to an untrapped state.

The trap depth is set by RF frequency $\epsilon_{\mathrm{cut}} = 2\hbar(\omega_{RF} - \omega_0)$, where $\hbar\omega_0$ is the energy separation at trap minimum. In the $|F = 2\rangle$ ground state $\omega_0 = 2\pi\times 0.7\,\mathrm{MHz\,G^{-1}}$. An advantage of using RF frequency cooling is that the trap depth can be decreased independently of the static trapping potential, thereby maintaining large trapping frequencies throughout the process.

2.1.3 Bose-Einstein condensation

As the phase space density approaches unity the quantum statistics becomes important as the atoms start to become degenerate. For a gas of non-interacting bosons in thermodynamic equilibrium of atom number N and temperature T the mean occupation number of an energy state i is given by the Bose distribution

function [45],

$$f(\epsilon_i) = \frac{1}{e^{(\epsilon_i - \mu)/k_B T} - 1},$$
(2.23)

where μ is the chemical potential. At high temperatures μ is large and negative, and Eq. (2.23) is approximately the Boltzmann distribution,

$$f_{MB}(\epsilon_i) = e^{-(\epsilon_i - \mu)/k_B T},$$
(2.24)

and $f_{MB}(\epsilon_i) \ll 1$ thus the occupation number for any particular state is low. As the temperature is lowered the chemical potential increases and thus $f(\epsilon_0)$ increases, the chemical potential is constrained $\mu < \epsilon_0$ otherwise the occupation number would become negative and therefore unphysical [45]. In the case for a harmonic trapping potential defined as,

$$V(\mathbf{r}) = \frac{1}{2}m\left(\omega_x^2 x^2 + \omega_y^2 y^2 + \omega_z^2 z^2\right),$$
(2.25)

the energy levels ϵ_i of the Bose distribution function will then be,

$$\epsilon(n_x, n_y, n_z) = (n_x + \frac{1}{2})\hbar\omega_y + (n_y + \frac{1}{2})\hbar\omega_x + (n_z + \frac{1}{2})\hbar\omega_z.$$
(2.26)

Bose-Einstein condensation occurs when there is macroscopic occupation of the ground state ϵ_0. The critical temperature T_c is defined as the point at which macroscopic occupation occurs, signifying the onset of Bose-Einstein condensation. Here I will derive T_c following the steps in [45]. For large atom number $N_{tot} = N_0 + N_{ex}$ (number of atoms in the ground state plus the number in all of the excited states), ϵ_0 is chosen to be zero, which also constrains $\mu \leq 0$. The number of particles in the excited states is given by,

$$N_{ex} = \int_0^\infty g(\epsilon) f(\epsilon) d\epsilon$$
(2.27)

where $g(\epsilon)$ is the density of states, which for a three dimensional anisotropic harmonic oscillator is,

$$g(\epsilon) = \frac{\epsilon^2}{2\hbar^3 \omega_x \omega_y \omega_z}.$$
(2.28)

Equation 2.27 is maximised when $\mu = 0$, this means that there is an upper bound on the number of atoms that can occupy the excited states N_{ex}^{max}. If $N_{tot} > N_{ex}^{max}$ the surplus atoms must reside in the ground state, therefore at $N_{tot} = N_{ex}^{max}$, $\mu = 0$, and $T = T_c$. Applying these conditions to Eq. (2.27) we get,

$$N_{ex}^{max}(\mu = 0, T = T_c) = \int_0^\infty \frac{g(\epsilon)}{e^{\epsilon/k_B T_c} - 1} d\epsilon.$$
(2.29)

Evaluating the integral we get the expression of T_c for an ideal gas in a harmonic trap [45],

$$T_c = 0.94 \frac{\hbar}{k_B} \bar{\omega} N_{tot}^{1/3}, \tag{2.30}$$

where $\bar{\omega}$ is the geometric mean trapping frequency. Combining this result with Eq. (2.29) and $N_{tot} = N_0 + N_{ex}$, we get the condensate fraction as a function of temperature,

$$\frac{N_0}{N_{tot}} = 1 - \left(\frac{T}{T_c}\right)^3. \tag{2.31}$$

In reality Eq. (2.31) needs a number of corrections to account for finite size [67] and interactions [68] (interestingly in this paper they also show that interactions between the condensate and the thermal fraction have to be accounted for). Remaining in the ideal case, without interactions, the ground state $\phi(\mathbf{r})$ is obtained by putting all the particles in the lowest single particle state ($n_x = n_y = n_z = 0$), then the total ground state is the product of all the single particle states $\phi(\mathbf{r}) = \Pi_i \varphi_0(\mathbf{r}_i)$, where $\varphi_0(\mathbf{r})$ is determined by the Schrödinger equation [67],

$$\varphi_0(\mathbf{r}) = \left(\frac{m\bar{\omega}}{\pi\hbar}\right)^{3/4} \exp\left(-\frac{m}{2\hbar}(\omega_x x^2 + \omega_y y^2 + \omega_z z^2)\right). \tag{2.32}$$

The density distribution is $n(\mathbf{r}) = N|\varphi_0(\mathbf{r})|^2$, which increases with N, however the size of condensate does not, its size is fixed by the harmonic oscillator length $a_{ho} = \sqrt{\hbar/m\bar{\omega}}$.

Interactions

Whilst the case of an ideal Bose gas proves instructive, it is not representative of the experimental situation. Even though the gases are very dilute interactions between the atoms still exist, these can be attractive or repulsive (for ^{87}Rb interactions are repulsive). As the gas is cold and dilute the inter-atomic interaction, $U(\mathbf{r}' - \mathbf{r})$, is simplified as only low energy two-body collisions are likely, they are characterised by the s-wave scattering length [67]. In this regime the interactions can be described with an effective contact potential,

$$U(\mathbf{r}' - \mathbf{r}) = g_{3D}\delta(\mathbf{r}' - \mathbf{r}), \tag{2.33}$$

where g_{3D} is the coupling constant and is related to the s-wave scattering length a by,

$$g_{3D} = \frac{4\pi\hbar^2 a}{m}. \tag{2.34}$$

Accounting for this interaction with mean-field approach leads to a modification of the Schrödinger equation, giving the time-dependent Gross-Pitaevskii equation (GPE) (for derivation of the GPE see [67]),

$$i\hbar\frac{\partial}{\partial t}\Phi(\mathbf{r}, t) = \left(-\frac{\hbar^2\nabla^2}{2m} + V(\mathbf{r}) + g_{3D}|\Phi(\mathbf{r}, t)|^2\right)\Phi(\mathbf{r}, t). \tag{2.35}$$

Here, $\Phi(\mathbf{r}, t)$ is the order parameter or wave function of the condensate which comes from the Bogoliubov approximation. The ground state is obtained by writing the wave function into time and spatial-dependent terms $\Phi(\mathbf{r}, t) = \phi(\mathbf{r}) \exp(-i\mu t/\hbar)$, Eq. (2.35) becomes the time-independent GPE,

$$\left(\underbrace{-\frac{\hbar^2 \nabla^2}{2m}}_{Kinetic} + V(\mathbf{r}) + \underbrace{g_{3\mathrm{D}}|\phi(\mathbf{r})|^2}_{Interaction} \right) \phi(\mathbf{r}) = \mu \phi(\mathbf{r}). \tag{2.36}$$

This equation is said to be a nonlinear Schrödinger equation, as the interaction term $g|\phi(\mathbf{r})|^2$ is a source of nonlinearity, which is proportional to density as $n(\mathbf{r}) = |\phi(\mathbf{r})|^2$.

Thomas-Fermi approximation

Interactions can have a dramatic effect on the condensate density, depending on the sign of g the density will either be attracted to or repelled from centre, deforming the Gaussian Eq. (2.32). For sufficiently large N the interaction energy becomes much larger than the kinetic energy and the corresponding KE term can be dropped. Neglecting the kinetic energy from Eq. (2.36) leaves,

$$\left[V(\mathbf{r}) + g_{3\mathrm{D}}|\phi(\mathbf{r})|^2 \right] \phi(\mathbf{r}) = \mu \phi(\mathbf{r}). \tag{2.37}$$

this is known as the Thomas-Fermi approximation. It has the solution [45],

$$n(\mathbf{r}) = |\phi(\mathbf{r})|^2 = (\mu - V(\mathbf{r}))/g_{3\mathrm{D}}, \tag{2.38}$$

in the region that $V(\mathbf{r}) \leq \mu$, and $n(\mathbf{r}) = 0$ for $V(\mathbf{r}) > \mu$. Thus the size of the cloud is determined by the chemical potential and the trapping potential. For an anisotropic harmonic potential, the radii in each direction are

$$R_i = \sqrt{\frac{2\mu}{m\omega_i^2}}, \tag{2.39}$$

the radius R, is hence referred to as the Thomas-Fermi radius. The density profile has the form of an inverted parabola

$$n(\mathbf{r}) = \frac{18}{8\pi} \frac{N_0}{R_x R_y R_z} \left(1 - \frac{x^2}{R_x^2} - \frac{y^2}{R_y^2} - \frac{z^2}{R_z^2} \right), \tag{2.40}$$

and the chemical potential μ, which serves to normalise the distribution to the total number of particles N_0, is given by

$$\mu = \frac{1}{2}\hbar\bar{\omega} \left(\frac{15a}{a_{\mathrm{ho}}} N_0 \right)^{2/5}. \tag{2.41}$$

2.2 Coherence properties of Bose gases

The flexibility to manipulate the trapping potentials in the experimental systems has allowed experiments to force constraints onto condensed systems that induce two- or one-dimensional behaviour. The trapping potential for 2D system results in a pancake-like density, whereas for a 1D system the density is an elongated cigar shape. Strictly speaking, to be 1D/2D the following criteria need to be satisfied

$$\mu \ll \hbar\omega_\perp \tag{2.42a}$$

$$k_{\mathrm{B}}T \ll \hbar\omega_\perp \tag{2.42b}$$

where $\omega_\perp$ is the trapping frequency in the transverse direction or the system's short axis. Excitations to higher energy transverse modes are not possible, and the transverse dynamics are "frozen out". Clouds satisfying Eq. (2.42a) or Eq. (2.42b) are said to be chemically or thermally 2D/1D. The coherence properties of 2D/1D systems differ significantly from the 3D situation, and the defining features of the BEC are not upheld, as such true Bose-Einstein condensation is not possible at finite T in 2D or 1D systems (for $T = 0$ condensation is possible in 2D, but not in 1D [16]). The definition of a BEC is often stated as the presence of off-diagonal long-range order in the density matrix $\rho^{(1)}$, i.e. the $\langle \mathbf{r}'|\rho^{(1)}|\mathbf{r}\rangle \neq 0$ even as $|\mathbf{r}' - \mathbf{r}| \to \infty$ [69], it is this condition that is not satisfied at finite temperature T in one or two dimensions [70]. That being said, the coherence properties observed still have condensate-like behaviour, and are commonly referred to as quasi-condensates. In this section I will discuss the coherence properties in more detail, but I will focus only on 3D and 1D systems as the 2D case is not relevant to our experiment.

2.2.1 Correlation functions

In order to analyse the coherence properties it is useful to introduce the first and second order correlation functions $G^{(1)}$ and $G^{(2)}$, as they are inherently related to the coherence. First presented by R. Glauber in 1963 to define coherence of light fields [71–73], the correlation functions were later used to study coherence of Bose gases [74, 75]. The first-order, or one-body, correlation function describes the spatial coherence and is defined as,

$$G^{(1)}(\mathbf{r}, \mathbf{r}') = \langle \hat{\Psi}^\dagger(\mathbf{r})\hat{\Psi}(\mathbf{r}')\rangle, \tag{2.43}$$

where $\hat{\Psi}^\dagger(\mathbf{r})$ and $\hat{\Psi}(\mathbf{r}')$ are the creation and annihilation field operators of the second quantisation representation. $G^{(1)}$ is normalised by the density $n(\mathbf{r})$ to give

$$g^{(1)}(\mathbf{r}, \mathbf{r}') = \frac{\langle \hat{\Psi}^\dagger(\mathbf{r})\hat{\Psi}(\mathbf{r}')\rangle}{\sqrt{n(\mathbf{r})n(\mathbf{r}')}}, \tag{2.44}$$

this function describes the phase coherence of the system, and it often has a characteristic length scale over which it decays, which is referred to as the phase coherence length.

The second-order, or two-body, correlation function $G^{(2)}$ gives the probability of finding a particle at position $\mathbf{r'}$ given that there is a particle at $\mathbf{r}$. It describes the density correlations and is defined as,

$$G^{(2)}(\mathbf{r}, \mathbf{r'}) = \left\langle \hat{\Psi}^\dagger(\mathbf{r})\hat{\Psi}(\mathbf{r})\hat{\Psi}^\dagger(\mathbf{r'})\hat{\Psi}(\mathbf{r'}) \right\rangle, \tag{2.45}$$

and is normalised by the density squared,

$$g^{(2)}(\mathbf{r}, \mathbf{r'}) = \frac{\left\langle \hat{\Psi}^\dagger(\mathbf{r})\hat{\Psi}(\mathbf{r})\hat{\Psi}^\dagger(\mathbf{r'})\hat{\Psi}(\mathbf{r'}) \right\rangle}{n(\mathbf{r})n(\mathbf{r'})}. \tag{2.46}$$

A famous measurement of second-order correlations was the Hanbury Brown and Twiss experiment [76–78]. In this experiment they were able to determine the size of the star Sirius by measuring the decay of second-order (intensity-intensity) correlations using two detectors with variable separation. A known property of light is photon-bunching ($g^{(2)}(0) > 1$), which is observed when the light source is incoherent. Bunching is absent when the light source is coherent, i.e. from a laser. Interestingly, Bose gases display behaviour analogous to photons. Bosonic bunching occurs in thermal gases (incoherent source), whereas for a BEC (coherent source) the bunching is absent. This behaviour was measured experimentally in [79].

2.3 Regimes of interacting Bose gases

In this section I will relate the correlations and fluctuations in different regimes of the 3D and 1D systems. The 3D model has already been introduced so I will go directly into the discussion of correlations. For the 1D case I will first introduce the Lieb-Liniger model to and define the different sub-regimes of 1D systems along with their coherence properties.

2.3.1 Correlations in 3D systems

In 3D a thermal gas ($T > T_c$) the normalised first and second order correlation functions are related by [75],

$$g^{(2)}(\mathbf{r}, \mathbf{r'}) = 1 + g^{(1)}(\mathbf{r}, \mathbf{r'})^2. \tag{2.47}$$

The phase coherence length is the thermal de Broglie wavelength λ_{dB}, over this distance $g^{(1)}(\mathbf{r}, \mathbf{r'})$ will decay to zero,

$$g^{(1)}(\mathbf{r}) \simeq \exp\left(-\pi \frac{r^2}{\lambda_{\mathrm{dB}}^2}\right). \tag{2.48}$$

Thus $g^{(1)}(0) = 1$ and from Eq. (2.47) $g^{(2)}(0) = 2$, which means it is twice as likely to find a particle at the same position than at a distance greater than $\lambda_{\rm dB}$, this property is known as *bosonic bunching* which was previously mentioned in analogy to incoherent light sources Section 2.2.1. For a pure BEC the phase coherence length goes to infinity and $g^{(1)}(\mathbf{r}, \mathbf{r}') = 1$ everywhere. For a partially condensed gas $N_0 < N_{\rm to}$ $g^{(1)}(\mathbf{r}, \mathbf{r}')$ decays from 1 to a finite value determined by the local condensate fraction $N_0/N_{\rm tot}$ [75]. In this case the second order correlation function is given by [80],

$$g^{(2)}(\mathbf{r}, \mathbf{r}) = 2 - \left(\frac{|\psi(\mathbf{r}, \mathbf{r}')|^2}{n(|\mathbf{r} - \mathbf{r}'|)} \right)^2, \tag{2.49}$$

where the second term is ratio of the local condensate density to the total density. For a pure BEC $g^{(2)}(\mathbf{r}, \mathbf{r}) = 1$ over the whole sample.

2.3.2 One-dimensional systems

Lieb-Liniger model

In 1963 Lieb and Liniger introduced the Hamiltonian for a one-dimensional gas of bosons [21, 22]

$$\hat{H} = -\frac{\hbar^2}{2m} \sum_{i=1}^{N} \frac{\partial^2}{\partial y^2} + g_{\rm 1D} \sum_{i<j=1}^{N} \delta(y_i - y_j). \tag{2.50}$$

where $g_{\rm 1D}$ is a general one-dimensional interaction parameter (this assumes repulsive contact interactions), for consistency with the coordinate system used in the experimental section I will define the axial direction along y, and the radial direction in the $x - z$ plane. The Lieb-Liniger model solves this Halmiltonian at $T = 0$ with a Bethe-Ansatz [1], providing a method to calculate the equilibrium ground state and excitation spectrum. Later the Yang and Yang used a thermodynamic Bethe-Ansatz to derive thermodynamic functions for a system at finite T [24].

The transverse ground state for a one-dimensional gas in a harmonic trap has a Gaussian form [81, 82]

$$\phi_\perp(\mathbf{r}) = \left(\frac{m\omega_\perp}{\pi\hbar} \right)^{1/4} \exp\left(\frac{m\omega_\perp \mathbf{r}^2}{2\hbar} \right), \tag{2.51}$$

where $\mathbf{r} = (x, z)$ represents the transverse directions, and $a_\perp = \sqrt{\hbar/m\omega_\perp}$ is the harmonic oscillator length in the transverse direction. If the condition $\mu/\hbar\omega_\perp \ll 1$ is not quite satisfied then the transverse ground state swells due to the interactions [83]. If the s-wave scattering length $a < a_\perp$ then the three-dimensional behaviour of collisions remains. The 1D scattering parameter is then calculated by integrating out

the transverse degrees of freedom [81],

$$g_{1D} = \frac{2\pi\hbar^2 a}{ma_\perp^2}.$$
(2.52)

The interaction coupling constant g_{1D} can be used to define an intrinsic length, $l_g = \hbar^2/mg_{1D}$, of the interactions [84]. The length scale is related to the Lieb-Liniger parameter γ, (a dimensionless quantity characterising the interaction strength) by,

$$\gamma = \frac{1}{n_{1D}l_g} = \frac{mg_{1D}}{\hbar^2 n_{1D}},$$
(2.53)

where $n_{1D} = N/L$, with L being the length of the gas. Interestingly, as opposed to the case in three-dimensions, Eq. (2.53) shows that in one-dimension interactions actually increase with decreasing density. The degeneracy temperature in one-dimension is [14, 84],

$$T_{1D} = \frac{\hbar^2 n_{1D}^2}{2mk_B},$$
(2.54)

whereas the equivalent temperature in 3D is given by Eq. (2.30). It is also useful to introduce a dimensionless temperature t, where,

$$t = \frac{T}{T_{1D}\gamma^2} = \frac{2\hbar^2 k_B T}{mg_{1D}^2}.$$
(2.55)

The parameters t and γ are used to build a phase diagram where different regimes can be distinguished, shown in Fig. 2.10. Note that whilst the term phase diagram is used, the regimes should not be interpreted as phase transitions. In fact phase transitions in 1D at finite T are forbidden by the Mermin-Wagner theorem [85], and the boundaries between regimes should instead be understood as smooth cross-overs.
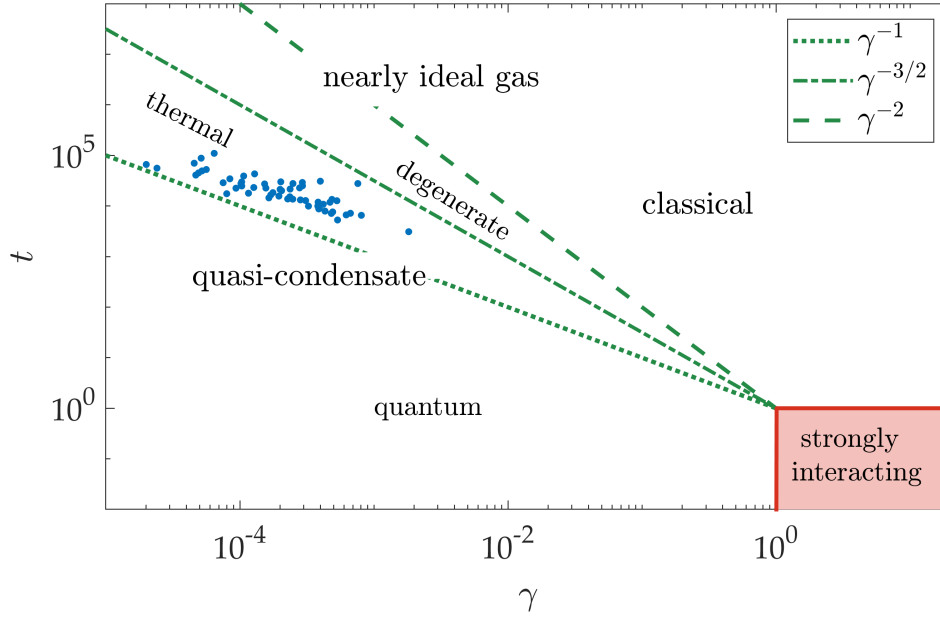
FIGURE 2.10: Phase diagram capturing the different coherence regimes of one-dimensional gases, the different regimes were calculated using the Yang-Yang model [86]. The green lines indicate the cross-over regions between different regimes, which are described in the text below. The blue dots indicate the values of all the clouds analysed in our experiment, however this will not be entirely accurate as not all the clouds can considered as one-dimensional.

Strongly interacting - ($\gamma > 1$, $t < 1$) - In this regime the interactions are very strong and completely dominate, experimentally this would be achieved with very low N and high $\omega_\perp$ (for example the experiment in [9] had an atom number of $N \sim 50$ and transverse confinement of $\omega_\perp = 70.7\,\mathrm{kHz}$). The regime is more famously known as the *Tonks–Girardeau gas* [23] here the interactions are so strong that the atoms cannot occupy the same position, and therefore are said display fermionic properties $g^{(2)}(0) = 0$. In 2004 the Tonks gas was realised twice using optical lattices [9, 10], as of yet observation of a Tonks gas on an atom chip has not been confirmed however features of the strongly interacting regime were observed in [26].

Weakly interacting - ($\gamma < 1$) - Within this regime several sub-regimes are distinguished, first is the *nearly ideal Bose gas regime* [2] which is split into a non-degenerate (classical) where $t \gg \gamma^{-2}$ & $T > T_{1D}$, and a degenerate sub-regime, where $\gamma^{-3/2} \ll t \gg \gamma^{-2}$ & $T < T_{1D}$. In the classical sub-regime temperatures are high and interactions do not play a role, as the gas is very dilute. State occupation is well described by the Boltzmann distribution Eq. (2.24), the correlation length is on the order of λ_{dB} similar to the case in 3D Eq. (2.48). Once the temperature is lowered

---

[2]following the nomenclature of [84], this is referred to as the *decoherent regime* in [86].

below T_{1D} the gas becomes degenerate and the phase coherence increases,

$$g^{(1)}(y) \simeq \exp\left(-\frac{2\pi y}{n\lambda_{\mathrm{dB}}}\right) = \exp\left(-\frac{y}{l_\phi}\right) \tag{2.56}$$

the length scale of decay, $l_\phi = \lambda_{\mathrm{dB}}^2 n/2\pi = \hbar^2 n/mk_{\mathrm{B}}T$ is much bigger than λ_{dB}. As I will explain in Section 2.3.3 density and phase fluctuations are present in this sub-regime.

Second is the *quasi-condensate regime*, which again has two sub-regimes, thermal ($\gamma^{-1} \ll t \ll \gamma^{-3/2}$) and quantum $t \ll \gamma^{-1}$. The two sub-regimes are named after dominating contributor to the fluctuations, the source of which can be either thermal or quantum. Our experiment probes the thermal quasi-condensate sub-regime, for quantum fluctuations to dominate extremely low temperatures are required [27], and are not of concern in this experiment. Density fluctuations in the quasi-condensate regime are suppressed by interactions $\langle \delta n \rangle \propto 1/g_{1D}$ Eq. (2.58), and the length scale is given by the healing length $\xi = \hbar/\sqrt{mg_{1D}n_{1D}}$. Thus the only relevant source of fluctuations in this experiment are phase fluctuations which are thermally driven, and the first order correlation function for this regime is calculated in Section 2.3.3.

2.3.3 Thermal fluctuations

Fluctuations refer to the random manifestation of excitations in the system, and they are responsible for the loss of long range order. They come in two categories, thermal or quantum fluctuations. Quantum fluctuations are a result of the Heisenberg uncertainty principle, however since they do not give significant contribution to the total fluctuations in our experimental parameter space (see Fig. 2.10) they will not be discussed in this thesis. A derivation of expressions for the fluctuations in quasi-condensates can be found in [87, 88], they apply a Bogoliubov treatment in the phase-density representation, where the field operator is expressed as

$$\hat{\psi}(r) = \sqrt{\hat{n}(r)}\exp^{i\hat{\theta}(r)}. \tag{2.57}$$

Here, $\hat{n}(r) = n_0(r) + \delta\hat{n}(r)$ ($\delta\hat{n}(r)$ accounts for the density fluctuations) and $\hat{\theta}(r)$ are spatially dependent density and phase operators. This section will avoid going into the finer details of the derivations but rather attempt to highlight the important results to give a qualitative description.

Density fluctuations

Excitations are divided into two groups, long wavelength ($k \ll 1/\xi$) phononic excitations, and short wavelength ($k \gg 1/\xi$) particle-like excitations, where $\xi = \hbar/\sqrt{mgn}$ is the healing length. The relative density fluctuations coming from

phonons with wave vectors $1/L \geq k < 1/\xi$ are given by,

$$\frac{\langle \delta n^2 \rangle_{\text{phonons}}}{n^2} \propto \frac{k_{\text{B}}T}{g\xi n^2} \propto t\gamma^{3/2}. \tag{2.58}$$

For particle like excitations the contribution from each mode is,

$$\delta n_k^2 = \frac{4mk_{\text{B}}T}{L\hbar^2 k^2} \tag{2.59}$$

which scales as $1/k^2$, to estimate the total contributions we must sum over all modes (i.e. $1/\xi \to \infty$) the contribution converges to [89],

$$\frac{\langle \delta n^2 \rangle_{\text{particles}}}{n^2} \simeq \frac{t\gamma^{3/2}}{\pi}. \tag{2.60}$$

Thus, from Eq. (2.58) and Eq. (2.60) if $t \ll \gamma^{-3/2}$ density fluctuations will be small and can be neglected, this can be seen to be true for our data in Fig. 2.10.

Phase fluctuations

From similar analysis as above we find that phonon contributions scale as [84, 89],

$$\langle \theta^2 \rangle_{\text{phonons}} \propto \frac{Lmk_{\text{B}}T}{\hbar^2 n} = \frac{L}{l_\phi} \tag{2.61}$$

where $l_\phi = \hbar^2 n / mk_{\text{B}}T$ is the phase coherence length, we see that this scales with the length of the system which sets the upper bound of the phonon wavelength.

The phase fluctuations from particle like excitations again scale with $1/k^2$, and a similar relation to Eq. (2.60) is found,

$$\langle \theta^2 \rangle_{\text{particles}} \propto t\gamma^{3/2}. \tag{2.62}$$

As is the case with the density fluctuations, if $t \ll \gamma^{-3/2}$ then contributions from particle like excitations to the phase fluctuations can be neglected. Thus in the thermal quasi-condensate regime (see Fig. 2.10) the source of the phase fluctuations comes from only thermal long wavelength excitations. We can now compute the first-order correlation function Eq. (2.44) with Eq. (2.57) (neglecting density fluctuations),

$$g^{(1)}(y) = \langle e^{i(\theta(y) - \theta(0))} \rangle. \tag{2.63}$$

Using Wick theorem $\langle e^{i(\theta(r) - \theta(0))} \rangle = e^{-\langle (\theta(r) - \theta(0))^2 \rangle / 2}$ [84]. From Eq. (2.61) we find that $\langle (\theta(r) - \theta(0))^2 \rangle = y/l_\phi$, therefore the first order correlation function is,

$$g^{(1)}(y) = e^{-|\Delta y|/\lambda_T}, \tag{2.64}$$

where $\lambda_T = 2l_\phi = 2\hbar^2 n/mk_B T$ is the thermal phase coherence length. The decay length of $g^{(1)}$ is twice as long that in the degenerate ideal Bose gas, the reason for this can be understood by the fact that in this regime both phase and density fluctuations are present, whereas in the thermal quasi-condensate regime only phase fluctuations are present [84].

In experiments a common detection method is to perform absorption imaging (see Section 3.3.1) after switching off the trapping potential (effectively instantaneously) and letting the cloud expand for a time t_{tof}. This free expansion time is called time-of-flight. It turns out that time-of-flight is particularly useful as it allows us to indirectly measure $g^{(1)}$. In-situ the quasi-condensate has a random phase pattern $\theta(y)$ that follows the the first-order correlation function in Eq. (2.64). The gradient of the phase $\nabla\theta(y)$ gives rise to a velocity field via the relation [45],

$$v(y) = \frac{\hbar}{m}\nabla\theta(y). \tag{2.65}$$

During expansion the velocity field converts into position space, and gives rise to the striking interference fringes in the density, commonly referred to as *density ripples*. This can also be seen as a self-interference effect, due to the differences in phase. In effect, free expansion transforms the phase pattern into density correlations, which experimentally is an easily measurable quantity. An analogy can also be made to speckle patterns in optics, where the quasi-condensate (laser) is a coherent source with a perturbed spatially fluctuating phase which transforms after temporal (spatial) propagation into density (intensity) fluctuations [90]. Similarities between atomic and optical speckle have been measured experimentally in references [91] and [92].

As long as the in-situ density fluctuations are small, the assumption that first-order correlations transform into second-order correlations is valid. This condition is true for the parameter space we explore (as we've shown in Section 2.3), density fluctuations only become important for temperatures close to T_c. In 2009 an analytical solution for the evolution of the power spectrum of the density ripples $\langle|\rho(q)|^2\rangle$ (which can be obtained experimentally by taking the Fourier transform of the absorption images) for one and two-dimensional systems was provided by [93] (the result will be discussed in more detail in Section 4.1.1). In the 1D case the gas is assumed to be weakly interacting, of uniform density, and infinitely long axially. The second order correlation function $g^{(2)}(y)$ and $\langle|\rho(q)|^2\rangle$ are Fourier pairs and follow the relation [93],

$$\langle|\rho(q)|^2\rangle = n_{\text{1D}}^2 \int_{-\infty}^{\infty} dy \exp(iqy) \left[g^{(2)}(y, t_{\text{tof}}) - 1\right], \tag{2.66}$$

where $\langle|\rho(q)|^2\rangle$ is given by,

$$\frac{\langle|\rho(q)|^2\rangle}{n_{\text{1D}}^2\xi} = \frac{\lambda_T q - \left[\lambda_T q \cos(2\hbar q^2 t_{\text{tof}}/m) + 2\sin(2\hbar q^2 t_{\text{tof}}/m)\right]\exp(-2\hbar q t_{\text{tof}}/m\lambda_T)}{q\xi(1 + \lambda_T^2 q^2)}.$$
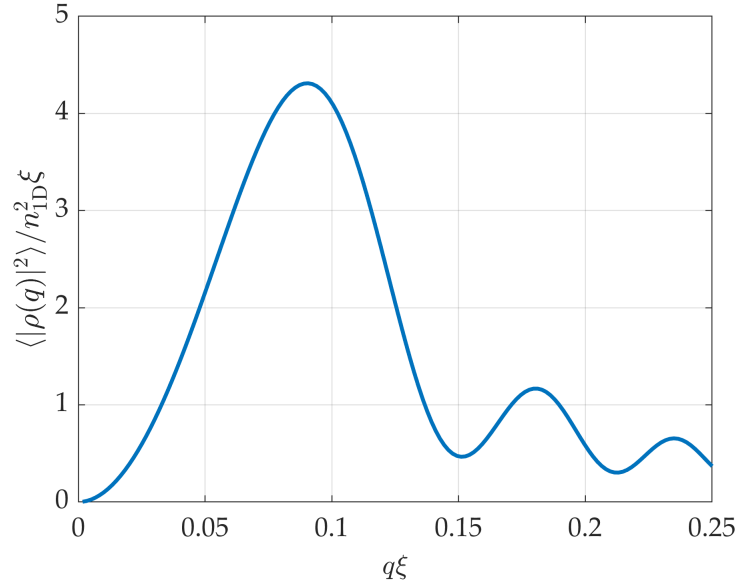$$\tag{2.67}$$

FIGURE 2.11: Power spectrum of the density ripples $\langle|\rho(q)|^2\rangle$ generated with Eq. (2.67), for a homogeneous gas of density $n_{1D} = 55\,\mu m^{-1}$ and temperature $T = 53\,nK$ after a time-of-flight of $34\,ms$.

An example of the power spectrum $\langle|\rho(q)|^2\rangle$ is plotted in Fig. 2.11, which shows clear non-monotonic behaviour. Since the phase coherence length is a free parameter in Eq. (2.67), it was suggested by [93] that this result could be used to perform thermometry where standard "fit to the wings" method fails (this method is described in Section 3.3.1). At very low temperatures there can little to no observable thermal cloud, and even with a small observable thermal fraction the signal-to-noise can be too small for reliable fitting. Good agreement with experimental measurements was observed in [94], in [95–97] they adapt Eq. (2.67) with a local density approximation (see Section 4.1.2) and also extract temperature. Agreement for the 2D scenario was found in [98].

In our experiment we measure $\langle|\rho(q)|^2\rangle$, as it is the Fourier transform of $g^{(2)}(y)$ it is related to the in-trap first order correlation function $g^{(1)}(y)$ and hence can be used to extract information of the phase coherence. Thus, by measuring $\langle|\rho(q)|^2\rangle$ whilst changing the cloud parameters we can investigate the phase coherence properties throughout the 1D-3D crossover.

Chapter 3

Experimental realisation

This chapter gives an overview of the important components in our experiment set-up, the procedure for Bose-Einstein condensate production, and a summary of the overall performance. There are numerous laboratories globally that produce Bose-Einstein condensates, incorporating many different techniques. Optimising the production process in terms of atom number, cycle time, power consumption, and system size is desirable not only for research quality but also to progress the robustness, repeatability, and commercialisation of quantum technologies. Comparing techniques is therefore valuable to academics and those in industry. In our set-up notable technologies include the 2D MOT, PCB (printed circuit board), and 3D printed structures. This chapter provides a detailed description of these components and an overview of the methods in BEC production and detection.

3.1 Experimental set-up

This sections documents the main components in the experiment. Emphasis on detail is given for components - such as imaging - that have greater significance to the experimental results in Chapter 4. When I started my PhD at the University of Sussex, our laboratories were yet to be built, and so I helped build the whole experiment from scratch. The building contains five separate laboratories all but one used for cold atom experiments. The experiment reported in this thesis is located in a laboratory named the "Green lab", the nomenclature will be used to distinguish from the other laboratories which will occasionally be referenced. Some of the components described in this section are common to the other laboratories, further information can be found in former students' theses, [39, 99].

3.1.1 Laser systems

As our building has three laboratories working with ^{87}Rb it was clear that it would be beneficial to have a centralised laser system. Sharing a laser system saves on cost, optical table space, and improves output stability (as the laboratory is isolated and less prone to disturbance). The main drawback is that failure of the laser system delays all three laboratories, however that does also mean that there are three parties interested in

getting it fixed as quickly as possible. This section describes the laser system built in the centralised laser laboratory room, the optical set-up within the Green lab, methods of stabilisation of laser frequency, power and polarisation, and the laser cooling schemes.
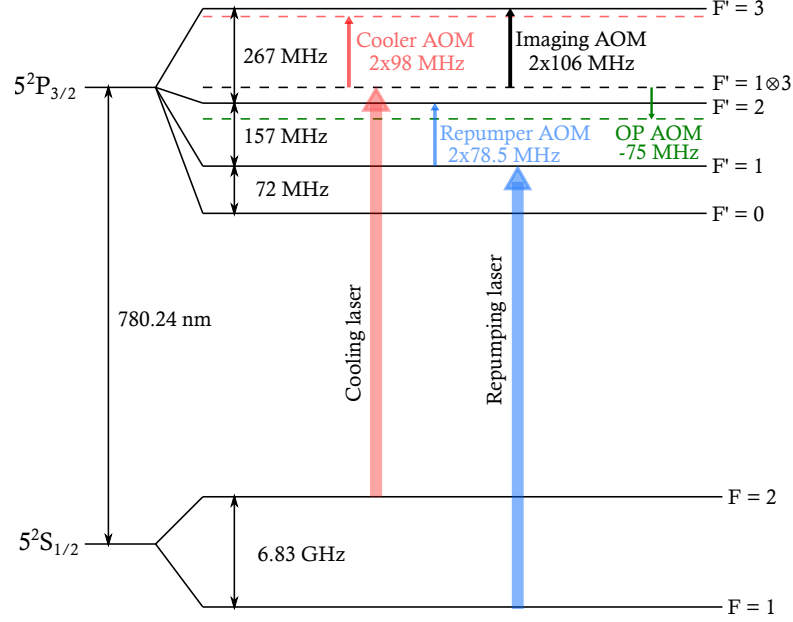

FIGURE 3.1: Energy level diagram of the ^{87}Rb D$_2$ line [44]. The laser laboratory (Fig. 3.2) provides cooling and repumping light locked to the frequencies shown in this diagram. Within each laboratory the source light from the laser laboratory is frequency shifted via acousto optic modulator's (AOMs) to the final frequencies required for the cooling, repumping, optical pumping, and imaging light. The frequency shifts required for each process are indicated on the diagram.

The laser laboratory provides each experimental lab with two laser beams that we will call *cooling beam* and *repumping beam* which are both frequency and power stabilised. Each laboratory works with ^{87}Rb, the energy level structure is shown in Fig. 3.1. The cooling light is also the source light for optical pumping and imaging. Figure 3.2 shows a diagram of the optics set-up. To supply the light we use two Toptica TA-Pro lasers, each contains an extended cavity laser diode that provides seed light for a tapered amplifier (TA) chip, which amplifies the power from $50\,\text{mW}$ to $3\,\text{W}$. In order to reduce the effect of environmental noise, each laser is housed in an optical enclosure on top of a optical table equipped with automatic re-levelling pneumatic isolators. This suppresses the effect of vibrations and temperature fluctuations. Having a separate isolated lab dramatically decreases the amount of exposure to noise that can occur from someone simply entering the room. It is also protected from electrical interference that can occur from the plethora of electrical components used in the main lab (such as ground loops, and electrical spikes from switching currents on/off). This is particularly helpful for frequency stabilisation; both power and frequency stabilisation methods will be outlined later in this section. The main output from each TA-Pro is then split into three arms using a series of mirrors and polarising

beam splitter (PBS) cubes, these are then coupled into $15\,\mathrm{m}$ long polarisation-maintaining optical fibres that are routed to each lab, see Fig. 3.2. These fibres are not capable of receiving high power input, limiting the power output to $\sim100\,\mathrm{mW}$, while this is sufficient for the repumping transition it is short of the required $2\,\mathrm{W}$ for the cooling transition. To overcome the lack of power an additional 3 W TA chip (Toptica BoostTA) is used in each lab. This amplifies the seed light from the laser lab from $30\,\mathrm{mW}$ to $2.7\,\mathrm{W}$ whilst retaining the original frequency.
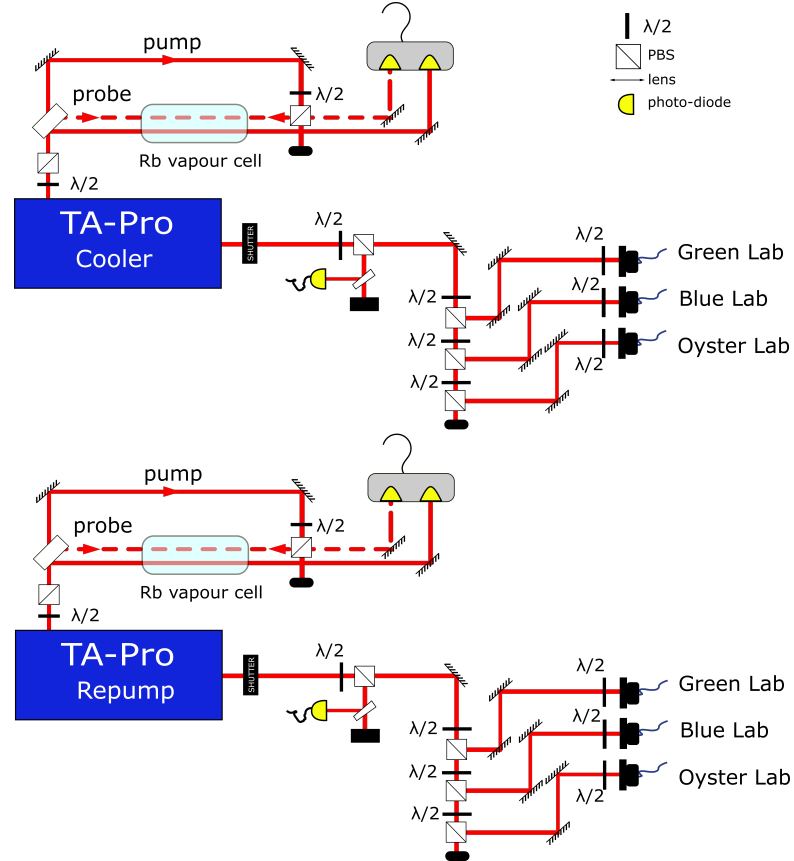

FIGURE 3.2: Optical set-up of laser system in the laser lab. Both the cooler and repump lasers have the same set-up, a pick off beam is taken after the laser diode to be used for spectroscopy. Immediately after the main output we dump excess power and a pick off a small proportion of the beam to monitor the power output with a photodiode (PD). The main beam is then distributed via optical fibres amongst the three laboratories.

Frequency stabilisation

The frequency can be stabilised using active feedback, typically referred to as "locking". There are number of techniques to perform frequency locking, naming a few, modulation transfer spectroscopy [100], magnetic field dithering [101], and polarisation spectroscopy [102]. In our experiment we use standard frequency modulation spectroscopy [103]. This method uses the atomic absorption spectrum as a

frequency reference and requires the output frequency to be modulated in order to generate an error signal. To generate a frequency reference we perform Doppler-free saturation spectroscopy [104] on a rubidium vapour cell (with an enhanced population of the ^{87}Rb isotope), to extract an absorption spectrum. We also obtain the Doppler-broadened spectrum to subtract from the Doppler-free spectrum to cancel out common noise. The laser output frequency is modulated by dithering the laser diode current with a low amplitude sine wave at $40\,\mathrm{kHz}$. This modulates the amplitude of the transmission signal seen on the photodiode. The signal from the photodiode is then demodulated by mixing with the dither signal, producing an error signal that is proportional to the derivative of the absorption profile. With the error signal obtained standard PID electronics are used to feedback on the laser diode current, this hardware is built-in to the laser controller provided by Toptica. The zero crossing of the error signal will correspond to a peak in absorption profile, thus locking can be performed on resonance with a transition or at a crossover resonance (see [104] for the definition of a crossover resonance). Our cooler laser is locked to the $|F = 2\rangle \rightarrow |F' = 1 \otimes 3\rangle$ crossover resonance, and our repump laser is locked to the $|F = 1\rangle \rightarrow |F' = 1\rangle$ transition Fig. 3.1.
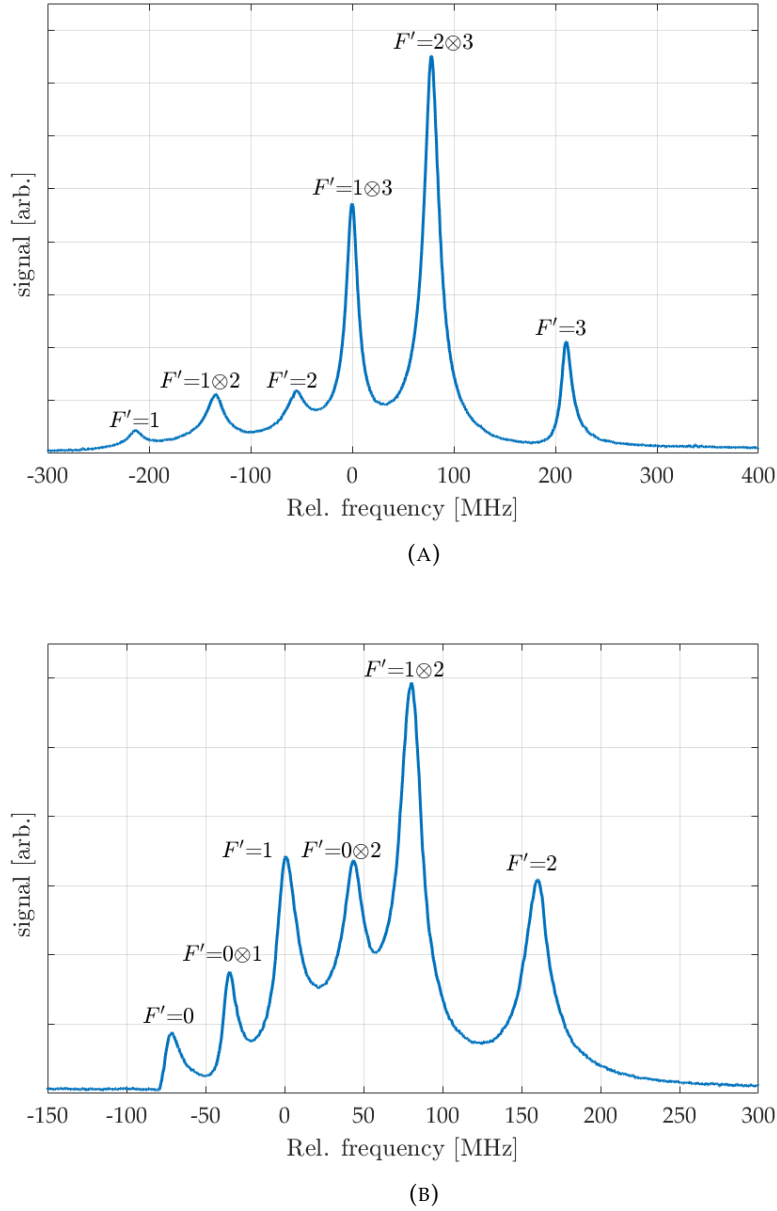
(A)

(B)

FIGURE 3.3: Doppler-free absorption spectroscopy signal of the (A) cooling transition $5^2S_{1/2}\,|F=2\rangle \rightarrow 5^2P_{3/2}\,|F'=1 \otimes 3\rangle$ and (B) the repump transition $5^2S_{1/2}\,|F=1\rangle \rightarrow 5^2P_{3/2}\,|F'=1\rangle$.

Power stabilisation

Power stabilisation is a much simpler process; an error signal can be extracted directly from the output of a photodiode as it varies monotonically with the laser power. The power is locked at three locations, first after the TA-Pro output in the laser lab to ensure the power supplied to each sub-laboratory is stable, second after the BoosTA in the Green lab (see Fig. 3.4) this corrects for any residual variations such as polarisation that can occur after passing through a $15\,\mathrm{m}$ optical fibre, and finally after a fibre

located next to 3D MOT fibre couplers in the Green lab (see Fig. 3.4) which deals with local variations due to optics (e.g. mirror mount instability). At the first two locations we feedback on the current supplied to the TA chip within the TA-Pro/BoosTA. For the third location feedback is applied to the voltage-controlled amplifier (VCA) which controls the power output of the acousto-optic modulator (AOM) used on the cooler light (see Fig. 3.4). The third location is the most important as this has the most influence on the MOT beam powers, power variance here will have a knock-on effect which will ultimately cause the BEC atom number to fluctuate. The ideal location to perform feedback would be at the MOT fibre outputs (which send light directly into the vacuum chamber) this could be done with an electronic variable optical attenuator.
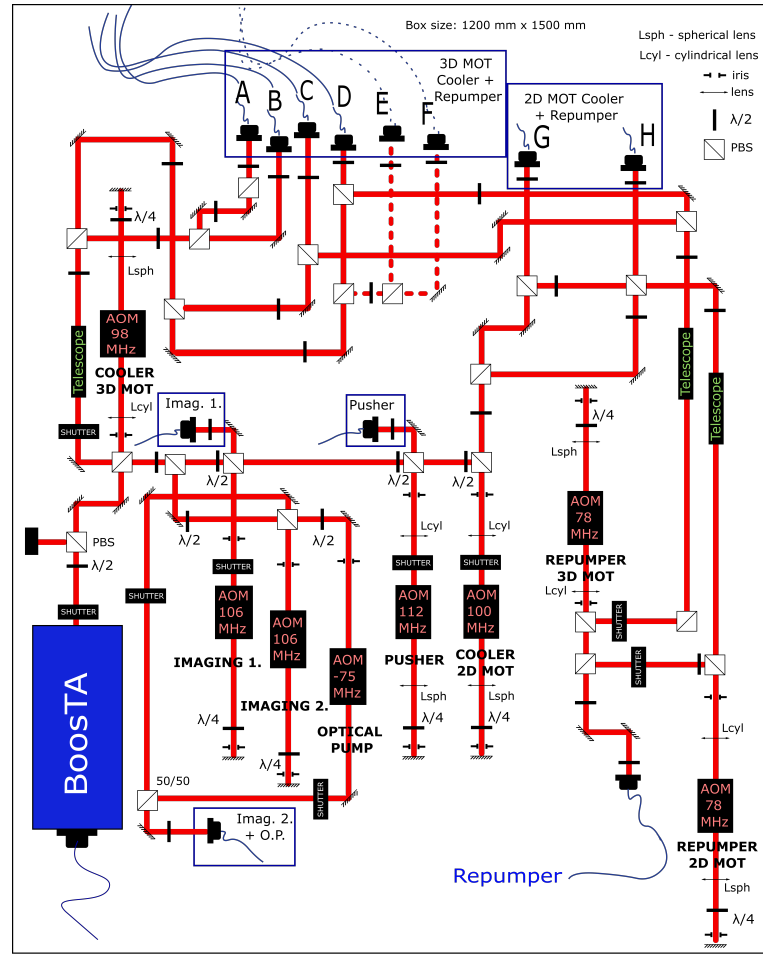

FIGURE 3.4: Schematic of the optics distribution for laser light preparation in the Green lab.

3D MOT

We utilise a four beam mirror-MOT configuration [54] where two of the cooling beams are reflected off the surface of the atom chip. A $45°$ rotated quadrupole field is created with the under-structure (see Section 3.2.1) and an external bias field. When well-optimised, in combination with the 2D MOT (discussed in the next section,

Section 3.1.1) $>2\times10^9$ atoms can be loaded in $4\,$s. When well-aligned $2\,$s MOT loading is long enough to saturate the atom number loaded into the magnetic trap, however for the sake of stability we load for $4\,$s. Our lab has air conditioning that performs poorly, whilst it does cool the room it displays periodic ($\sim30\,$min) variations with temperature swings of $\sim6\,°$C. The large temperature fluctuations are detrimental to BEC stability (in terms of atom number and temperature), after extensive characterisation we find that the stability is best without the air conditioning on. As in normal operation our laboratory is not temperature controlled, we observe the fibre coupling drift over the course of the day due to temperature drifts, loading for an extra $2\,$s ensures the atom number loaded into the magnetic trap is less sensitive to the temperature fluctuations.

2D MOT

We employ a 2D MOT to pre-cool the rubidium atoms before loading into the 3D MOT located in the science chamber. It is advantageous in that it allows a region of high rubidium partial pressure in the 2D MOT for capturing many atoms, and keeps the pressure low in the science chamber which reduces the background collision rate and improves the evaporate cooling (see Section 2.1.2). The introduction of the 2D MOT dramatically decreased our MOT loading time from $30\,$s to $4\,$s, and increased the loaded atom number from 4×10^8 to $\sim 1 \times 10^9$. A measurement of the loading rate is shown in Fig. 3.5, an apparent two-step loading rate is observed when using $100\,$mW per beam. It is worth noting that absorption imaging for such large atom numbers can become unreliable due to the limited field of view of the imaging, and the irregular shape and high densities of the cloud. These factors can invalidate the assumptions made in Eq. (3.4), and/or the applied fitting function Eq. (3.5).

We are lacking an accurate measurement of the atom number in the 3D MOT as the cloud is simply too large at sufficient time of flight to reduce the density below saturation of the optical depth. Measuring it would require designing a new imaging system with lower magnification, however ultimately we care about the number of atoms loaded onto the atom chip (see Section 3.2.3) and therefore it was deemed not to be essential. Details of the design, working principles, and an in-depth analysis of the performance can be found in chapter 7 of [39]. Highlighting the use of new technologies, the optical and magnetic mounts were 3D printed, which allowed us to easily replicate the design in another laboratory. For the interested reader, more information can be found about 2D MOTs and their implementation in cold-atom experiments in [105–107].
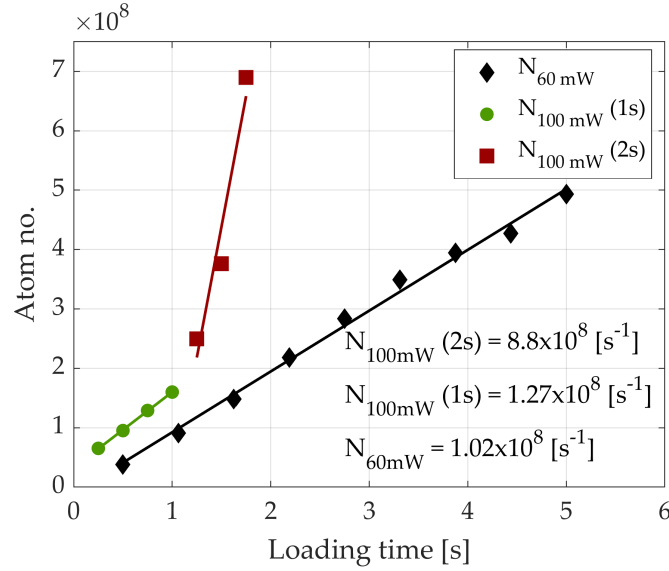
FIGURE 3.5: Atom number vs loading time, for different powers of the cooling laser beams in the 2D MOT. Initially only $60\,\mathrm{mW}$ per beam was used (black, diamonds), after increasing to $100\,\mathrm{mW}$ we observed an increase in atom number, and that the loading curve became non-linear, after the first second (green, dots) we measure $\sim 2 \times 10^8$ atoms, and after $2\,\mathrm{s}$ (red, squares) roughly 1×10^9. We deem that a loading rate of $5 \times 10^8\,\mathrm{s}^{-1}$ is a reasonable assumption.

3.1.2 Vacuum system

Figure 3.6 shows the vacuum system before external connections and bias coils have been added, the main features have been annotated. We use an off-the-shelf spherical octagon with a CF100 port on the top to house the electrical feed-through, and on the bottom such that there is large area of optical access for the mirror MOT beams. The picture was taken after bake-out, which was carried out over seven days with a maximum temperature of $160\,°\mathrm{C}$. A bake-out tent was used, this encases the whole chamber and acts as would an oven. The bake-out tent provides excellent temperature control and homogeneity, both problems that often occurs with the more commonly used method of applying heat tape and wrapping the chamber in aluminium foil. The tent was custom built to fit our system, and whilst time consuming to design, once built it was quicker and easier to use.
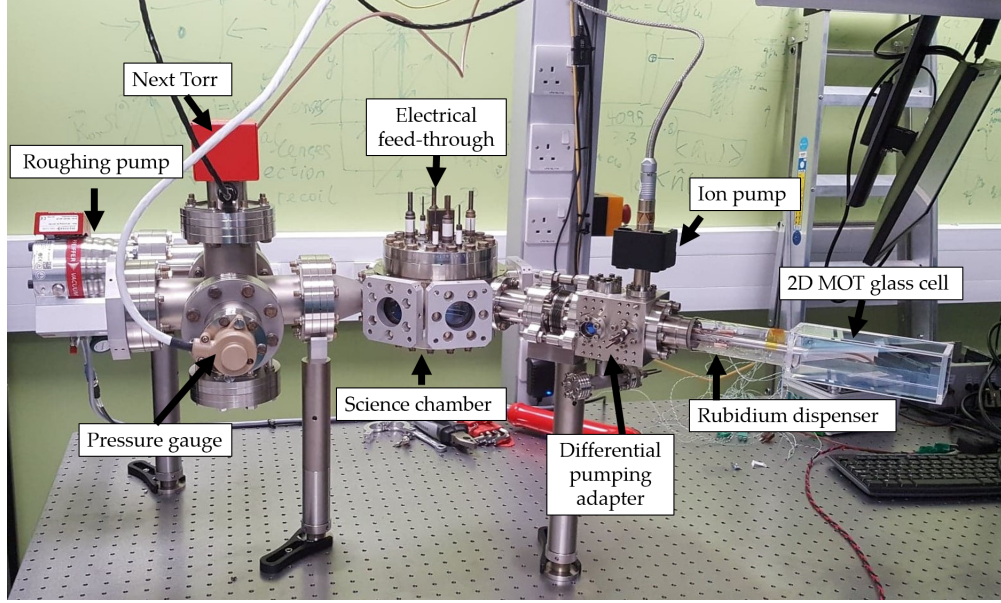
FIGURE 3.6: Vacuum chamber post bake-out, before addition of bias-coils and cable connections.

Pressure in the science chamber is kept to 2×10^{-10} mbar, which is typically quite high for experiments of this nature. We suspect the reason for the high pressure is due to two high density Sub-D[1] (also known as D-sub) connectors located in our feed-through, they both contain 50 pins each capable of carrying roughly 9 A, they are used to supply currents to the PCB and atom chip (see Section 3.2). A standard helium leak detection test points to the D-sub connectors as a potential source of leak in our chamber. Similar behaviour was observed in other laboratories with the same connectors. The poor vacuum limits the atoms lifetime in the magnetic trap to about 10 s, the measurement is shown in Fig. 3.7. Fortunately this low lifetime is not a major issue as RF cooling can be performed sufficiently well in 8 s, leaving around 1×10^5 atoms in the final BEC (see Fig. 3.38).
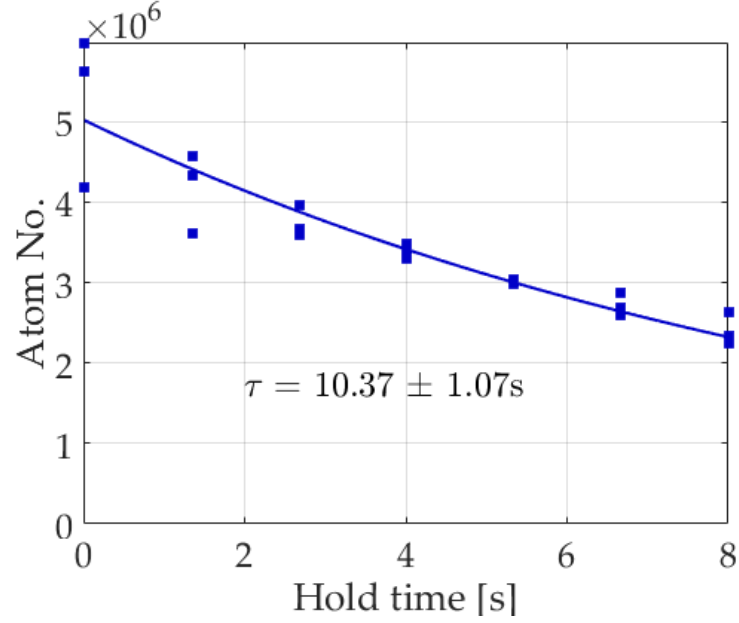
---

[1] Allectra 218-D50-SS-HC

FIGURE 3.7: Measurement of the lifetime of a thermal cloud in the copper-Z trap, atoms are cooled to a temperature of a few µK in a trap with truncation parameter $\eta >10$ and the hold time varied. The lifetime τ, is extracted from a fit to $N(t) = N(0)\exp(-t/\tau)$.

3.1.3 Bias coils

To provide homogeneous bias fields we use coil pairs in Helmholtz configuration. Figure 3.8 shows the positioning of the coils in relation to the science chamber. Using 3D modelling and magnetic field simulations to optimise the geometry we were able design a compact formation that gave us a high field to current ratio and thereby reduce power consumption, without the need for active cooling.

The largest bias field required is along the x-axis, it needs to cancel the large fields produced from the central bar of the copper-Z, and they are both large in order to attain the high field gradients desired for trapping (see Section 2.1.1). We are able to produce fields >100 G without heating the coil above $\sim45\,°\mathrm{C}$ eliminating the need for water cooling. A custom rig was built to wind the enamelled copper wire about the holder, this allowed us to efficiently pack the volume with conductor, true to the simulation. The coil holder for the vertical (z-bias) was 3D printed which gave us more flexibility in the design allowing us easily mount to the chamber, it was also manufactured in a few days, substantially quicker than mechanical workshop times for metal parts.
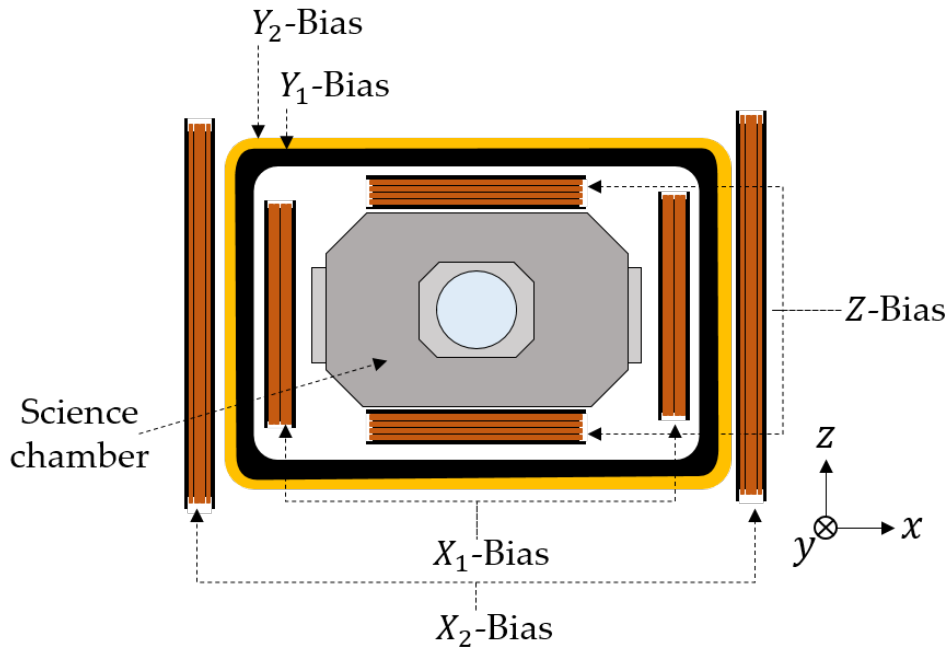
FIGURE 3.8: Arrangement of bias coils with respect to the science chamber (not to scale). Two x-bias coils provide fields for the MOT, magnetic trapping, optical pumping, and imaging. Two opposing y-bias coils provide fields in the MOT, Ioffe and anti-Ioffe fields (see Section 2.1.1). One z-bias coil is used for MOT fields.

Two x-bias coils are required due to the short time ($\sim 3\,\text{ms}$) and large variation in field ($\approx 100\,\text{G}$) required from MOT bias field, optical pumping field, and magnetic trap bias field. Whilst ensuring that the fields are switch on/off in $>1\,\text{ms}$. The two y-bias coils provide fields in the Ioffe and anti-Ioffe directions, and the z-bias is mainly used to control the position of the MOT.
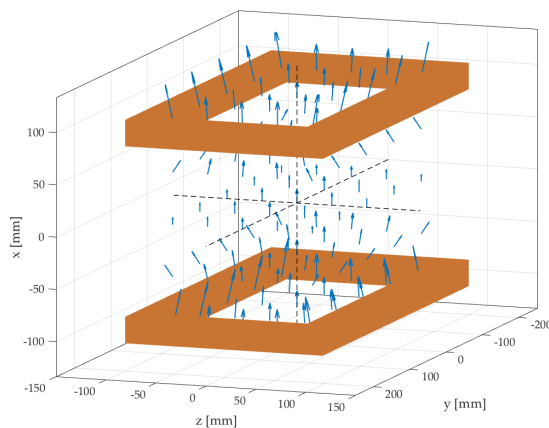
(A)
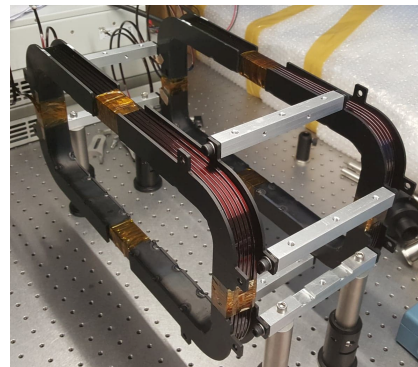
(B)

FIGURE 3.9: (A) A plot from the magnetic field simulation used to determine optimal size and location of the x-bias coil pair. (B) Image of the assembled coil pair.

3.1.4 Control and monitoring system

As is common to all cold atom experiments, there is a requirement for precise control over a range of different equipment. Power supply units that provide electrical currents for all the trapping structures, AOMs that control the frequency and power of the laser beams, and waveform generators to perform RF cooling. It is essential that they can be run in parallel, and can be switched on/off quickly and simultaneously. The control system we use is called Advanced Real-Time Infrastructure for Quantum (ARTIQ) [108]. It is an open source programming software written to interface between fully programmable gate array (FPGA) based hardware. The modular set of hardware comes from open-source hardware ecosystem called Sinara [109]. A detailed description of the ARTIQ system can be found in chapter 5 of [39].
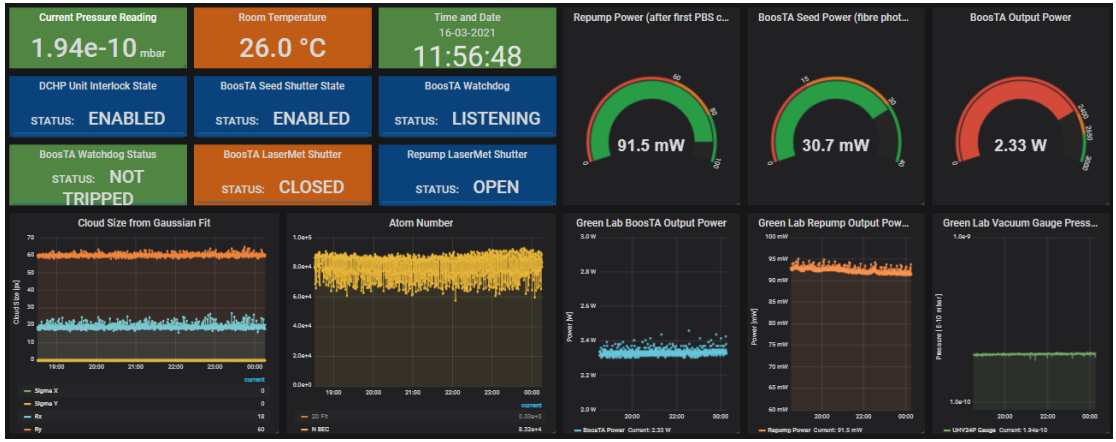

FIGURE 3.10: Dashboard of our online monitoring system visualised by Grafana.

We use real time monitoring of the laboratory conditions for diagnosis of malfunctions or unexpected behaviour. Using multiple micro-processors around the lab we collect data on beam powers, temperatures, atomic cloud properties, vacuum pressure, and electrical currents. These data are uploaded in real time to an online database influxDB [110] and then visualised on Grafana [111], a web based tool that can be accessed anywhere with an internet connection. This has allowed us to perform safe remote operation of the experiment, which has been essential over the lockdown period due to COVID-19. Further details on the monitoring network can be found in [112].

3.2 Trapping structures

Our experiment contains three different components for magnetic trapping (excluding bias coils) an under-structure, PCB, and an atom chip, see Fig. 3.11. This section describes each structure and the principles guiding their design. The typical size of the trapping wires on each component reduces in size from centimetre to micron scales. Each structure is stacked on top of each other with the largest structures (which have highest current capacity) located the furthest away from the trapped atoms, see Fig. 3.11c. The main principle (as will be discussed in more detail), is that throughout the cooling sequence the scale of the trapping structures matches that of the atomic cloud, thus providing an efficient transfer from a large relatively hot cloud (MOT, T $\approx$60 µK, $\sigma_{y,z} \gtrsim 1$ mm) to a small cold cloud (BEC, $R_y = \sim$100 µm, $R_z = \sim$1 µm).

(A)

(B)

Atom chip
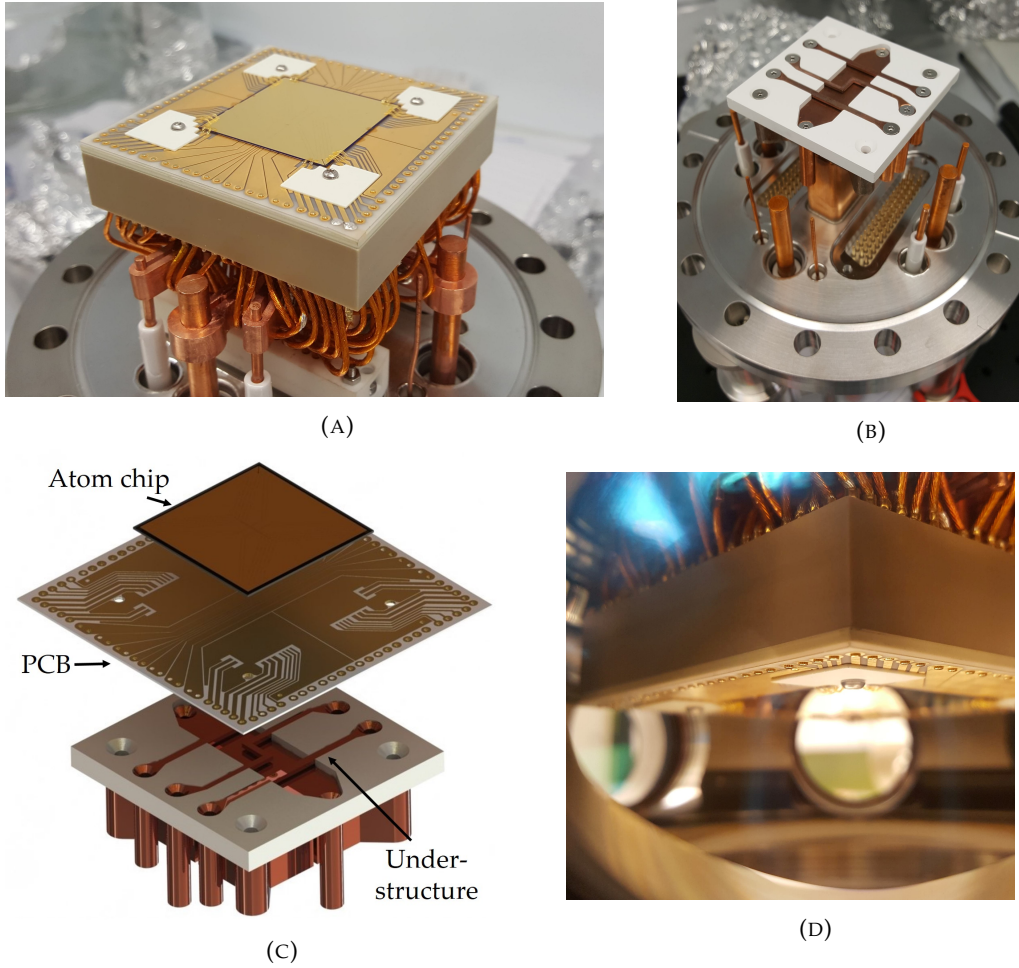
PCB

Under-structure

(C)

(D)

FIGURE 3.11: (A) Assembled electrical feed-through, atom chip and PCB can be seen on top. (B) Under-structure shown before PCB and atom chip have been added. (C) Exploded view of the trapping structure assembly showing atom chip, PCB, and under-structure. (D) View of assembled electrical feed-through inside the science chamber.
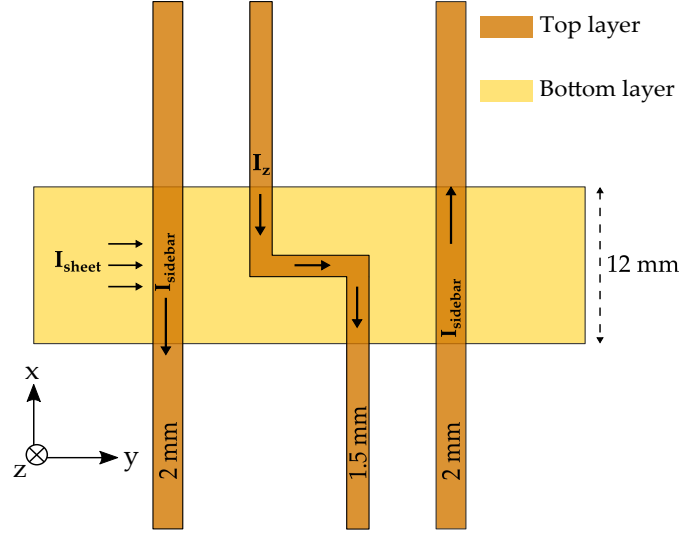
3.2.1 Under-structure

FIGURE 3.12: Schematic of under-structure. On the bottom layer is the sheet which when combined with an x-bias field provides the quadrupole field in the x-z plane for the MOT, and the sidebars (on the top layer) generate the MOT field in the y-z plane. Also on the top layer is the Z track, which is used in the pure magnetic trap.

The copper under-structure consists of a z-shaped conductor, two sidebars which run parallel to the legs of the Z, and a broad sheet running perpendicular to legs. We use the sheet and sidebars with an external bias coil to create the quadrupole field for the MOT. The broadness of the sheet improves the quality of the quadrupole field produced, as the eigenaxis remain at $45°$ over a larger volume than they would if it was a narrow wire [58]. The MOT is then compressed and undergoes sub-Doppler cooling. After cooling we atoms transfer into an Ioffe-Pritchard type magnetic trap made using the copper Z and an external bias coil. The MOT cloud is large (N = 1×10^9) and relatively hot (T $\approx 60\,\mu$K). To optimally transfer the atoms from MOT to magnetic trap we follow the concept of mode matching. This process aims to maximise the phase space density, ρ, [63] $\rho = n(0)\lambda_{\text{dB}}^3$, where $n(0)$ is peak atomic density, and $\lambda_{\text{dB}} = \sqrt{2\pi\hbar^2/mk_{\text{B}}T}$ is the thermal de Broglie wavelength. A large ρ will also mean a high elastic collision rate which will improve the efficiency of RF cooling (see Section 2.1.2). Maximising the phase space density requires us to keep atom number high and temperature low. To maximise N a useful quantity to know is η, the ratio between trap depth and T a high η will suppress atom loss from spilling and plain evaporation. To minimise the heating during transfer the final and initial trapping potentials should have the same shape and position. To maintain a Gaussian density distribution from the MOT, the atomic cloud must be transferred in the magnetic trap whose harmonic frequencies are given by,

$$\omega_j = \sqrt{\frac{k_{\text{B}}T}{m\sigma_j^2}}, \tag{3.1}$$

where σ_j is the RMS width of the cloud in the jth dimension ($j \in \{x, y, z\}$). In our sequence after compression and sub-Doppler cooling the MOT has temperature $T \approx 60\,\mu K$, and sizes $\sigma_x = 1600\,\mu m$, and $\sigma_y = \sigma_z = 700\,\mu m$. Thus, the mode-matching procedure determines the ideal initial magnetic trap frequencies to be $(\omega_\parallel, \omega_\perp) = 2\pi \times 8\,Hz$ and $2\pi \times 16\,Hz$, and a trap depth of $\geq 600\,\mu K$. In practice it is difficult to achieve these values, as increasing trap depth generally increases the trap frequencies, the best parameters are found with large fields far from the trapping wire. This requires very high currents, meaning large copper structures are needed to support them.
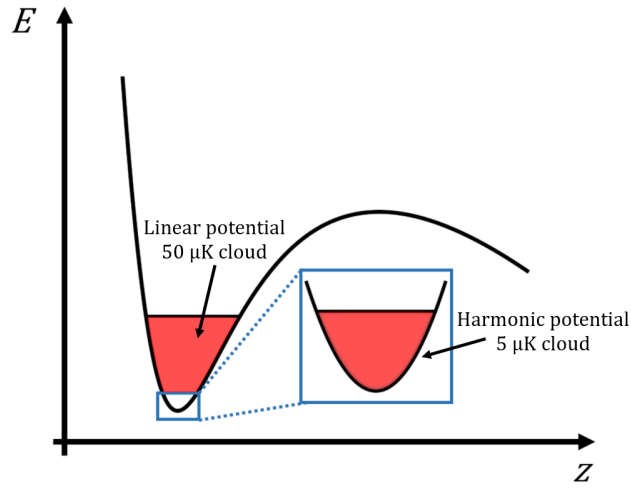

FIGURE 3.13: Schematic showing the difference of the trapping potential in the regions sampled by a hot and a cold cloud.

It is worth noting that the mode matching process breaks-down slightly as the potential generated by the trapping structures is only harmonic in a small region about the trap minimum. Far away from the minimum the potential becomes linear. As such, hotter clouds predominantly sample the linear part of the potential and therefore the trap is better characterised by a field gradient rather than a frequency. Whereas the converse is true for cold clouds (e.g. BECs), a schematic is shown in Fig. 3.13. Practically, the loading of the magnetic trap is often found optimised empirically, but the parameter η and frequencies from Eq. (3.1) can be used as an initial starting point. The control parameters are then adjusted to maximise the final phase space density. In our experiment we find that a high trap depth is more important than well-matched trap frequencies, because this results in larger captured atom number, allowing more flexibility to counteract any induced heating with evaporative cooling in the following stage.

Thermal management is often very important in cold atom experiments. Electric current flow through a wire causes joule heating, and as by-product can cause them to deteriorate (particularly on the atom chip), and if allowed to get too hot will melt. However more likely is that thermal expansion will become problematic before

reaching the melting point, the expansion causes stress on the structures and can lead to bad connections, short-circuits, and in the worst-case expand into to the atom chip/PCB and cause it to crack. High temperatures can also cause material to out-gas and hence degrade the vacuum. As stated above we require high currents in our under-structure so to prevent unwanted heating the trapping wires are embedded in Boron Nitride, which is electrically insulating, with a good thermal conductivity $30\,\mathrm{W\,m^{-1}\,K^{-1}}$. This is then secured to a large copper block that projects outside the vacuum chamber (copper has a thermal conductivity of $401\,\mathrm{W\,m^{-1}\,K^{-1}}$) acting as a heat sink to draw heat out of the chamber. The importance of thermal management is discussed in more detail in the next section as it is a key component in the design process.

3.2.2 Printed circuit board (PCB)

The main purpose that the PCB was designed for was to act as an intermediate trapping stage between the under-structure and the atom chip. The medial size of the PCB would allow us to create trapping fields that well match with both. Thus helping us follow the mode-matching principle of maximising the phase space density, which in turn improves atom number and cycle time. We designed it with compactness in mind, with the hope that it might be able to replace the under-structure. A MOT was produced with PCB alone, however the atom number was significantly lower, proper characterisation was not undertaken. The feasibility of replacing the under-structure will be explored in the future with the second generation PCB Section 3.2.2. The currents required are much smaller as the trapping structures can be much closer to the atoms, this would remove the need for high current supplies and switches, which are expensive and bulky. It should also be possible to create a BEC directly on the PCB potentially bypassing the need for an atom chip. This would be a major advantage in terms of cost.

TABLE 3.1: Thermal conductivity and resistivity of common materials used in atom chip and printed circuit board technologies.

Material	Thermal conductivity [$\mathrm{W/(m\,K)}$]	Resistivity [$\Omega\,\mathrm{m}$]
FR4 [113]	0.34 (23 °C)	3×10^{13}
Rogers4003 [114]	0.71 (80 °C)	1.7×10^{14} (23 °C)
AlO [115]	18	10×10^{12}
AlN [115]	170	10×10^{12}
Copper [116, 117]	401 (0 °C)	1.724×10^{-8} (20 °C)
Si [116, 117]	168 (0 °C)	0.1 to 60 (20 °C)
$\mathrm{SiO_2}$	1.1	$\sim 1 \times 10^{15}$

PCB technology is well established for use in electronics and a PCB designed for atom trapping is structurally much simpler than what would typically be used in

electronics (there are no electrical components just wire traces). At first glance one might conclude that making such a PCB would therefore be not only simple but inexpensive. There are however some key requirements that mean that standard PCB materials are not suitable, and this complicates the design process. An atom trapping PCB needs to be UHV compatible, non-magnetic, and have a high thermal conductivity. The standard board material used in electronics is FR4 (a fibre glass material) and is not UHV compatible, typically the conductors contain nickel which is magnetic and needs to avoided for atom trapping. A common alternative is Rogers4000 (a type of ceramic laminate) it is UHV compatible and the boards can be fabricated with the same standard manufacturing processes as with FR4 (keeping costs low). Unfortunately, it has poor thermal conductivity, which severely limits the maximal electric current that can be sustained. For low electrical current requirements Rogers4003 [114] is good a option as there are a wealth of companies that are able to process it, and the cost of production remains low. For our purposes however high current capacity is needed (see Section 3.2.2 for more details on the current requirements) and therefore high thermal conductivity is essential. Aluminium nitride (AlN) is a ceramic material that is an ideal candidate, as it has a high thermal conductivity (see Table 3.1) and is an excellent electrical insulator. A number of groups have used AlN as substrate for their atom chips [118–121]. Normally the substrates are made of silicon which has good thermal conductivity but is electrically semi conductive, to prevent current flow into the substrate a thin layer of SiO_2 is used, which is electrically insulating but a poor thermal conductor. Figure 3.14 shows numerical finite element calculations of the time evolution of heat distributions, comparing FR4 and AlN materials as a substrate. After $6\,$s the temperature of the wire on the FR4 substrate increases by $20\,°$C as the heat hasn't been able to travel to the heat sink whereas with an AlN substrate the wire heats by only $1\,°$C as the AlN can quickly transport heat into the copper.
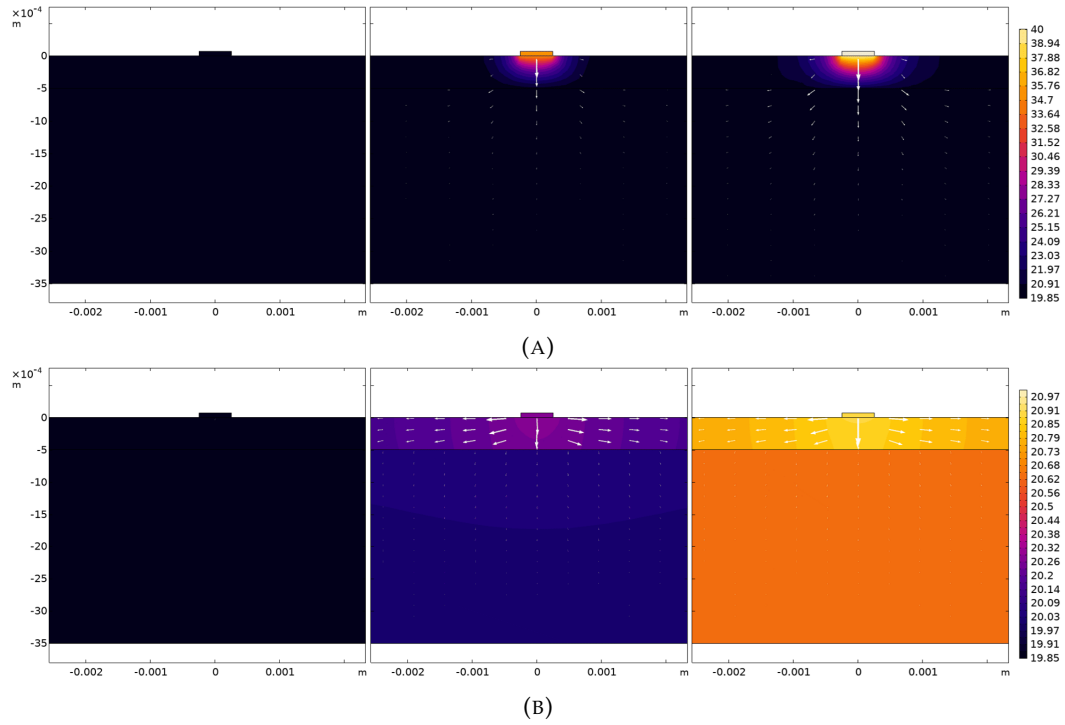
FIGURE 3.14: Time series plots showing the heat flow arising from joule heating of a $35\,\mu\text{m} \times 200\,\mu\text{m}$ Au wire carrying $2\,\text{A}$, on an FR4 (A) and an AlN (B) substrate attached to a large copper heat sink. Time steps (from left to right) $0\,\text{s}$, $1\,\text{s}$ and $6\,\text{s}$, with an initial temperate $20\,°\text{C}$, simulation was produced in COMSOL.

The main difficulty with AlN PCBs is in bonding copper to the AlN, the current method (direct copper bonding - DCB) is tricky and significantly more expensive partly due to the high temperatures required. At the time we were designing the PCB we found only one company in Europe who offered AlN (there were a handful of options in China and the USA). Even with the increased expense the PCB was still roughly ten times cheaper than commercially available atom chips. It also has the advantage that double layer PCBs are no more complicated than a single layer, the same cannot be said for atom chips. If the PCB can be shown to work effectively then it could significantly reduce costs and increase versatility.
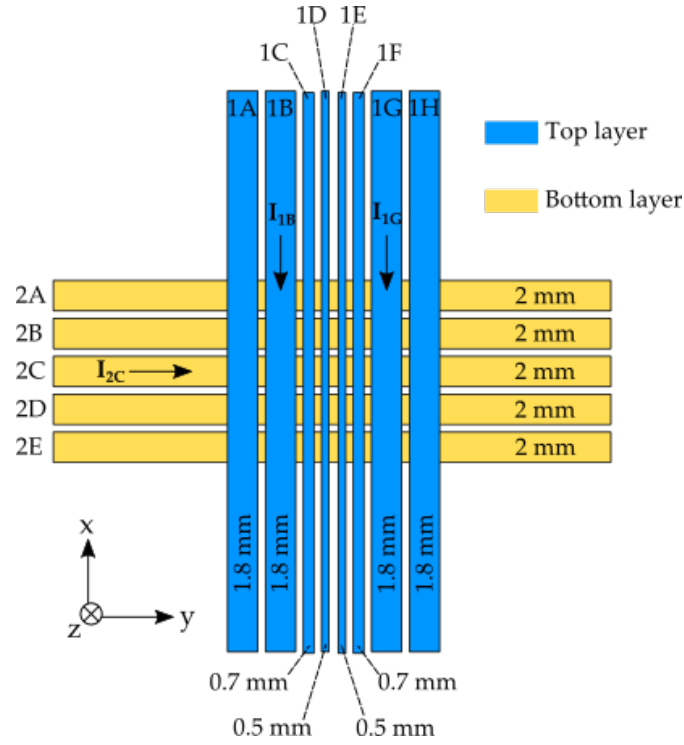
Version 1

FIGURE 3.15: Track layout of PCB, numbers in millimetres indicate the width of the track. A H-trap trap can be made with currents I_{1B} & I_{1G} for longitudinal confinement, and I_{2C} with an X-Bias for transverse trapping. All tracks are made of copper and have a thickness of $70\,\mu$m, which are bonded to AlN board.

Figure 3.15 shows the track layout on the double layered PCB. Tracks on the top/bottom run perpendicular/parallel to the main trapping wire on the atom chip - labelled as TE see Fig. 3.18 - the top layer being closest to the atom chip. The PCB was designed with a H-trap rather than a Z-trap configuration as this allows for independent control of the longitudinal, $\omega_{//}$, and transverse, $\omega_{\perp}$, trapping frequencies. This independent control enables a large tuneable range of aspect ratios, which was key for our experiment in Chapter 4.

The aim was to use the PCB throughout the whole magnetic trapping sequence. Transfer from the MOT using tracks 2A-2E with an x-bias field providing transverse confinement, and tracks 1A & 1H with an anti-Ioffe field for longitudinal confinement. The cloud would then be smoothly transferred into the chip trap, where the PCB top layer would provide longitudinal confinement. The bottom layer tracks could then be used to support the chip wire increasing transverse trapping frequency without having to bring the cloud closer to the chip surface or increasing the current in the wire as both of these become limited by fragmentation effects (see Section 3.2.3).

Unfortunately, grounding problems and electrical noise affected many of the PCB tracks. This severely reduced the lifetime of the magnetic trap and direct transfer of the

MOT cloud to PCB trap had to be abandoned. Attempts at creating a BEC solely with the PCB trapping wires also failed, efficient evaporative cooling of the cloud couldn't be maintained. We attribute this to a combination of limited lifetime and radial trapping frequency. The wires responsible for radial trapping(2B, 2C, & 2D) are located on the bottom layer of the PCB - furthest away from the atoms. This makes it difficult to get the high field gradients required. Supplying a maximum current of $25\,\mathrm{A}$ through these, and trapping $100\,\mu\mathrm{m}$ away from the atom chip surface the geometric mean trap frequency $\bar{\omega}$ is only $\simeq 2\pi\times\,90\,\mathrm{Hz}$. This would be sufficient if the cooling sweep was slow enough, though this requires a better quality vacuum.

Version 2

Due to fragmentation issues (Section 3.2.3) and the limited number of usable tracks on the atom chip (see Section 3.2.3) a new chip design was necessary. We decided to use this opportunity to also design a new PCB. Knowing the problems with the first design we decided to flip the layers around, with the radial trapping wires now closer to the atoms. Our simulation indicates $8\,\mathrm{A}$ through track 1C (and again trapping at a distance of $100\,\mu\mathrm{m}$) would be able to provide $\bar{\omega} > 2\pi\times\,200\,\mathrm{Hz}$. The radial trapping wires being closer to the chip surface also means that there is higher potential barrier to chip surface which means we could trap $<100\,\mu\mathrm{m}$ away, further increasing $\bar{\omega}$.

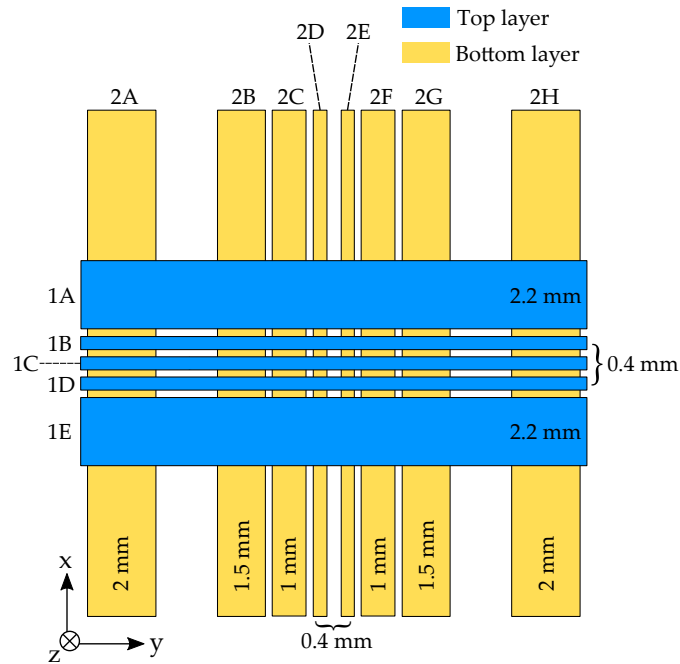FIGURE 3.16: Schematic of the second generation PCB. For magnetic trapping top layer tracks will provide transverse confinement when combined with an opposing x-bias, and the bottom layer tracks will deliver the axial confinement. Both layers can be combined to generate the MOT fields currently produced by the under-structure, tracks 1A to 1E acting as the sheet, and tracks 2A and 2H as the sidebars.

As the optimal MOT fields are now known, we were able to position the wires such that the fields produced by under-structure can be better replicated. If successful this will allow us to neglect the under-structure from future designs. This PCB has been manufactured and will be installed the next time the vacuum needs to be opened.
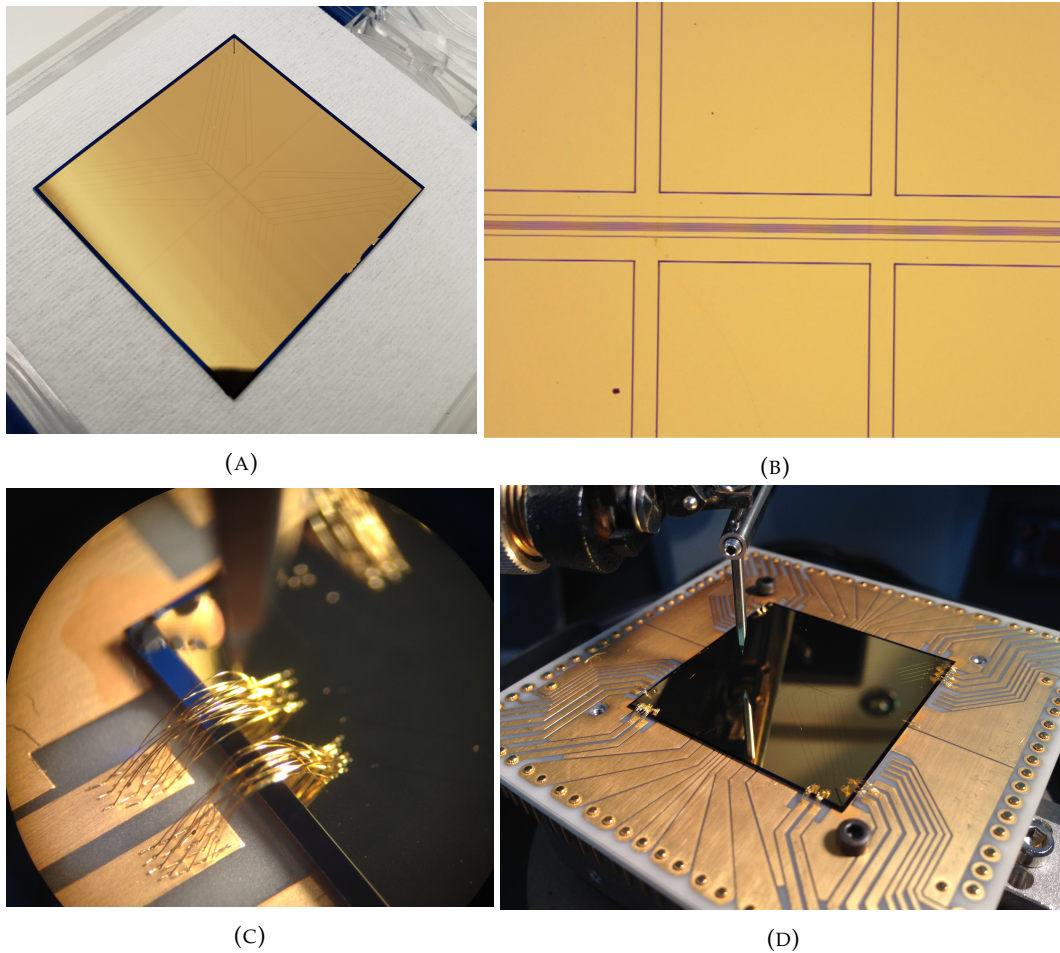
3.2.3 Atom chip

(A)

(B)

(C)

(D)

FIGURE 3.17

The atom-chip was fabricated by Dr Chris Mellor at the University of Nottingham. It has a Si substrate with an area of $35.5\,\mathrm{mm} \times 35.5\,\mathrm{mm}$ and a thickness of $280\,\mu\mathrm{m}$. The conducting surface layer is $2\,\mu\mathrm{m}$ thick Au, deposited by thermal evaporation, all gaps between tracks are $5\,\mu\mathrm{m}$. Tracks are connected to the PCB by Au wire bonds.

The design was intended to be flexible and allow us to create a number of different types of traps. Z and U configurations can be made on the $200\,\mu\mathrm{m}$ wide tracks using the appropriate, an H-trap configuration can be made but requires the PCB to provide longitudinal confinement. Multiple central wires were included in case of track failure during fabrication, but can also be used to perform RF-dressing [122]. Unfortunately we found shorts to ground on tracks NK, RH, and SG, due to remnant flakes of gold

between wires, left over from the lift-off process during fabrication. We also observed fragmentation (see Section 3.2.3 p.48) problems making many wires unusable. As a consequence this has limited us to a maximal radial trapping frequency, $\omega_\perp$, of about $1.4\,\text{kHz}$. The trapping potentials created for the experiment in Chapter 4 were made with a H-trap configuration, chip track TE was the main trapping wire providing radial confinement, and PCB tracks 1B & 1G performed as the legs to provide longitudinal confinement.
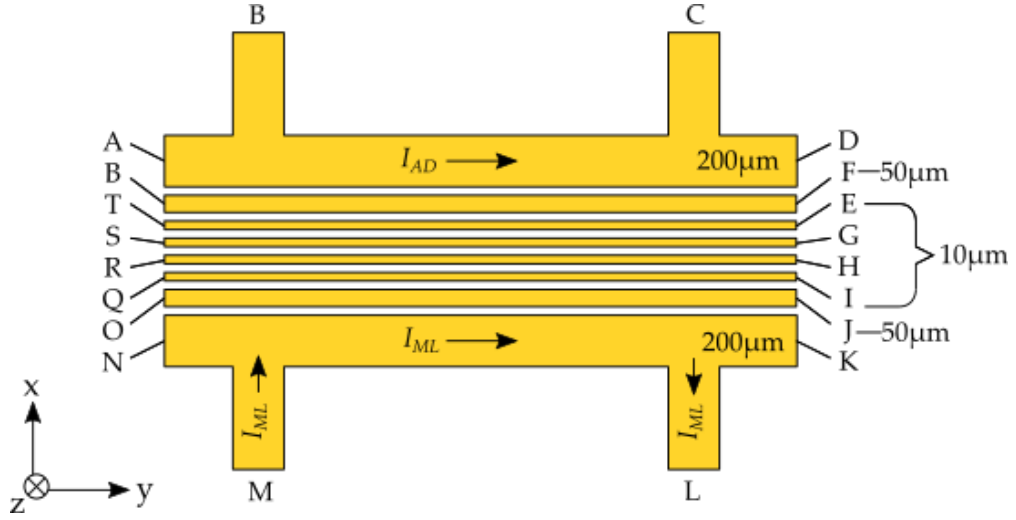

FIGURE 3.18: Track layout of atom chip. Grounding problems mean that tracks SG, RH, and NK are unusable.

Fragmentation

Fragmentation refers to unwanted break up of the atomic density [55, 123, 124], it occurs due to perturbations of the trapping potential. In wire/chip traps these perturbations arise from imperfections of the trapping wire that causes the electrical current path to meander [125, 126]. Wire imperfections come in a few forms, surface roughness, edge corrugations, and grain formation within the bulk of the conductor. Not surprisingly, fragmentation effects get stronger the closer the atoms are to the trapping wire. Improved fabrication techniques have been shown to greatly reduce the magnitude of fragmentation [57], they saw with the best quality chips it was possible to trap at heights of $10\,\mu\text{m}$, whereas early experiments had observed fragmentation at heights as large as $250\,\mu\text{m}$. Other methods to negate fragmentation effects have been successfully implemented, one way is to use AC currents [127, 128], and more recently digital mirco-mirror devices (DMD) were used to imprint a correcting optical potential [129].
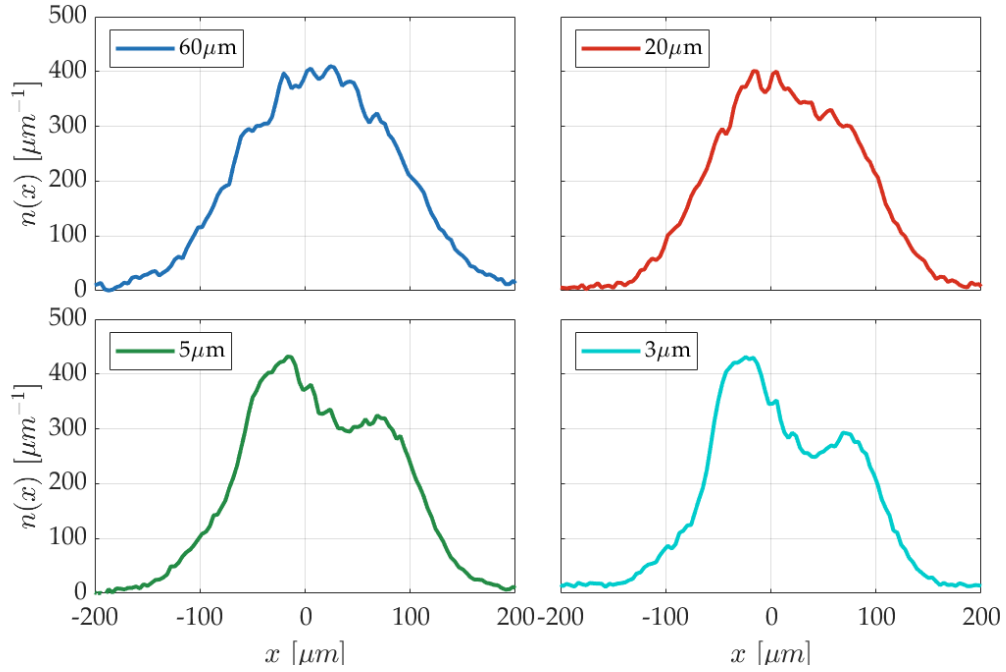
FIGURE 3.19: Fragmentation of a thermal cloud close to critical temperature ($T_{\mathrm{c}} = 450\,\mathrm{nK}$), trapped on a $200\,\mu\mathrm{m}$ wide wire. The cloud is made at a height of $60\,\mu\mathrm{m}$ from the surface of the wire and then ramped to its final height where it is held for $50\,\mathrm{ms}$ before imaging after $1\,\mathrm{ms}$ time of flight. Each profile is an average of five images after integrating vertically.

Figure 3.19 shows the atomic density profiles as a function of their height from the chip, demonstrating the effect of the fragmentation due to the imperfections of the trapping track AD on our atom chip. We observe smooth potentials up to a height of $\sim 30\,\mu\mathrm{m}$. In the experiment described in Chapter 4, atom chip track TE is used instead, fragmentation effects are observed at $< 100\,\mu\mathrm{m}$, however it is still possible to create traps with higher aspect ratios thus making it better suited for the experiment. We observe fragmentation at heights $> 150\,\mu\mathrm{m}$ on the two remaining $10\,\mu\mathrm{m}$ wide tracks, at this distance radial trapping frequencies are lower than what can be obtained on track TE. Whilst these tracks are not used for trapping, they can be utilised to perform RF-dressing which is currently an ongoing experiment in the laboratory.
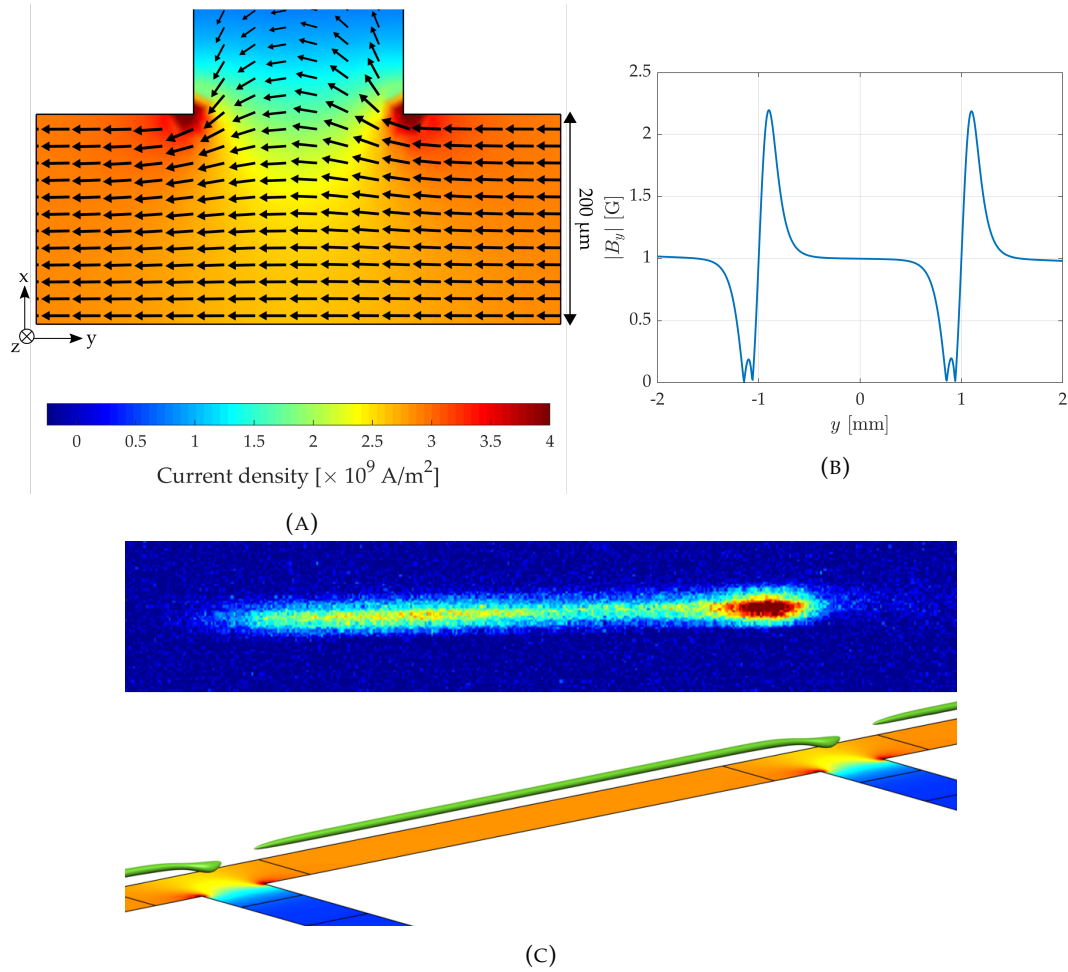
(A)

(B)

(C)

FIGURE 3.20: (A) Current density simulation produced in COMSOL of a T-junction on track AD with a current of $1\,\mathrm{A}$. (B) Trapping potential $|B_y|$ along the y-axis from $1\,\mathrm{A}$ through track AD and a $1\,\mathrm{G}$ bias field along y. (C) Isosurface of the trapping potential in (B) which showing the filling of well and an OD density image of the atom cloud after $1\,\mathrm{ms}$ time of flight.

One of the main issues with using track AD was the the T-junctions at B and C. They were included to give us the option to make extra trapping configurations, a U-trap could be made sending current from B to C, or a modified Z-trap by sending current from M to K and A to C. The problem was that the T-junctions create a path of lower resistance causing the current flow to bulge outward, as can be seen in Fig. 3.20a. The bulging effect creates a mini U-trap at the two junctions, and when combined with an homogeneous bias field (the Ioffe-field) this creates an asymmetric potential along the y-axis, where atoms trapped at edges will either see a potential well or barrier, see Fig. 3.20b. For a lot of traps the T-junctions are far enough apart that they have no observable effect on the atomic density, however when making traps with low $\omega_{\parallel}$ we observed clouds like that shown in Fig. 3.20c.

Bose-Einstein condensate microscopy

Observations of fragmentation in early experiments highlighted that BECs were extremely sensitive to small changes in magnetic field. Further investigation demonstrated that they could be used as a magnetic field microscope offering pT sensitivity with μm scale resolution [130, 131]. Since then BEC microscopy has been demonstrated several times [132–134]. A separate experiment in our group is working on microscopy [99], they are attempting to measure the current flow through samples of silver nano-wires and graphene. It was possible for us to demonstrate a much simpler example of BEC microscopy, by analysing the fragmentation of the BEC as it is scanned across the trapping wire. This allows us to visualise the location of imperfections in the atom chip track.
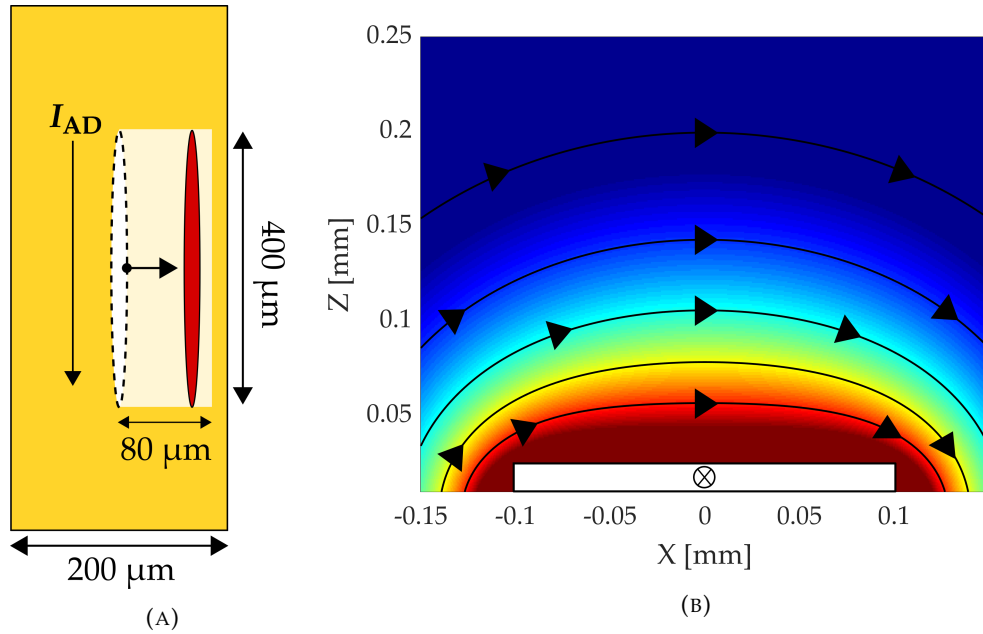

FIGURE 3.21: (A) Area scanned in the measurement shown in Fig. 3.22. The cloud is moved incrementally from the centre to the edge of the wire, a total distance of $80\,\mu\text{m}$ off-centre. (B) Magnetic field lines produced by the chip wire, adding a z-bias field will shift the trap minimum towards the edge of the wire. To keep the distance to the surface of the chip fixed the x-bias field must also be simultaneously reduced.

The scan was performed with clouds at three different temperatures, $T \gg T_c$, $T = T_c$, and $T < T_c$. The volume of the thermal cloud depends on the temperature, whereas below T_c the chemical potential becomes the important parameter. The transition appears as an increase in sensitivity which can be seen visually in Fig. 3.22.
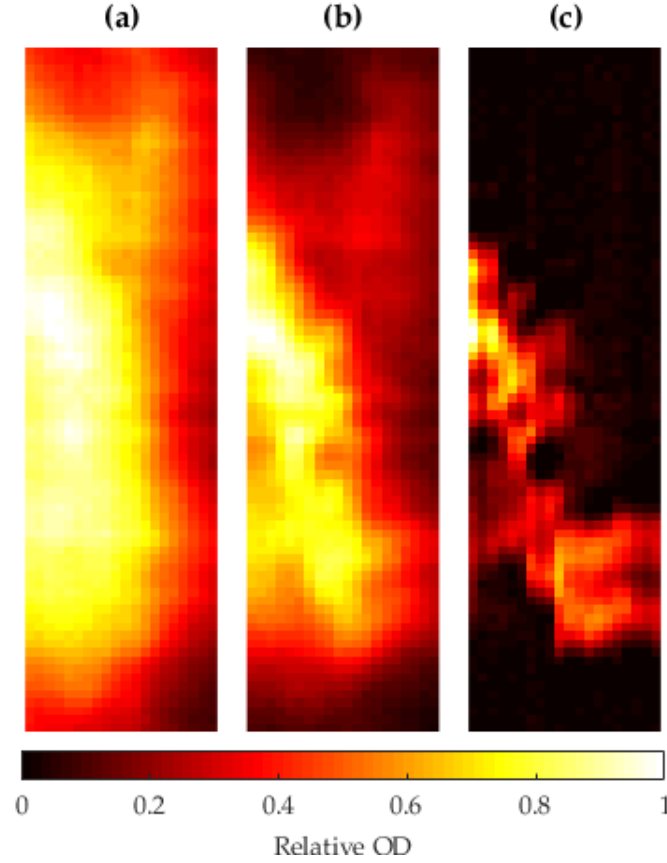
FIGURE 3.22: Microscopy of the $200\,\mu$m wide chip wire with varying temperature clouds which are held at an estimated distance of $1\,\mu$m from the wire surface. Each image scans an area of $400\,\mu$m $\times$ $80\,\mu$m, each column is an average of 20 images that have been vertically integrated. a) Thermal cloud $T =1\,\mu$K. b) Cloud at critical temperature $T = 0.45\,\mu$K. c) Bose-Einstein condensate $T = 0.2\,\mu$K.

3.3 Imaging

Our primary detection method employs standard absorption imaging techniques we also utilised fluorescence imaging to optimise the 2D MOT. In this section I will briefly highlight the key physics principles involved in absorption imaging, describe our imaging system, and discuss problems that are significant for the density ripple measurements in section 4.2.

3.3.1 Absorption imaging

Absorption imaging after time of flight is a very common technique amongst ultra cold atom experiments. The basic principle is to shine resonant probe light onto the atomic cloud and observe the reduction in light intensity from which the atomic density is extracted. Extraction of the atomic density is based on the Beer-Lambert law [38, 135, 136],

$$dI/dx = -n(x,y,z)\sigma_{\mathrm{sc}}I, \tag{3.2}$$

where I is the probe light intensity, x is the direction of propagation of the light, n is the 3D atomic density, and σ_{sc} is effective scattering cross-section. This defines the probability of absorption of an incoming photon [43],

$$\sigma_{\text{sc}} = \frac{\sigma_0}{1 + (2\delta/\Gamma)^2 + I/I_{\text{sat}}}, \tag{3.3}$$

where $\sigma_0 = 3\lambda^2/2\pi$ is the resonant scattering cross section, Γ is natural linewidth of the atom, δ is the detuning from resonance, and I_{sat} is the saturation intensity. In our experiment the imaging transition is from $|F = 2\rangle \rightarrow |F' = 3\rangle$ (see Fig. 3.1). If the probe light is unpolarised (or if there is no magnetic field present) transitions to all available m_F states are possible making a complex multi-level system. Accounting for the multiple levels σ_{sc} is modified by the average squared Clebsch-Gordon coefficient $(2F' + 1)/3(2F + 1) = 7/15$ [137]. However if circularly polarised light, σ^+, is used with a quantisation axis defined by a homogeneous magnetic field (we use $\sim 2\,\text{G}$) the transition is restricted to $|F = 2, m_F = 2\rangle \rightarrow |F' = 3, m_F = 3\rangle$, simplifying the system to two-levels. In the two-level case $I_{\text{sat}} = 1.67\,\text{mW/cm}^2$ for ^{87}Rb [135]. A detailed description of how to determine σ_{sc} when the two-level approximation isn't possible can be found in [89]. Attenuation of the light intensity is greatest at $\delta = 0$ enabling maximum signal to noise ratio, and dispersion effects (i.e. phase shifts) are suppressed, for these reasons imaging is performed on resonance. We also set the probe light intensity such that $I \ll I_{\text{sat}}$ which simplifies Eq. (3.3) to $\sigma_{\text{sc}} = \sigma_0$. Inserting this result into Eq. (3.2) and then integrating over the length of the cloud along x gives the definition of optical density, OD,

$$\text{OD}(y, z) = \sigma_0 n_{\text{2D}}(y, z) = -\ln\left(\frac{I_0(y, z)}{I_{\text{f}}(y, z)}\right), \tag{3.4}$$

where I_0 and I_{f} are the incident and output intensities, and $n_{\text{2D}}(y, z)$ is the two-dimensional column density. Hence, to extract optical density one must measure the intensity of the light beam before and after the passing through the cloud. In practice three images are taken, atoms A, light L, and dark D. A contains information of I_{f} the probe light intensity after passing through the atoms. L contains information of I_0 where the image is captured with the probe light only. Finally D the dark image is taken without probe light or atoms, this captures all stray background light I_{bg} and is subtracted from both A and L. Figure 3.23 shows each of the images captured and the calculated optical density.
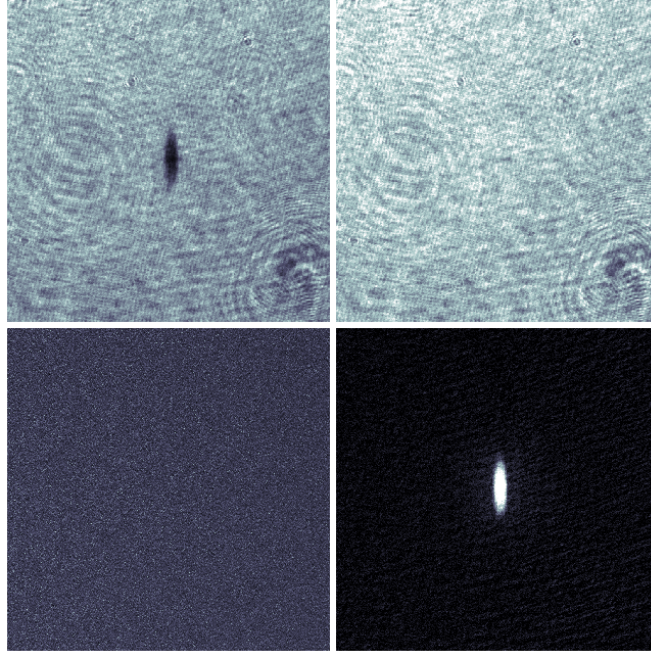
FIGURE 3.23: Atoms A (top left), Light L (top right), Dark D (bottom left), and the resulting optical density (bottom right) image.

Fringe removal

Captured absorption images often show undesirable fringes patterns. These come from imperfect propagation of the probe light along the imaging path, where slight misalignments can cause lens aberrations as well as interference and diffraction patterns. In principle, calculating A_k/L_k should remove all common fringes between A_k and L_k (when taking measurements many images are taken for statistical purposes, here k represents the image number within the total data set). In practice mechanical noise causes vibrations of the optical elements and hence lead to shot to shot variations of the probe intensity and not all fringes are removed. Figure 3.23 shows that whilst most large fringe patterns in the atoms and light images are removed in the final optical density image, remnant fringes remain. This is problematic for our density ripple analysis (see Section 4.2.1) as the size of fringes are similar to the features we are measuring.
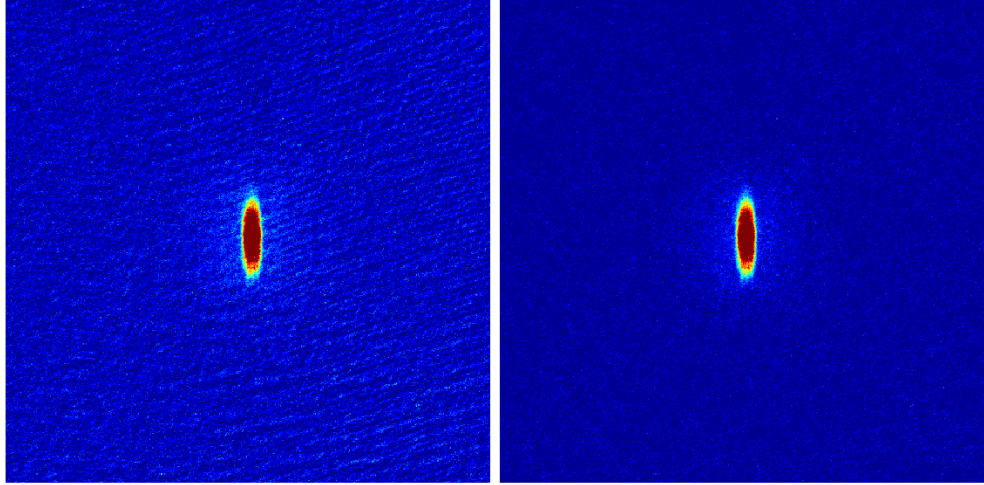
FIGURE 3.24: Optical density image of a Bose-Einstein condensate. (Left) original OD image. (Right) OD image after applying the fringe removal algorithm, it is very effective and no visible fringes remain.

To combat the imaging fringes, during post-processing we employ a fringe removal algorithm demonstrated in [138], this method is also advantageous in that it can reduce the photon shot noise. The basic principle of the algorithm is to construct a new optimal light image Q_k for every atoms image A_k using all of the light images available. Whereby the resulting optimal image Q_k is a weighted average of many light images, and instead of calculating A_k/L_k we use the optimal image A_k/Q_k. This fringe removal algorithm actually has a similar working principle to that of modern facial recognition algorithms [139]. Figure 3.24 shows the effectiveness of the procedure comparing the resulting optical densities calculated with/without application of the fringe removal.

Extracting cloud parameters

Once the OD images have been collected we need to convert them into atomic density, and apply a fitting procedure to extract the size, atom number, and temperature. Absorption imaging captures column density, the analytical formula for the column density can be obtained by integrating the formula for the 3D density along the imaging direction (x-axis). High temperature thermal clouds follow a Maxwell-Boltzmann distribution, leading to a Gaussian density profile with column density given by,

$$n_{\text{classical}}^{\text{2D}}(y, z) = \frac{N}{2\pi\sigma_y\sigma_z} \exp\left(-\frac{y^2}{2\sigma_y^2} - \frac{z^2}{2\sigma_z^2}\right), \tag{3.5}$$

integration along z gives the line density,

$$n_{\text{classical}}^{\text{1D}}(y) = \frac{N}{\sqrt{2\pi}\sigma_y} \exp\left(-\frac{y^2}{2\sigma_y^2}\right). \tag{3.6}$$

For clouds close to T_c the lower energy states become highly populated and quantum degeneracy effects can no longer be ignored. In this situation the distribution is given by a Bose-enhanced Gaussian. The column density of a Bose-enhanced Gaussian is given by [136],

$$n_{\mathrm{BE}}^{\mathrm{2D}}(y, z) = \frac{N}{2\pi\sigma_y\sigma_z g_3(\tilde{z})} g_2 \left[\tilde{z} \exp\left(-\frac{y^2}{2\sigma_y^2} - \frac{z^2}{2\sigma_z^2} \right) \right], \tag{3.7}$$

where $\tilde{z} = \exp(\mu/k_{\mathrm{B}}T)$ is the fugacity, and $g_k(x) = \Sigma_{n=1}^{\infty} x^n/n^k$ is the polylogarithm function. Again we obtain the line density by integration along z,

$$n_{\mathrm{BE}}^{\mathrm{1D}}(y) = \frac{N}{\sqrt{2\pi}\sigma_y g_3(\tilde{z})} g_{5/2} \left(\tilde{z} \exp\left(-\frac{y^2}{2\sigma_y^2} \right) \right). \tag{3.8}$$

To simplify the fitting procedure it is typically assumed that $\tilde{z} = 1$ as at T_c $\mu \approx 0$. For clouds with temperature $T \ll T_c$ in a harmonic potential where the Thomas-Fermi (TF) approximation is valid, the density is an inverted parabola. In this case the column density is given by,

$$n_{\mathrm{TF}}^{\mathrm{2D}}(y, z) = \frac{5}{2\pi} \frac{N}{R_y R_z} \max\left\{ 1 - \frac{y^2}{2R_y^2} - \frac{z^2}{2R_z^2}, 0 \right\}^{3/2}, \tag{3.9}$$

integration along z gives the line density,

$$n_{\mathrm{TF}}^{\mathrm{1D}}(y) = \frac{15}{16} \frac{N}{R_y} \max\left\{ 1 - \frac{y^2}{2R_y^2}, 0 \right\}^2. \tag{3.10}$$

In quasi-1D condensates ($\mu \ll \hbar\omega_\perp$) the 3D TF approximation is not valid as the kinetic energy is no longer much smaller than the interaction energy. As such, the kinetic energy term in Eq. (2.36) cannot be neglected. When the kinetic energy is much greater than the interaction energy, the wave function of the radial ground state is a Gaussian with a width given by the harmonic oscillator length $\sigma = a_\perp = \sqrt{\hbar/m\omega_\perp}$. Longitudinally, the TF approximation can still be valid (as $\mu \gg \hbar\omega_\parallel$), in which case the axial density profile remains an inverted parabola. In this case the line density is obtained by vertical integration of a Gaussian to give [140],

$$n_{\mathrm{q1D}}(y) = \frac{3}{4} \frac{N}{R_y} \max\left\{ 1 - \frac{y^2}{2R_{\mathrm{1D}}^2}, 0 \right\}, \tag{3.11}$$

where the cloud radius $R_{\mathrm{1D}} = \sqrt{2\mu_{\mathrm{1D}}/m\omega_\parallel^2}$ now depends on the 1D chemical potential $\mu_{\mathrm{1D}} = \hbar\omega_\perp \left(\sqrt{1 + 4an(0)} - 1 \right)$. For gases close to the 1D limit ($\mu \sim \hbar\omega_\perp$) the interaction and kinetic energy can be comparable and the radial wave function swells due to interactions. Here, the wave function takes the form of a Gaussian with a density dependent width $\sigma^2 = a_\perp^2 \sqrt{1 + 2an_{\mathrm{1D}}}$ [83, 141] (a measurement of the interaction-induced swelling was performed in [142]). The resulting axial density

profile was calculated in [83] and has the following form,

$$n_{\text{Gerbier}}(y) = \frac{\alpha}{16a}\left(1 - \frac{y^2}{L^2}\right)\left[\alpha\left(1 - \frac{y^2}{L^2}\right) + 4\right]. \tag{3.12}$$

where $\alpha = 2(\mu/\hbar\omega_\perp - 1)$, $L = \frac{a_y^2}{a_\perp}\sqrt{\alpha}$ is the length of the gas, and a is the s-wave scattering length. This formula works when the radial ground state is Gaussian Eq. (3.11) or Thomas-Fermi Eq. (3.10) and anywhere in between.

Temperature is extracted from a "fit to the wings", where Eq. (3.7) is fitted to the thermal component of the density profile after masking out the condensate fraction. Once the rms width of the Bose-enhanced Gaussian σ_i is extracted it can be used to calculate the temperature, T. A simple method would be to assume purely ballistic expansion during time of flight and which gives the time dependence of σ_i as,

$$\sigma_i(t_{\text{tof}}) = \sqrt{\sigma_i(0)^2 + \frac{k_{\text{B}}T}{m}t_{\text{tof}}^2}. \tag{3.13}$$

Assuming that the cloud has expanded to much greater than its initial size i.e. $\sigma_i(0) \ll \sqrt{\frac{k_{\text{B}}T}{m}}t_{\text{tof}}$ (which is true for hot clouds and long time of flight), we then get the simple expression for temperature,

$$T_{\text{Ballistic}} = \frac{m}{k_{\text{B}}}\left(\frac{\sigma_i(t)}{t_{\text{tof}}}\right)^2. \tag{3.14}$$

This is a useful assumption as it does not require knowledge of $\sigma_i(0)$ meaning T can be extracted directly from a single tof image. In reality, at early times of flight, where the mean free path is smaller than the cloud size, interactions still contribute and hydrodynamic expansion occurs [143], this can happen for elongated clouds and high densities. As atom chip traps are typically much longer in the axial direction, it is common that the mean free path is smaller than axial size but much larger than its radial dimension. This means that at early time of flight hydrodynamic axial collisions transfer energy to the radial degree of freedom. This creates a velocity imbalance that is proportional to the collision rate and hence dependent on the trapping frequencies $\omega_\perp$ and $\omega_\parallel$, leading to an anisotropic expansion such that $\sigma_\perp(t) > \sigma_\parallel(t)$. Accounting for the hydrodynamic expansion gives the following expression for temperature T [144],

$$T = \frac{2\tau_\parallel^2}{1 + 3\tau_\parallel^2}T_\perp + \frac{1 + \tau_\parallel^2}{1 + 3\tau_\parallel^2}T_\parallel, \tag{3.15}$$

where $\tau_i = \omega_i t$, and

$$T_i = \frac{m}{2k_{\text{B}}}\frac{\omega_i^2\sigma_i^2}{1 + \tau_i^2}. \tag{3.16}$$

The result means that to get an accurate temperature one must know the trap frequencies beforehand, and whilst this requires additional measurements it is not too

arduous as the frequencies are fixed and need only be measured once.

Imaging system

Our experiment uses two imaging systems that share the same mount but have switchable components so that we can alternate between two magnifications of the imaging system, this allows us to image atomic clouds depending on the cloud size throughout sequence effectively. For clarity I will refer to the two set-ups as high-magnification and low-magnification. Both the low-magnification and high-magnification imaging systems image the $z - y$ plane which captures the longitudinal and radial profile of the cloud (see Section 3.2.3 to see coordinates in relation to the atom chip). Both systems were initially numerically optimised using OSLO, a ray tracing program. External measurements of each system prior to installation were then carried out and free parameters adjusted for optimal resolution.
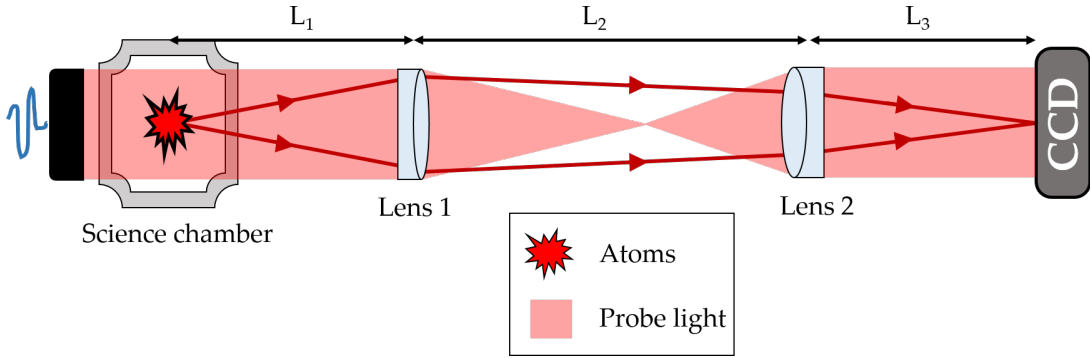

FIGURE 3.25: Schematic for both the low-magnification and high-magnification imaging system. Lens l1 (focal length $150\,\text{mm}$) is shared between the two systems, after lens l1 there is a removable lens tube that can be replaced with lens l2 (focal length $75\,\text{mm}$ low-magnification, $750\,\text{mm}$ high-magnification) and the camera of the low-magnification imaging system. For low-magnification imaging $(L_1, L_2, L_3) = (174, 225, 57)\,\text{mm}$, and for high-magnification imaging $(L_1, L_2, L_3) = (174, 500, 259)\,\text{mm}$.

The primary use of the low-magnification imaging system was during the optimisation of the stages up to and including the loading of the atom chip trap. Atomic clouds produced by the MOT and in the early stages of evaporate cooling have large atom numbers, it is necessary for the clouds to expand sufficiently during time of flight that the atomic density has reduced enough to prevent saturation of the optical density. Since these clouds are relatively hot ($50\,\mu\text{K}$ to $400\,\mu\text{K}$) this expansion can be considerable, the σ_i width can easily be a few millimetres and so to capture the whole cloud we demagnify the object. The camera for the low-magnification imaging system is a DMK 23U618 CCD (640×480 pixels of width $5.6\,\mu\text{m}$) placed within in a two-lens system (see Fig. 3.25 for a schematic). This set-up has magnification,

$M = 0.5$, with a field of view of $4.48\,\text{mm} \times 3.36\,\text{mm}$, a spatial resolution of $\sim 17.5\,\text{µm}$, and a depth of field of $\sim \pm 1$ mm.

The high-magnification imaging system is required when imaging BECs, as the cloud's size is typically a few $100\,\text{µm}$ and can display internal features (such as solitons and density fluctuations) that are smaller than $1\,\text{µm}$. In this scenario it is desirable to have a large magnification and a high imaging resolution. The high-magnification imaging system uses an Andor iXon Ultra 888 camera (1024×1024 pixels of width $13\,\text{µm}$) also in a two-lens system (see Fig. 3.25 for a schematic), external measurements give $M = 3.36$ yet in-situ M was measured to be 3.51. The 4% discrepancy is considered to be acceptable and attributed to slight differences between the external and in-situ set-up. The field of view is $3.79\,\text{mm} \times 3.79\,\text{mm}$, with a spatial resolution (Rayleigh criterion) of $11.7\,\text{µm}$, and a depth of field of ± 0.2 mm. All optical density images in Chapter 4 are acquired with the high-magnification imaging system.

3.3.2   Design of optical system

Principles of design

In general it is desirable to have an imaging system with as high resolution as possible, such that all features of the cloud can be resolved. There are a few definitions of resolution but the most commonly recognised is the Rayleigh criterion which gives the diffraction limited resolution and is defined as (in the paraxial approximation),

$$\Delta r_{\text{Rayleigh}} = \frac{1.22 \lambda f}{D} = \frac{0.61 \lambda}{\text{NA}}, \tag{3.17}$$

where λ is the wavelength of the probe light, f and D are the focal length and diameter of the first lens, and $\text{NA} = D/2f$ is the numerical aperture of the system. This would suggest maximising NA is very important, which means getting the first lens as close as possible to the atoms. Experimental groups have employed a number of different techniques to achieve this, such as recessed windows and translatable lenses [145], and even atom chips with integrated optics [146]. The NA will also be reduced if the beam is clipped before entering the first lens. This can be particularly problematic when imaging close to the surface of the chip. To get around this a common technique is to tilt the beam with respect to the chip surface and capture the reflected beam [147]. In our experiment we image after $34\,\text{ms}$ time of flight which is sufficiently large such that cloud is far enough away from the chip surface that we do not have to worry about clipping of the beam. One issue with optimising for resolution is a loss of depth of field (DOF), this is the distance along the optical axis over which an object can be imaged without significant blurring. The formula for DOF is given by,

$$\text{DOF} = \frac{\lambda n}{\text{NA}^2}, \tag{3.18}$$

where n is the refractive index of the medium. The depth of field is inversely proportional to NA^2 hence the depth of field rapidly reduces as the resolution is improved. For example in an experiment at the university of Heidelberg [148] they have developed an extremely high imaging resolution of $\Delta r_{\text{Rayleigh}} = 1.1(1)\,\mu m$ (which is - within error - the diffraction limit of their system), however the depth of field is only $6.8\,\mu m$. This is problematic for time of flight imaging as interactions due to tight radial confinement can cause huge radial expansion of the cloud. Trapping potentials with $\omega_\perp \approx 2\pi \times 1\,kHz$ will typically have a sub-micron radial size in-situ but after time of flight will quickly expand to become on order of hundreds of micrometres. As an example, in our experimental set-up, after $34\,ms$ of time of flight, the radial cloud size at the time of imaging can be up to $500\,\mu m$. At small depth of field the duration of the imaging pulse τ becomes significant. During the pulse atoms absorb and re-emit photons resulting in a net transfer of momentum from photons to the atoms. The effect pushes the cloud a distance, $\Delta x = v_{\text{rec}} R_{\text{sc}} \tau^2 / 2$, along the optical axis where v_{rec} is the recoil velocity and R_{sc} is the effective scattering rate. In our experiment $\tau = 50\,\mu s$ which gives $\Delta x = 2.2\,\mu m$, this is very small compared to our depth of field, however for high resolution imaging systems Δx can easily be on the order of the depth of field. The distance Δx can be reduced by decreasing the pulse length and/or the beam intensity but these both in turn decrease the signal to noise ratio.

High resolution imaging can be hard to implement, the ideal system can be simulated with numerical ray tracing software (such as OSLO and Zeemax) yet it often requires complex multi-lens systems and custom-built optics, rapidly increasing the cost and build time. Getting the experiment up and running as quickly as possible was deemed a priority, thus it was decided to compromise on resolution by using a simpler two-lens design with off-the-shelf optics to save on time. However, we have designed a new imaging system with better imaging resolution and plan to assemble and install it in the near future.

Lens aberrations

Another point is to make sure that the imaging beam and all optical components are well-aligned to the optical axis. The effects of misalignment however are not so obvious and are quite complicated. In general any misalignment will worsen the effects of lens aberrations and lead to defocusing, this section briefly summarises the common lens aberrations, for more detail I refer the reader to [149].

Lens imperfections or misalignment of either the object or an optical element can lead to aberrations. Looking at Fig. 3.26, in the ideal case all light should be focused at f_1 and the camera located at the image plane. Generally aberrations lead to the creation of secondary foci, for simplicity let us consider only one additional focus at f_2. Now using spherical aberrations (discussed in the next paragraph) as an example, central

rays will be focused at f_1 and peripheral rays at f_2. Placing a camera at the image plane will capture the central rays in focus however the peripheral rays will be out of focus.
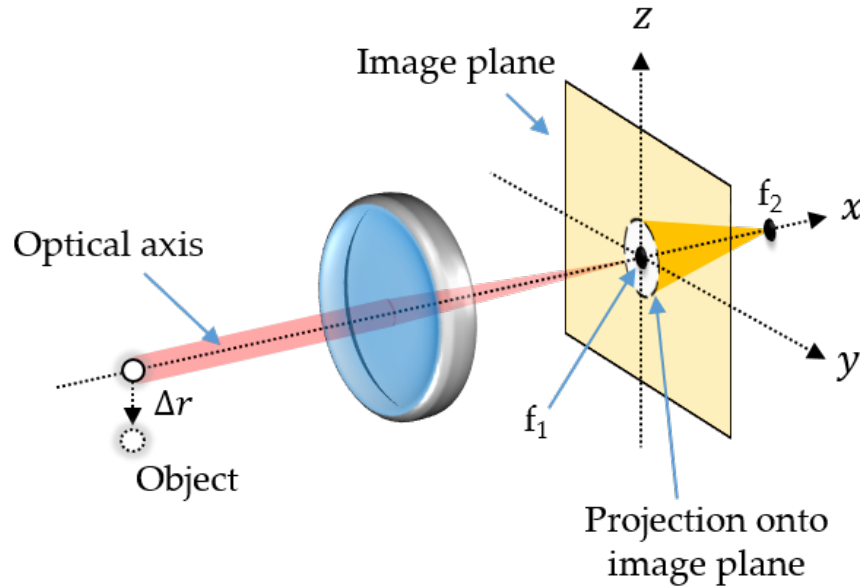

FIGURE 3.26: Schematic of a simplified imaging system to visualise alignment procedure and aberrations.

Spherical aberrations come from the spherical curvature of the lens surface, ideally the lens should be aspheric however this is tricky to manufacture and spherical lenses are more common. The consequence is that rays passing through the lens off centre will be focused to an axial location offset from the rays passing through the centre. At the focus, the intensity distribution is given by the Airy pattern (which is discussed in Section 3.3.2 p.62). The effect of this aberration is to transfer intensity from the central lobe to the side lobes. It can be avoided by using aspheric lenses (which are more expensive) or corrected for by using multiple spherical lenses. In our set-up spherical lens are used due to cost and accessibility.

Coma occurs when the object is located off axis. Rays pass through the lens obliquely, rays that that pass through the edge of the lens are focused at larger distances than rays that pass through the centre. This causes a point like object to look like a comet in the image plane, and its tail will extend towards the edge of the image. The effect is worse for larger aperture lenses. This is problematic when varying time of flight as the cloud moves along the z-axis, to image correctly at each time of flight the imaging system should be recentred to the cloud position. From a measurement of the focus position with time of flight we found that the focus position shifted by $\sim 100 \, \mu m$ from $10 \, ms$ to $25 \, ms$. In our set-up we estimate that this shift corresponds to a decrease in imaging resolution of $1 \, \mu m$ to $2 \, \mu m$. The data acquired in Chapter 4 is taken at a fixed time of flight, and the imaging system and cloud are always centered on each other, thus this effect should be negligible.

Astigmatism is similar to coma in that it occurs when the object is placed off centre from the optical axis, however it can also occur when there is an asymmetry in the lens curvature. Two planes are defined, the meridional plane which contains the object and the optical axis, and the sagittal plane which lies perpendicular. The two planes have separate foci, and the best imaging plane is located between to two.

Curvature of field, also known as the Petzval-aberration, refers to the fact that the imaging plane is in-fact not a plane but has a concave shape when viewed from the object. The curvature of the imaging plane is determined by the refractive index and surface curvature of the lens used. As detectors are typically flat this means that the captured image will be out of focus at the edge. This can be problematic when imaging large clouds.

Distortion occurs when magnification properties of the lens vary across the surface. This can lead to pincushion or barrel deformation depending on whether the magnification is higher or lower closer to the optical axis.

An interesting experiment at the University of Chicago [150] demonstrated a technique to greatly reduce the effects of aberrations. They were able to measure the modulation transfer function (MTF) in-situ from images of thermal clouds (the MTF will be described in relation to the point spread function in the next section). Aberrations distort the MTF, they were able to adjust the alignment of their imaging system and remove the distortions by observing the changes to the MTF.

Finite resolution

To describe the effects of finite resolution it is useful to introduce the point spread function (PSF). The function determines how a point like object $\mathcal{O}(r)$ is transformed into an image $\mathcal{I}(r)$ via the convolution $\mathcal{I}(r) = \mathcal{O}(r) * \text{PSF}(r)$. In a diffraction-limited system the PSF is the Fraunhofer diffraction pattern from a circular aperture and the result is the Airy function. In this case the PSF can be expressed in terms of the resolution,

$$\text{PSF}(r) = 2\frac{J_1\left(1.22\pi r/\Delta r\right)}{1.22\pi r/\Delta r} \tag{3.19}$$

where J_1 is the first order Bessel function of the first kind, and Δr is the resolution as defined by the Rayleigh criterion in Eq. (3.17). As a convolution in real space is equivalent to a multiplication in Fourier space, the image $\mathcal{I}(r)$ can be calculated by,

$$\mathcal{I}(r) = \text{FT}^{-1}[\tilde{\mathcal{O}}(k) \cdot \text{OTF}(k)], \tag{3.20}$$

here, $\tilde{\mathcal{O}}(k)$ is the Fourier transform of the object $\mathcal{O}(r)$, and the optical transfer function (OTF) has been introduced which is the Fourier transform of the PSF. The OTF is a complex function, its modulus is responsible for amplitude variation and is known as the modulation transfer function (MTF), the argument causes phase variation and is known as the phase transfer function (PTF), thus the total expression

$\text{OTF}(q) = \text{MTF}(q)\exp[i\text{PTF}(q)]$. For a diffraction-limited system there is no phase shift and the OTF can be reduced to MTF. For this reason the OTF and MTF are commonly interchanged. In real systems (not diffraction limited) the PSF is more complicated than Eq. (3.19) and is related to the pupil function which accounts for aberrations, for further reading see [150, 151]. Though, for systems with small aberrations Eq. (3.19) is a good estimate.
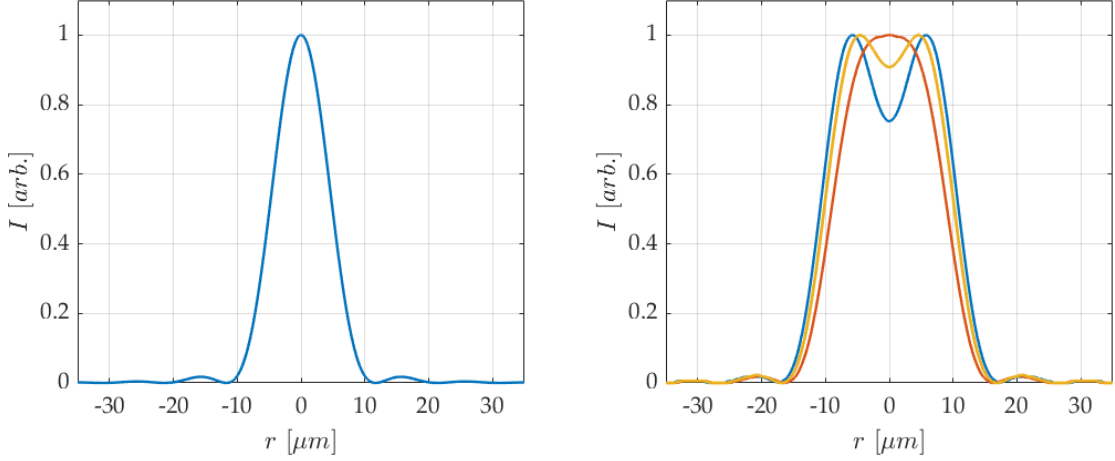

FIGURE 3.27: (Left) Normalised intensity of the modulus squared of point-spread function for an imaging resolution of $r_{\text{Rayleigh}} = 11.7\,\mu\text{m}$. (Right) Example image of two points separated by $11.7\,\mu\text{m}$ the Rayleigh criterion (blue), $9\,\mu\text{m}$ the Sparrow criterion (red), and $10.35\,\mu\text{m}$ a distance in between (yellow).

Figure 3.27 shows a one dimensional cut through $|\text{PSF}|^2$ where the PSF is given by Eq. (3.19), and the resulting image for two point like objects with different separations. It is worth noting that whilst the Rayleigh criterion is the most commonly accepted definition of imaging resolution, in practice it is still possible to discern that there are two points when separated at this distance. The most generous definition is given by the Sparrow criterion $\Delta r_{\text{Sparrow}} = \frac{0.47\lambda}{\text{NA}}$, at this distance there is no minimum between the two points in the final image. This criterion is perhaps more important for our experimental analysis as density fringes separated by $\Delta r_{\text{Rayleigh}}$ will still be discernible, and hence appear in the power spectrum, $\langle|\rho(q)|^2\rangle$ see Section 2.3.3 for the definition of $\langle|\rho(q)|^2\rangle$.
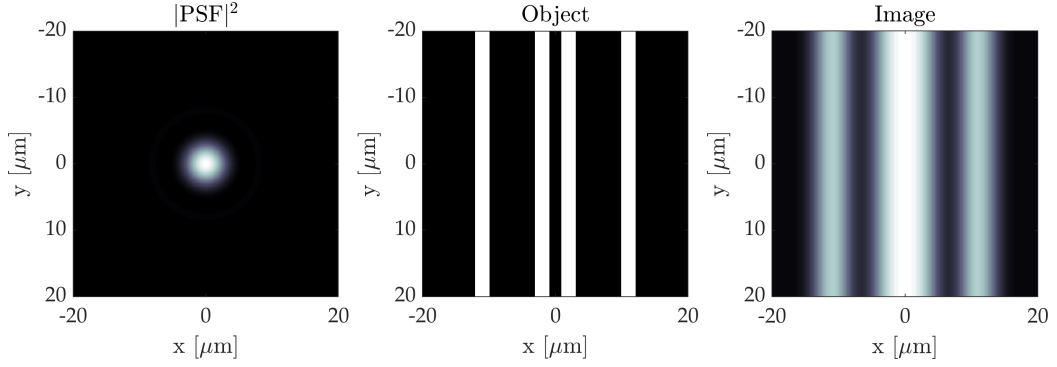
FIGURE 3.28: (Left) Modulus square of the point spread function generated using Eq. (3.19), with $\Delta r = 6\,\mu\text{m}$. (Center) Object, consisting of four $2\,\mu\text{m}$ thick stripes, the outer pair are separated by a distance of $20\,\mu\text{m}$, the inner pair by $2\,\mu\text{m}$, and separation between the outer and inner stripes equal to $7\,\mu\text{m}$. (Right) Resulting image after convolution of the object with the PSF.

An example of imaging an object with a finite resolution is shown in Fig. 3.28. In this figure the object consists of four stripes at different separations, imaging the object equates to a convolution of the object with the PSF. The result is to blur out the initial stripe pattern. In this case the blurring is so large that the two inner stripes can no longer be resolved. This stripe pattern is much like density ripples that arise from the phase fluctuations discussed in Section 2.3.3 and we observe experimentally. If two fringes in the atomic density are too close together they will be blurred into one, just like is seen in Fig. 3.28.

It is possible to approximate the PSF by fitting a Gaussian to the central lobe. Using the Gaussian approximation the effect of the imaging system on $\langle |\rho(q)|^2 \rangle$ can be simulated by multiplying by $e^{-q^2 \sigma_{\text{PSF}}^2}$ [96], where σ_{PSF} is the width of the Gaussian, the result can been seen in Fig. 3.29. The change is dramatic, high frequencies are suppressed and only the first peak remains yet with reduced amplitude and frequency. We can get an in-situ measurement σ_{PSF} by fitting the power spectrum of a 1D cloud to $\langle |\rho(q)|^2 \rangle e^{-q^2 \sigma^2}$ (where $\langle |\rho(q)|^2 \rangle$ is defined in Eq. (2.67)) gives a value of $\sigma_{\text{PSF}} = 4\,\mu\text{m}$, this corresponds to a resolution of $\Delta r_{\text{Rayleigh}} = 11.7\,\mu\text{m}$.
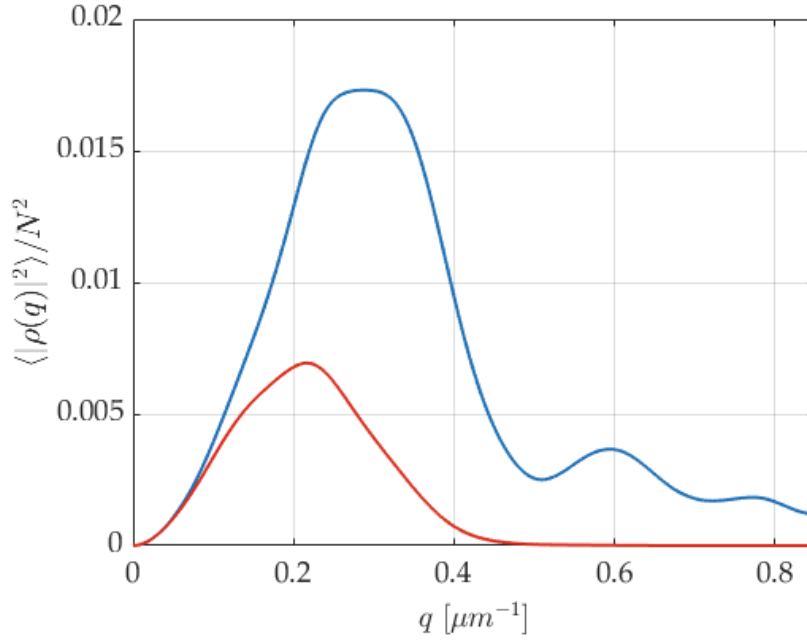
FIGURE 3.29: (Blue) Density ripple power spectrum simulated with the Ornstein-Uhlenbeck method (see Section 4.1.4). (Red) result after convolution with the PSF which has been approximated to a Gaussian with $\sigma_{\mathrm{PSF}} = 4\,\mu\mathrm{m}$.

Prior to installment the resolution of the high-magnification imaging system was measured externally by imaging a pin-hole of $2\,\mu\mathrm{m}$ diameter. When imaging an object much smaller than the imaging resolution the object is effectively point-like and the resulting image captures the modulus square of the point spread function $|\mathrm{PSF}|^2$. Figure 3.30 shows the results of our measurement, where a $2\,\mu\mathrm{m}$ diameter pin-hole was imaged at different points along the optical axis. As the pin-hole moves through the focus the point spread function alters, which can be seen in the captured images Fig. 3.30a. The images are compared to a ray-tracing simulation performed with OSLO which predicts the focal point as the position where the power in the central lobe is greatest. The pin-hole measurement shows good agreement with the OSLO simulation, and σ_{PSF} matches to within $10\,\%$, this corresponds to a resolution as defined by the Rayleigh criterion of $\Delta r_{\mathrm{Rayleigh}} = 5.4\,\mu\mathrm{m}$ from OSLO, and $\Delta r_{\mathrm{Rayleigh}} = 5.8\,\mu\mathrm{m}$ obtained from the pin-hole measurement. It is not completely clear why there is such a large discrepancy with the resolution measured externally and in-situ. However, we believe that the source of the discrepancy comes from a few differences between the external and in-situ set-up, for example a different camera was used in the external measurement (it had a smaller pixel size and therefore was deemed less likely to impair the measurement) and it is plausible that during installation the optical alignment was not as good as in the external set-up. It is also possible that in-situ the exit beam is clipped by the view-port, this would reduce the NA and thus increase $\Delta r_{\mathrm{Rayleigh}}$.
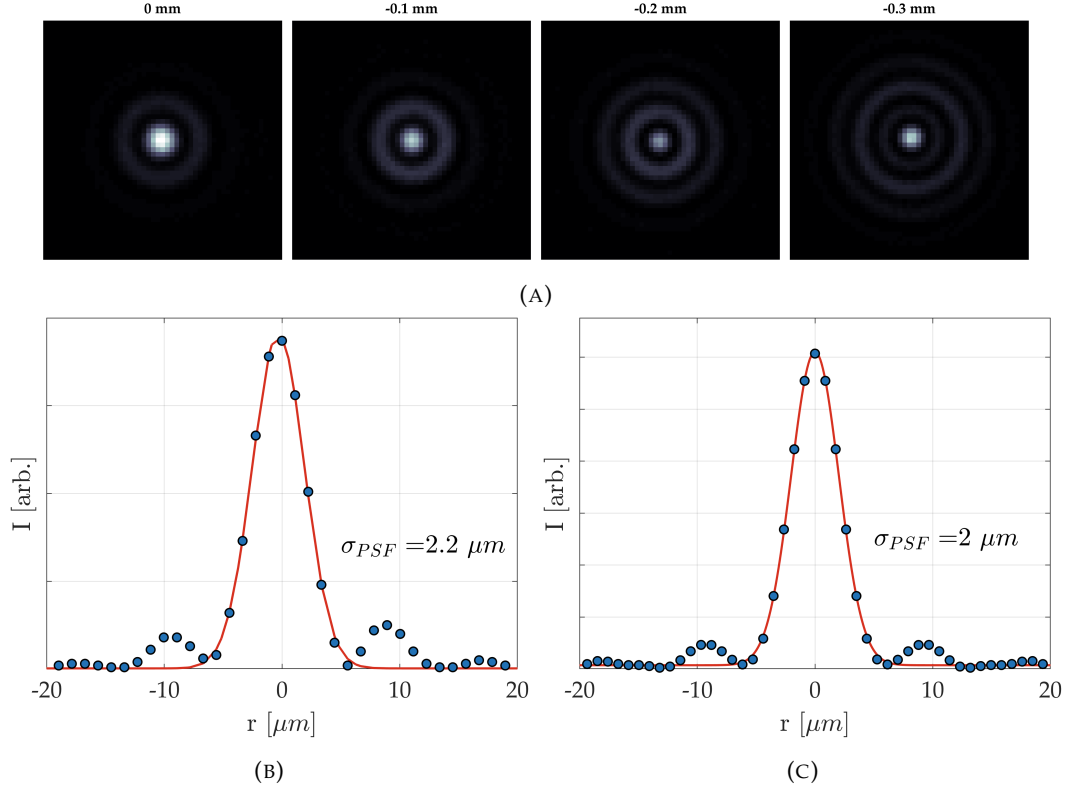
(A)

(B)

(C)

FIGURE 3.30: (A) Intensity images of $2\,\mu$m diameter pin-hole at various distances from the focal plane. As the pin-hole is defocused the intensity in the outer discs increases. (B) (Blue dots) Horizontal cut through an image of the pin-hole in focus, the central lobe is then fitted to a Gaussian (red curve). (C) Simulation produced in OSLO of the point spread function (blue dots) for our imaging at the focal point, the central lobe is fitted to a Gaussian (red curve).

Finite pixel area

After passing through the optics the image still needs to detected. Typical cameras have a square array of equally spaced photosensitive pixels, the result is to average over each pixel area, and due to the pixel separation certain frequencies will be suppressed. This averaging effect can be expressed as a convolution of the image with a 2D rectangular function, we write the detector response function $h_{\text{detector}}(x, y)$ as,

$$h_{\text{detector}}(x, y) = \text{rect}(x/W_x)\text{rect}(y/W_y), \tag{3.21}$$

where W_i is the width of a pixel. What matters here is the pixel width at the atoms (the object plane), this is the physical width of the camera pixel divided by the magnification. To calculate the corresponding MTF we then take Fourier transform, and hence the MTF for an array of square pixels is given by,

$$\text{MTF}_{\text{detector}}(k_x, k_y) = |\text{sinc}(\pi k_x W_x)||\text{sinc}(\pi k_y W_y)|, \tag{3.22}$$

where $k_x = 1/x$ and $k_y = 1/y$.

(A)

(B)

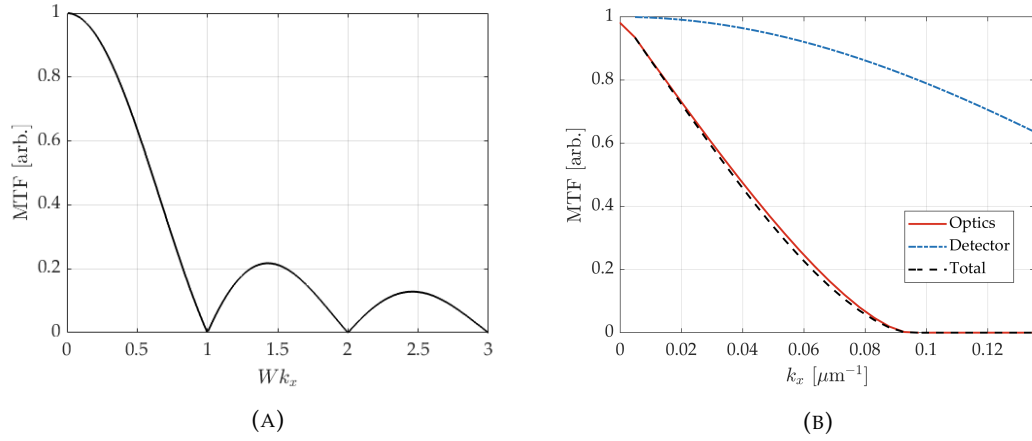FIGURE 3.31: (A) 1D MTF of a square pixel array with am effective pixel width of W, at spatial frequencies of $k_x = n/W$, where $n \in \{1, 2, 3...\}$, there is a complete reduction in amplitude. The effective pixel width is determined by the camera pixel width W_{cam} divided by the magnification M. (B) (Blue, dash-dot) MTF of our detector which for the high-magnification imaging system has an effective pixel width $W = W_{\mathrm{cam}}/M = 13/3.51 = 3.7\,\mu\mathrm{m}$. (Red, solid) MTF of our imaging optics given by Eq. (3.19), which has $\sigma_{\mathrm{PSF}} = 4\,\mu\mathrm{m}$. (Black, dashed) combined MTF of the whole imaging system. Units are given in $2\pi/\mu\mathrm{m}$ to be consistent with spectral measurements in the experimental section.

Figure 3.31 shows the effect of our camera on the MTF, the additional contribution is minimal. For high resolution imaging systems however it can become very important, for the MTF to not be detector limited the pixel size must be made sufficiently small.

3.3.3 Focusing methods

As previously discussed (Section 3.3.2) placing the imaging system at the focal plane is vital, even a relatively small separation between them ($>100\,\mu\mathrm{m}$) can cause a large decrease in the imaging resolution. In order to find the focal point experimentally, one must minimise a parameter whilst translating the imaging system along the imaging axis. One commonly used method measures the Thomas-Fermi radius of a BEC, which is deemed suitable due to the relatively (compared to a thermal cloud) sharp change in optical density at the cloud edge. A measurement using this method in our experiment is shown in Fig. 3.32. It is quite obvious that this is not a particularly sensitive measurement. Our pixel size is $3.75\,\mu\mathrm{m}$ so the cloud radius increases by roughly 2 pixels $2\,\mathrm{mm}$ away from the focus it is worth noting that this measurement should be improved with a smaller pixel.
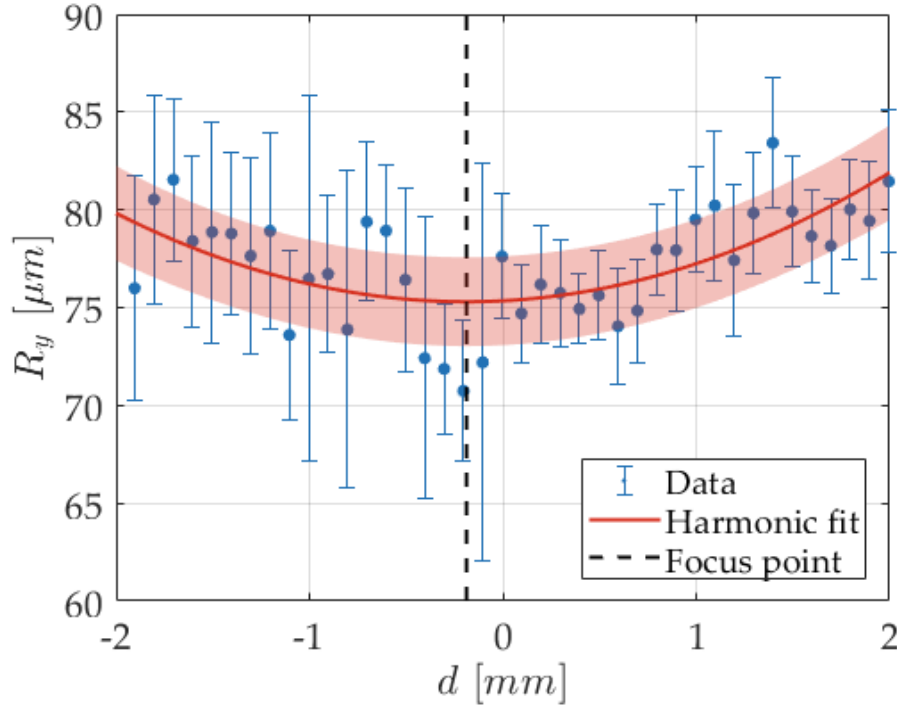
FIGURE 3.32: Focusing of the imaging system using axial half size of the cloud. (Blue, dots) Mean TF radius measured from five clouds at each distance d, errorbars indicate the standard deviation. (Red, solid) A harmonic fit finds the minimum at $d = (-188 \pm 112)\,\mu m$, the red shaded region indicates the confidence bounds from the fit, where $d = 0\,\mu m$ is the focal position determined from the density ripple method.

Density ripples can occur on scales much smaller than typical imaging resolutions, and when analysed in reciprocal space (i.e. the spatial frequency spectrum) the observed spectrum is very sensitive to small changes in the imaging resolution, making density ripples an ideal tool to determine the focal point, and has been demonstrated to be accurate to within $2\,\mu m$ [152]. As the imaging system moves away from the focal plane not only is there a blurring of the fringes, there are also additional artificial fringes that appear. The effect on the power spectrum $\langle |\rho(q, d)|^2 \rangle$ is to shift the first peak to lower frequencies and generate artificial peaks at higher spatial frequencies. The form of this relation is given by,

$$\langle |\rho(q, d)|^2 \rangle = \langle |\rho(q, 0)|^2 \rangle \cos^2 \left(\frac{q^2 d}{2k_0} \right), \tag{3.23}$$

where d is the distance from the focal plane, and k_0 is wave number of the imaging beam. An example of this measurement is shown in Fig. 3.33, which shows clearly the appearance of the artificial fringes as the imaging system is moved out-of-focus.
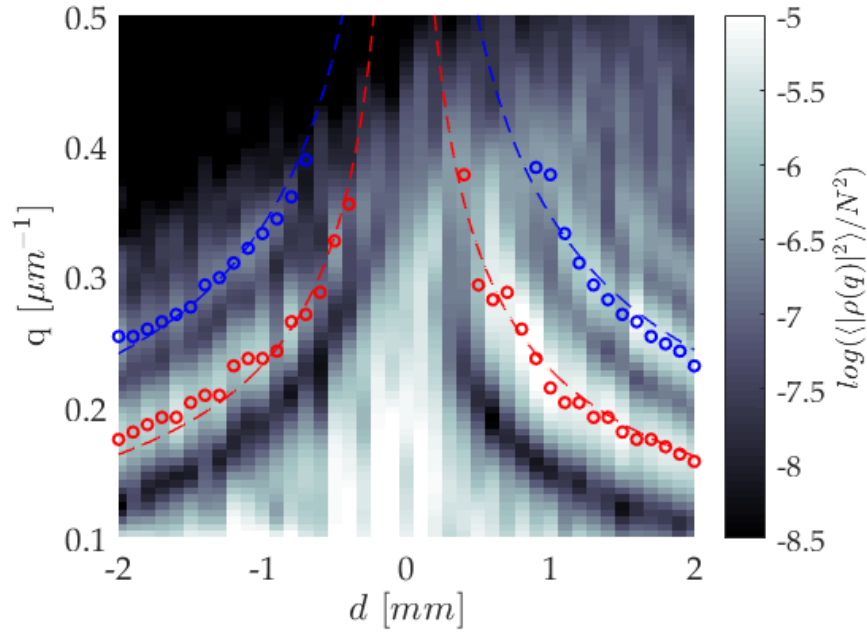
FIGURE 3.33: Focusing of the imaging system using density ripples. At each distance the mean power spectrum of the density ripples $\langle|\tilde{\rho}(q)|^2\rangle$ Eq. (4.8), is calculated from $\sim$ 30 images. Red and blue curves are fits to second and third peaks using Eq. (3.23), the focus is found at $d = (0 \pm 20)\,\mu m$.
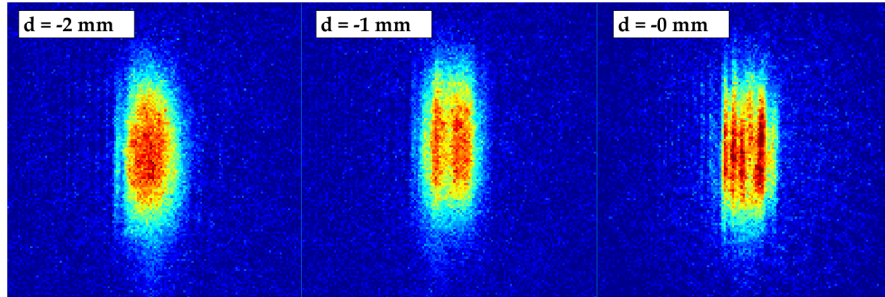

FIGURE 3.34: Single shot OD images of clouds taken at with the camera located at different points along the optical axis, where $d = 0\,mm$ is at the focus.

Cloud tilt

The trapping potential created in a H or Z trap causes a tilt, θ, with respect to the central trapping wire due to the vertical field asymmetry that arise between the legs and the central wires (see Section 2.1.1). Adjusting the trapping frequencies to decrease the aspect ratio $\lambda = \omega_\perp/\omega_\parallel$ causes an increase in the cloud tilt θ. Consider the diagram in figure 3.35, the imaging process effectively integrates the density along the x-axis, capturing any density fluctuations that occur along the y-axis. However, if $\theta \neq 0$ the integration does not occur along the eigenaxis of the cloud and would start to blur out the density ripples.
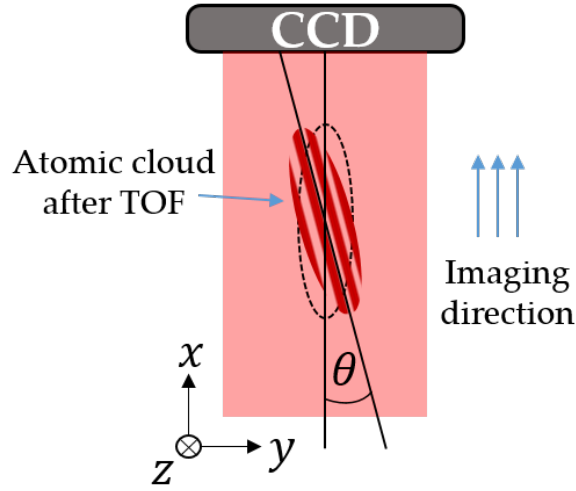
FIGURE 3.35: Schematic showing the orientation of the cloud tilt, θ, with respect to the imaging direction. During time of flight the cloud changes from a cigar shape to an elliptical disc, due to strong interactions in the radial direction. If the cloud is phase fluctuating density ripples will appear parallel to the semi-major axis.

When we initially started acquiring data for this experiment we didn't account for the cloud tilt and saw an artificial reduction in the density ripples in the lower aspect ratio traps. To model effects of the cloud tilt we first simulated the propagation of an electric field through an atomic density by using a split-step Fourier method [152]. The theoretical steps are described in Section 3.3.4, however in this section only a qualitative description is used and results shown.

We start by simulating a 3D atomic density of a BEC in the Thomas-Fermi approximation that has been expanded after a time of flight. The density is then modulated by a sinusoid with a variable spatial period d, to simulate density ripples with a specific, well-defined frequency, the cloud is then tilted about the z-axis by an angle θ determined from a magnetic trapping field simulation of the PCB and atom chip, plus an additional tilt ϕ that accounts for any tilt of imaging beam from the optical axis Fig. 3.36a shows a plot of a density slice in the x-y plane. The electric field of the imaging beam is then propagated through the tilted cloud (along the x-axis) and the optical density is calculated as shown in Section 3.3.4, replicating the optical density images captured experimentally (see Fig. 3.36b). Residuals are calculated by subtracting the density modulated image from one without the modulation, the residuals are then integrated along the z-axis to obtain the line density (see Fig. 3.36c). We then compare the power spectrum of tilted and non-tilted residuals, and repeat for a number of different spatial periods d. The tilted power spectra are normalised by the non-tilted spectra and the relative difference is computed to estimate the modulation versus spatial frequency q, thus creating a MTF$_\theta$ for cloud tilt seen in Fig. 3.37a. To simulate the effect of cloud tilt we then multiply the power spectrum $\langle|\rho(q)|^2\rangle$ by MTF$_\theta$. Figure 3.37b shows the result we see that the cloud tilt acts similar to the PSF in
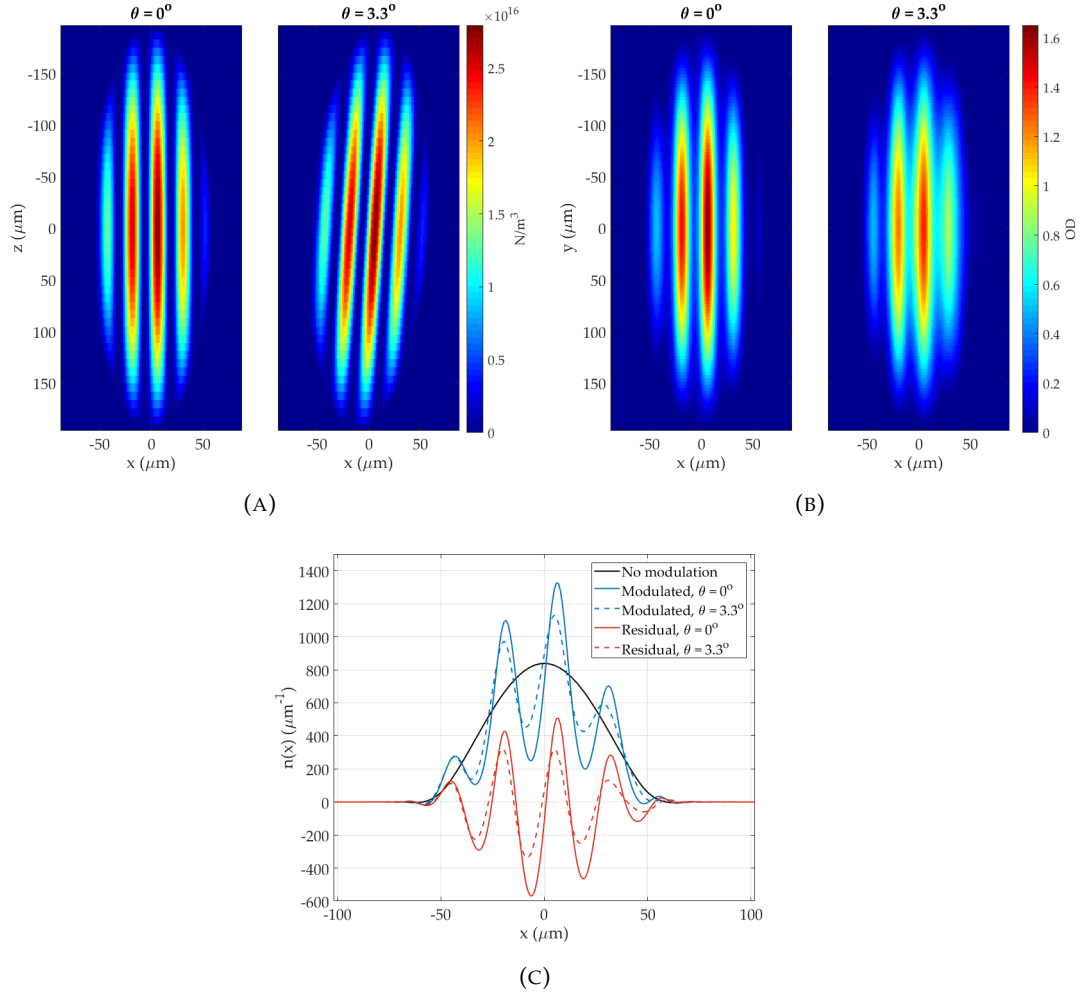
(A)

(B)

(C)

FIGURE 3.36: (A) density slice through the plane parallel to surface without tilt (left) and with tilt (right). (B) Simulated optical density images of the tilted clouds. (C) line density of tilted images and the calculated residuals for tilted and non-tilted clouds.

Fig. 3.29 it has a much stronger suppression of high frequencies. The modulation grows with the radial size of the cloud and θ, thus traps with larger atom number and/or $\omega_\perp$ will be more sensitive to θ.

For the traps we initially investigated θ ranged from 1° to 6.5°, and the value of the laser beam tilt ϕ was unknown. To estimate ϕ we deliberately tilt the imaging beam to maximise $\langle |\rho(q)|^2 \rangle$, this would mean that the laser beam is aligned with the cloud tilt, i.e. $\theta + \phi = 0°$. We found that such condition is met when $\phi = 1.5°$. Once we knew our value of ϕ we then adjusted the imaging beam tilt such that $\theta + \phi = 0° \pm 0.5°$ for all traps. However, it is not good practice to apply large corrections to ϕ as it can deteriorate the MTF of the optics (misalignment off the optical axis can increase aberrations and reduce the resolution), we therefore ensure $\phi \leq 2.5°$, and hence all traps investigated in Chapter 4 have θ no greater than 3°.
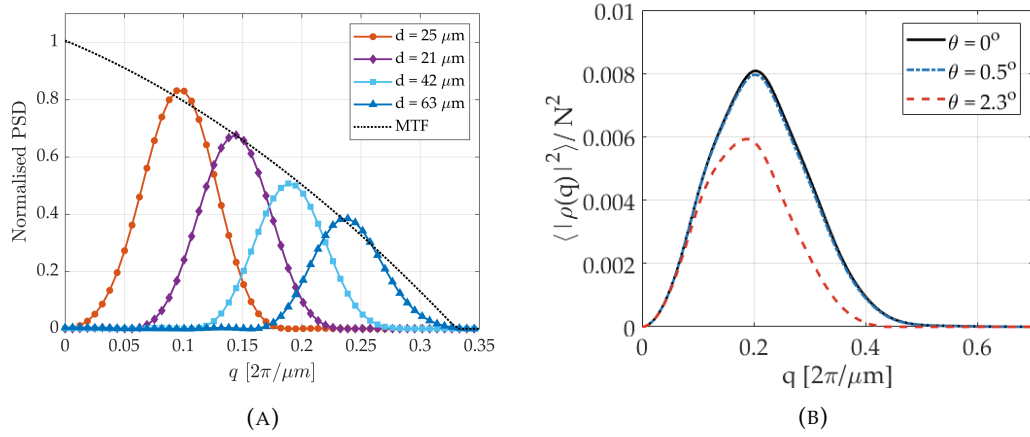
FIGURE 3.37: (A) MTF_θ is calculated from the ratio of the normalised amplitude of $\langle \rho \rangle$ for $\theta \neq 0°$ and $\theta = 0°$ at a number of different density modulation periods d. (B) Application of MTF_θ on $\langle \rho \rangle$, simulated by the Ornstein-Uhlenbeck process (see Section 4.1.4). We see that $0.5°$ tilt has negligible effect and therefore we consider it an acceptable error.

3.3.4 Split-step Fourier method

This section describes the method we have used to simulate the effect of the cloud tilt on the power spectrum of the density ripples. It can also be used to generate a theoretical prediction of the measurement in Fig. 3.33, the technique follows the approach used in [152]. The method propagates the electric field $\vec{E}(\vec{r})$ along the optical axis (the x direction), with wave number $k_0 = 2\pi/\lambda$, $\vec{E}(\vec{r})$ is defined as,

$$\nabla^2 \vec{E}(\vec{r}) + k_0^2 \varepsilon(\vec{r}) = -\nabla[\vec{E}(\vec{r}) \cdot \ln(\varepsilon(\vec{r}))]. \tag{3.24}$$

For a propagation through an object with complex relative permittivity $\varepsilon(\vec{r}) = \epsilon/\epsilon_0$ and relative susceptibility $\chi(\vec{r}) = \varepsilon(\vec{r}) - 1$, where ϵ is the permittivity, and ϵ_0 is the vacuum permittivity. If $\varepsilon(\vec{r})$ varies slowly across the medium the RHS of Eq. (3.24) can be set to zero, leaving,

$$\nabla^2 \vec{E}(\vec{r}) + k_0^2 \varepsilon(\vec{r}) = 0. \tag{3.25}$$

Assuming light is linearly polarised along x such that $\vec{E}(\vec{r}) = E(\vec{r})\vec{e_x}$, we can rewrite Eq. (3.24) as,

$$-\frac{\delta^2 E(\vec{r})}{\delta x^2} = [\nabla_{y,z}^2 + k_0^2]E(\vec{r}) + k_0^2 \chi(\vec{r})E(\vec{r}). \tag{3.26}$$

Applying the paraxial wave approximation and assuming the electric field has the form $E(\vec{r}) = \exp(ik_0 x)E'(\vec{r})$, where $E'(\vec{r})$ is a slowly varying envelope along $\vec{e_x}$, inserting into Eq. (3.26) we get,

$$-2ik_0 \frac{\delta E(\vec{r})}{\delta x} = \nabla_{y,z}^2 E'(\vec{r}) + k_0^2 \chi(\vec{r})E'(\vec{r}). \tag{3.27}$$

where the weak dependence of $E'(\vec{r})$ on x allows us to drop the $\frac{\delta^2 E'(\vec{r})}{\delta x^2}$ term. Propagation of $E'(\vec{r})$ can be split into two operations, one that performs free space propagation with operator $\mathbf{P}'(\vec{r}_{2D}, \Delta x)$ ($\chi(\vec{r}) = 0$), and another that deals with the absorption and refraction of the light $\mathbf{Q}'(\vec{r}_{2D}, \Delta x)$ (this only considers the second term of the right-hand-side in Eq. (3.26)). In the simulation free space propagation is performed in Fourier space, the operators are given by,

$$\mathbf{P}'(\vec{r}_{2D}, \Delta x) = \tilde{\mathbf{P}}'(\vec{k}_{2D}, \Delta x) = \exp\left(-i \frac{k_{2D}^2}{2k_0} \Delta x\right), \tag{3.28}$$

$$\mathbf{Q}'(\vec{r}_{2D}, \Delta x) = \exp\left(i \frac{k_0}{2} \int_x^{x+\Delta x} \chi(\vec{r}) dx, \right) \tag{3.29}$$

under the condition that $|\chi(\vec{r})| \ll 1$ such that the dependence of $E'(\vec{r})$ on x remains weak. The total propagation can then calculated by a split-step method,

$$E'(\vec{r} + \Delta x) = \mathbf{P}'(\Delta x/2)\mathbf{Q}'(\Delta x)\mathbf{P}'(\Delta x/2)E'(\vec{r}). \tag{3.30}$$

Once the electrical field is known the intensity can be calculated via $I(\vec{r}) = c\epsilon_0 |E(\vec{r})|^2/2$, from which the optical and atomic densities can be extracted using Eq. (3.4).

3.4 Preparation and characterisation of condensates

This section explains the experimental sequence used to produced a condensate in terms of timings and processes. A lot of the steps are common to all ultracold atom experiments however the optimal parameters can vary a lot depending on environmental conditions. I will describe our specific sequence parameters and why we have chosen them, the main limitations and how to resolve/improve on them.

3.4.1 Experimental sequence

Our typical sequence takes around $14\,\mathrm{s}$ to produce a single condensate. In the experiment we can produce condensates with different atom number, temperature, and trapping frequencies. Each run shares the same sequence up until the atoms are loaded into the chip trap. The ideal sequence is as short as possible without sacrificing too much on the final atom number, or shot to shot stability.
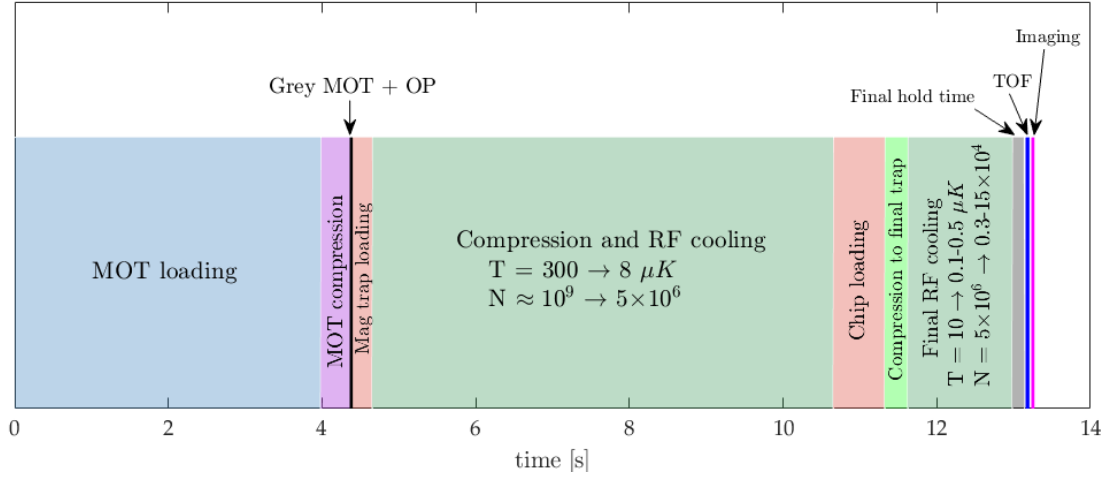
FIGURE 3.38: Time series of the processes used to generate a condensate. Each cloud generated undergoes the same process up until the chip has bean loaded, from there the trapping currents are varied to get the desired trap frequencies, then the hold time and final RF frequency are manipulated to control atom number and temperature.

MOT loading: Approximately 2×10^9 pre-cooled atoms from the 2D MOT are loaded into the 3D MOT in $4\,\mathrm{s}$ at a height of $4\,\mathrm{mm}$ from the chip surface.

MOT compression: The MOT is compressed by increasing the trapping frequencies and brought to a height of $1.5\,\mathrm{mm}$ from the surface of the atom chip, we then apply sub-Doppler cooling for $7\,\mathrm{ms}$ reducing the temperature of the atoms to approximately $60\,\mathrm{\mu K}$. The trapping fields are then turned off and the atoms are then optically pumped to the $|F = 2, m_f = 2\rangle$ ground state in $2.5\,\mathrm{ms}$.

Magnetic trap loading: Magnetic trapping fields are turned on within a few ms capturing approximately 1×10^9 atoms and held for a further $50\,\mathrm{ms}$ and the cloud is heated to about $300\,\mathrm{\mu K}$ during the process.

Compression and rf cooling: Radio frequency cooling is applied whilst the cloud is compressed and brought to a height of $300\,\mathrm{\mu m}$ from the chip whilst maintaining a trap bottom of roughly $1\,\mathrm{G}$ (this corresponds to $0.7\,\mathrm{MHz}$). The cloud is cooled to approximately $8\,\mathrm{\mu K}$ with 5×10^6 atoms remaining. As the initial chip trap is not as deep as the copper-Z trap hotter clouds would start spill out of the trap.

Chip loading: The rf frequency is raised instantaneously to $20\,\mathrm{MHz}$ and the atom chip and PCB currents are ramped on and the copper-Z down in $600\,\mathrm{ms}$. Approximately 4×10^6 atoms are loaded into the chip trap with minimal heating.

Compression to final trap: The cloud is then moved to a height of $100\,\mathrm{\mu m}$ while being compressed to the desired final trap frequencies. This is the closest we can get to the

chip surface before observing adverse fragmentation.

Final rf cooling: Once the atoms are settled in the final trap, we apply the last RF cooling ramp to set the final temperature of the atoms. It is during this ramp that we reach the critical temperature and make a BEC, the formation of a condensate as the temperature is reduced can be seen in Fig. 3.39. The cloud is then held for an additional $150\,\mathrm{ms}$ in the presence of an RF-shield to ensure the cloud has thermalised, a further optional hold time is applied to control the final atom number. The high heating rate from the current noise means the maximum hold time is less than $1\,\mathrm{s}$.
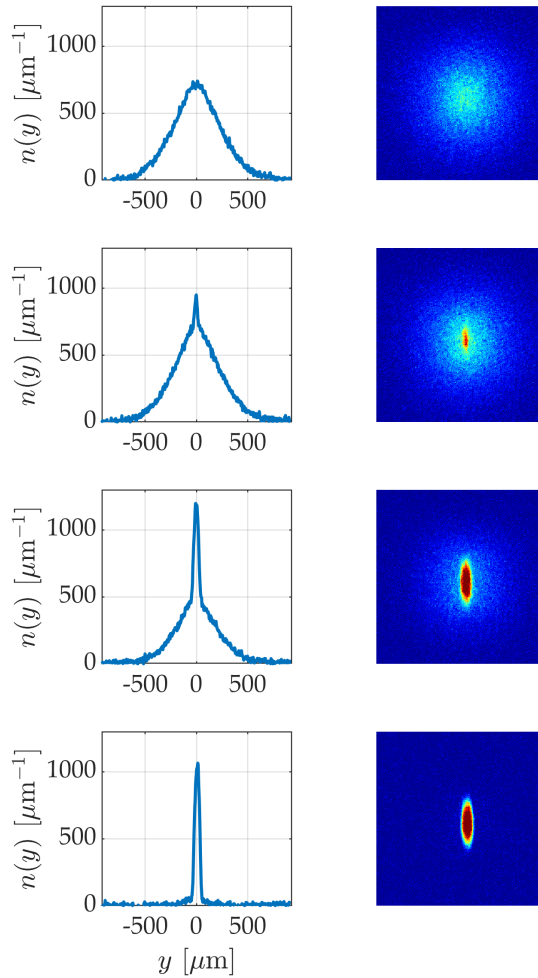

FIGURE 3.39: Formation of a BEC as the final rf frequency is reduced and the temperature of the gas decreases. From top to bottom, cloud temperature $T = 641\,\mathrm{nK}$, $547\,\mathrm{nK}$, $466\,\mathrm{nK}$ and $165\,\mathrm{nK}$, and condensate fraction $N_0/N_{\mathrm{tot}} = 0\,\%$, $2\,\%$, $14\,\%$ and $81\,\%$. The trapping frequencies are $\omega_\perp = 2\pi \times 680\,\mathrm{Hz}$ and $\omega_\parallel = 2\pi \times 23.5\,\mathrm{Hz}$.

The specific values for currents, timings, frequencies and powers etc. were chosen to optimise the phase space density. One way to analyse the effectiveness of the sequence is to plot the cooling efficiency i.e. the ratio of the number of atoms lost per

gain temperature reduction. Figure 3.40 shows the efficiency curves for three different sequences (shallow gradient corresponds to better cooling) the blue curve shows the progress made when we initially started to optimise the sequence. The cooling efficiency starts well but as we get to colder temperatures there are not enough atoms to maintain a high collision rate and the phase space density fails to reach unity i.e. condensation does not occur. To increase atom number we then doubled the MOT loading time, and with careful optimising of the rf cooling ramp we were able to improve the cooling efficiency in the latter stages of the sequence such that the cloud could condense. The yellow curve in Fig. 3.40 depicts the efficiency of the sequence in Fig. 3.38, with the addition of the 2D MOT the atom number and ramp time was improved throughout the sequence.
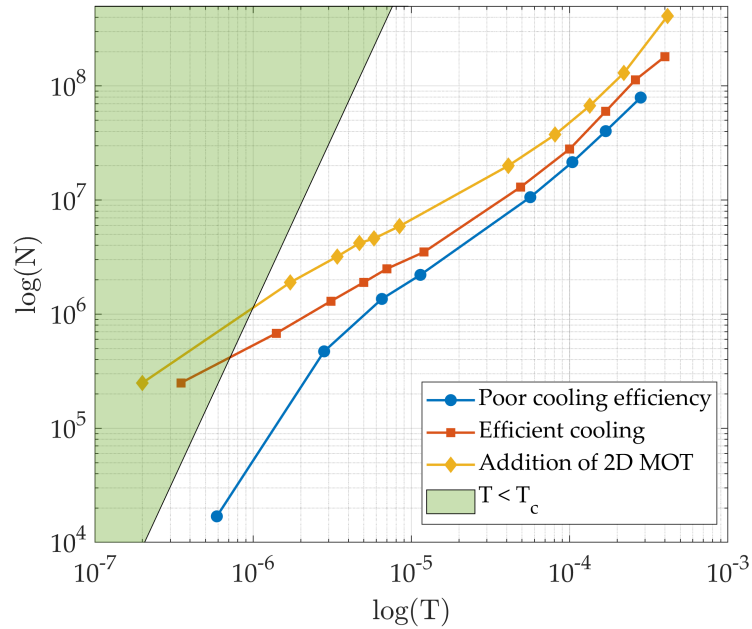

FIGURE 3.40: (Blue) No pre-cooling with the 2D MOT, $15\,\mathrm{s}$ MOT loading from the background, $10\,\mathrm{s}$ evaporative cooling, poor cooling efficiency during the end of the sweep prevented condensation. (Red) No 2D MOT, $30\,\mathrm{s}$ MOT loading, $10\,\mathrm{s}$ evaporative cooling, a higher initial atom number kept cooling efficiency high enough to reach condensation. (Yellow) 2D MOT, $4\,\mathrm{s}$ MOT loading, $7.5\,\mathrm{s}$ evaporative cooling. The green shaded area depicts the critical temperature required for condensation in a trap with a geometric mean frequency of $\bar{\omega} = 2\pi \times 212\,\mathrm{Hz}$.

The main limitations in our laboratory are, the absence of adequate air conditioning, a poor vacuum pressure, and electrical noise. The lack of active temperature control severely affects the long term stability of our experiment, the output of many components (e.g. electrical currents and optical fibre coupling) is dependent on the temperature of the laboratory (it typically takes an hour or two for our experiment to reach a stable temperature). This in turn is affected by external

temperatures and we see the lab temperature drift from morning to evening, day to day (if there are sharp changes in the weather), and from winter to summer. The sequence therefore requires constant tweaking in order to maintain atom number and most importantly the final trapping frequencies. An obvious improvement would be to install better AC units, and this has been scheduled to take place in the coming year. We are also planning to implement active feedback on the electric currents supplied to the trapping structures, this should keep the final trap frequencies fixed, and thus improve shot to shot stability and reduce the warm up time.

Bad vacuum pressure increases the collision rate between trapped cold atoms and the hot atoms from the background, thus reducing the lifetime of atoms in magnetic trap. These are "bad collisions" (see Section 2.1.2). The bad collision rate effectively determines the speed of the RF cooling sweep. The reasons for the poor vacuum pressure are discussed in Section 3.1.2, the vacuum limited lifetime is shown in Fig. 3.7, hence our sequence time in on the order of $10\,\mathrm{s}$. Increasing the lifetime would allow us to perform the cooling sweep slower making the cooling more efficient, however since the high pressure appears to be down to the sub-D connectors on the electrical feed-through connected to our vacuum chamber, it would require replacement of the electrical feed-through. Though we did apply high vacuum sealant around the sub-D pins which reduced the pressure from $5 \times 10^{-10}\,\mathrm{mbar}$ to $1.5 \times 10^{-10}\,\mathrm{mbar}$.

Whereas a thermal cloud's lifetime is largely vacuum limited, the condensate lifetime is much shorter, typically below $500\,\mathrm{ms}$, as it is subject to extra loss mechanisms. Atom losses occur from collisions with untrapped background atoms, three-body collisions (proportional to n^2), two-body spin flips (proportional to n), and parametric heating that comes from technical noise on the trapping fields. Heated atoms accelerate losses as they can undergo multiple collisions with the condensed atoms. To prevent the accelerated losses from heating, a radio-frequency (rf) shield is used to remove the heated atoms from the trap [153]. The frequency of the rf shield has to be slightly adjusted for different traps, we find $8\,\mathrm{kHz}$ to $12\,\mathrm{kHz}$ greater than the final frequency of the rf cooling sweep to be optimal.
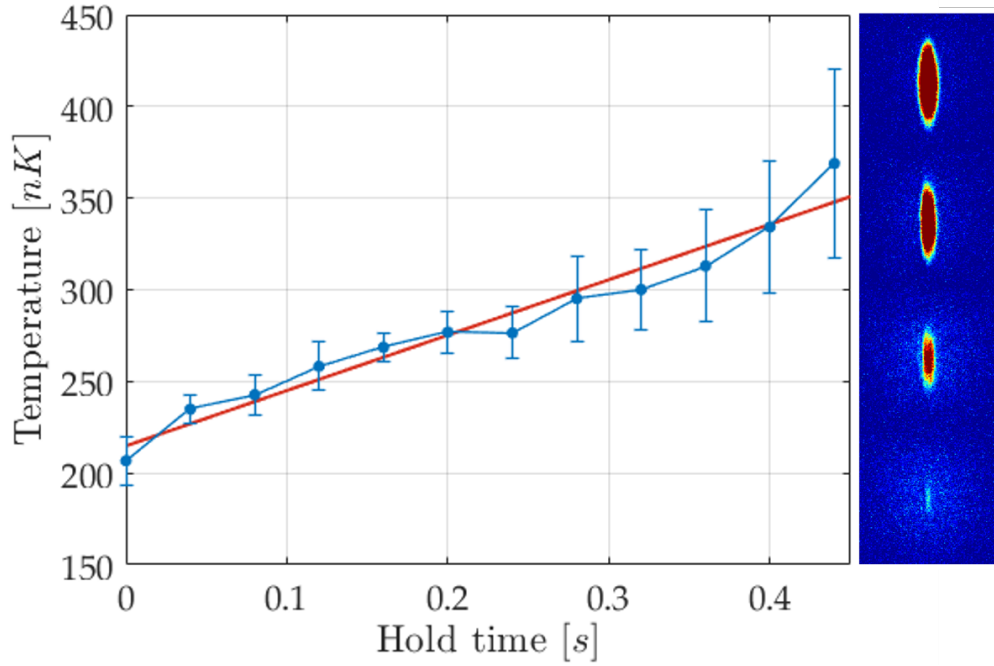
FIGURE 3.41: (Left) Temperature versus hold time in the atom chip trap. A BEC is created and allowed to thermalise in the presence of an RF-shield, the shield is then switched off and held for a further time to allow the current noise and background collisions to heat the cloud. From a linear fit the heating rate is measured to be $(302 \pm 22)\,\text{nK/s}$. (Right) Optical density images of clouds at hold times of (from top to bottom) $0\,\text{ms}$, $120\,\text{ms}$, $280\,\text{ms}$ and $440\,\text{ms}$.

The most problematic electrical noise in our lab came in the form of electrical current noise in the trapping structures, and ground loops. Current noise refers to the small AC current that is superimposed onto the DC output and depends on the specifications of the power supply unit. It causes a shaking of the trapping potential that leads to heating of the atoms if at a frequency comparable to $\omega_\perp$, $\omega_\parallel$, or the trap bottom, a measurement of the heating rate is given in Fig. 3.41, often the only way to reduce this is to buy a higher quality power supply or implement active stabilisation [154]. Noisy input power can also affect the noise of the device output, we have low noise power sockets in the laboratory which we power important devices such as the laser diodes and PSUs for trapping structures. Initially we powered our control system directly from the mains, this was later found be a large noise source and switching to an external PSU dramatically increased the cloud lifetime. Ground loops occur when the grounds for different devices become connected, this can lead to current flow in undesirable paths. We have observed ground loops to cause components output to become noisy, and even radiate in the radio-frequency $1\,\text{MHz}$ to $20\,\text{MHz}$ range (this is bad as it can couple the m_f states and cause additional spin-flip losses). Ground loops are notoriously complicated to resolve and since in typical cold atom experiments there are numerous connections between multiple devices it is

important to take great care to avoid short-circuits between different grounds. To protect against stray radio-frequency radiation we use cable shielding on the connections to the trapping structures.

Final cloud parameters

The range of traps used in the experiment in Chapter 4 are listed in the table below. The values were chosen to investigate the 1D and 3D regimes. For the 1D regimes we wanted to explore any difference between the usual 1D conditions, $\mu/\hbar\omega_\perp <1$, and $k_B T/\hbar\omega_\perp <1$ with the less stringent definitions such as high aspect ratio and $L/\lambda_T \gg 1$. For the 3D regime we need $L/\lambda_T \ll 1$, in general this requires large atom number, and low temperatures. Atom number and temperatures are obtained by the fitting procedure discussed in Section 3.3.1, and the trap frequencies are determined by the measurement shown in Fig. 3.42.

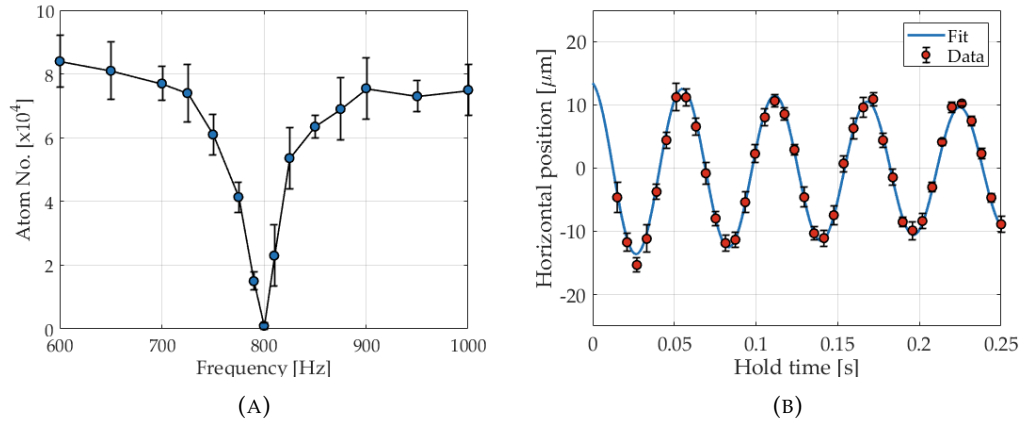| Trap parameter	Value
$\omega_\parallel$ [$2\pi \times$ Hz]	15 - 34
$\omega_\perp$ [$2\pi \times$ Hz]	400 - 1400
λ	12 - 80
N [10^4]	0.3 - 12
T [nK]	80 - 500

TABLE 3.2: Cloud parameters

FIGURE 3.42: (A) Example of a measurement of the radial trapping frequency $\omega_\perp$, an AC current is applied to PCB track 2C, the frequency is then swept. The AC current causes parametric heating of the cloud, and when in the presence of an RF shield heated atoms are kicked out of the trap, the effect is strongest on resonance hence the trap frequency is the point where most of the atoms are lost. In this measurement $\omega_\perp = 2\pi \times (800 \pm 10)$ Hz. (B) Example measurement of the longitudinal trapping frequency $\omega_\parallel$, a small horizontal kick is applied to the cloud, the cloud is held in the trap and undergoes an oscillation at the trap frequency. The hold time is varied and the horizontal position extracted, the data is then fitted to a damped sinusoidal function. In this measurement $\omega_\parallel = 2\pi \times (17.70 \pm 0.16)$ Hz.

Chapter 4

Density Ripples in the crossover Regime

This chapter explains our main experiment; measurement of the density ripples across the 3D-1D crossover in order to probe the evolution of the phase coherence, and determine the driving parameters. The first section describes four contending theoretical models that can be used to predict the power spectrum of the density ripples after time of flight $\langle |\rho(q)|^2 \rangle$ in elongated phase-fluctuating gases. Second the experimental acquisition and data analysis methods are explained. Finally the results are shown and discussed, this part contains a comparison of our measurements against the different theoretical models and an investigation into the potential driving parameters of the 3D-1D crossover regime.

4.1 Equilibrium properties: simulation

In this section four theoretical models are described, each concerned with the density ripples after time of flight but differing in their assumptions and approach. The basis of each model is explained and their results will be compared to each other, comparison with our measured data is made in the following section.

4.1.1 Imambekov result

In 2009, an analytical expression was presented for the spectrum of the density ripples after time of flight for a weakly interacting 1D gas of length $L \rightarrow \infty$ in the thermodynamic limit i.e. $n_{1D} = N/L$ is constant [93]. The model assumes that at time $t = 0$ the confinement potential is switched off instantaneously, during time of flight interactions are assumed to be negligible and redundant, and axial expansion is weak such that mean density profile after time of flight is equal to the in-situ density profile i.e. $\langle \rho(y, t_{\text{tof}}) \rangle = n(y, t = 0) = n_{1D}$ where $n(y)$ denotes the in-situ density profile, and $\rho(y)$ the density after time of flight. The main result was first given in Section 2.3.3,

however for readability I will repeat it here[1],

$$\frac{\langle |\tilde{\rho}(q)|^2 \rangle}{n_{1D}^2 \xi} = \frac{\lambda_T q - \left[\lambda_T q \cos(2\hbar q^2 t_{\text{tof}}/m) + 2 \sin(2\hbar q^2 t_{\text{tof}}/m) \right] \exp(-2\hbar q t_{\text{tof}}/m\lambda_T)}{q\xi(1 + \lambda_T^2 q^2)}.$$

(4.1)

This result is valid if

$$\frac{\pi}{\xi} \sqrt{\frac{\hbar t_{\text{tof}}}{m}} \frac{k_B T}{\mu} \gg 1,$$

(4.2)

and if satisfied, the first order correlation function can be approximated to $g^{(1)}(y) = \exp(-|y|/\lambda_T)$. Note that $\langle |\rho(q)|^2 \rangle$ is an intensive quantity, when comparing Eq. (4.1) to a system of finite length we introduce the parameter $\langle |\tilde{\rho}(q)|^2 \rangle = L\langle |\rho(q)|^2 \rangle$. The spectrum shows non-monotonic behaviour as long as $t_{\text{tof}} < 6.5m\lambda_T^2/\hbar$, the position of the minima and maxima are roughly given by,

$$q_n^{\min} = \sqrt{\frac{\pi m 2n}{\hbar t_{\text{tof}}}},$$

(4.3a)

$$q_n^{\max} = \sqrt{\frac{\pi m(2n-1)}{\hbar t_{\text{tof}}}}.$$

(4.3b)

These are "standing wave" conditions (the arguments of the sine and cosine terms in Eq. (4.1) are equal to πn / $2\pi n$) which become more precise at lower temperatures [93], i.e. the contrast between minima and maxima increases with decreasing temperature. The presence of minima and maxima in $\langle |\rho(q)|^2 \rangle$ is understood by interpreting the free expansion of a phase fluctuating cloud as the matter-wave equivalent to the temporal Talbot effect [155]. Initially formulated in optics from the context of a plane wave incident on a periodic grating. At regular distances from the grating (the Talbot length) the image of the grating is reproduced. The effect has been observed in cold atom experiments numerous times, [156–161].

In Fig. 4.1a the function in Eq. (4.1) is plotted for various times-of-flight, illustrating how the spectrum changes. The first maximum $q_1^{\max}$ shows the worst agreement with Eq. (4.3b) this is due to the interplay between the exponential decay term with the oscillatory sine and cosine terms. The modification of the spectrum due to finite optical imaging resolution is demonstrated in Fig. 4.1b. For comparison, Fig. 4.1c shows an experimental measurement of the power spectrum of the density ripples. This measurement has also been obtained with a 2D degenerate Bose gas [98] for which the analytic prediction was also given in [93]. However, they found the positions of the maxima to be given by $q_n^{\max} \simeq \sqrt{\pi m(1.8n - 1.26)/\hbar t_{\text{tof}}}$ as opposed to Eq. (4.3b), they attribute the discrepancy to interactions during early time-of-flight, which was also theoretically investigated in [162].

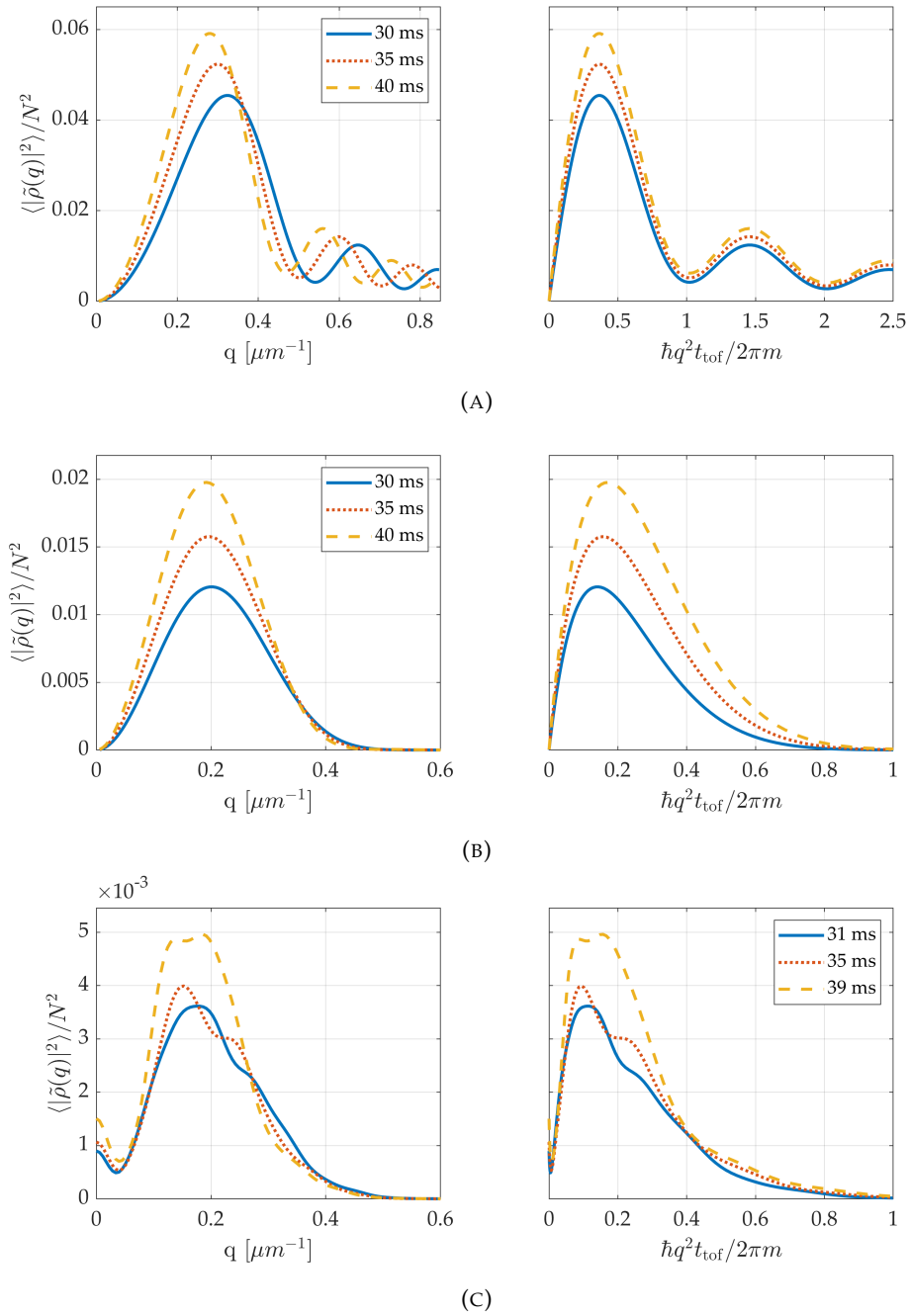[1]Note, the original expression in [93] contained an incorrect factor, which was later corrected in [97].

FIGURE 4.1: (A) (Left) Density ripple power spectra $\langle|\tilde{\rho}(q)|^2\rangle$ generated with Eq. (4.1) for a cloud with $n_{1D} = 24\,\mu\mathrm{m}^{-1}$ and $T = 5\,\mathrm{nK}$ at time-of-flight $30\,\mathrm{ms}$ (blue, solid), $35\,\mathrm{ms}$ (red, dotted), and $40\,\mathrm{ms}$ (yellow, dashed). Minima/maxima of the spectra shift to lower frequencies as time of flight increases. (A) (Right) Minima/maxima of spectra at different time-of-flight align when plotted against the dimensionless quantity $\frac{\hbar q^2 t_{\mathrm{tof}}}{2\pi m}$, positions of the minima/maxima are estimated by Eqs. (4.3a) and (4.3b). (B) Density ripple power spectra generated as in (A) with an additional correction for the finite optical imaging resolution. The shift in peak position becomes less clear, and the peaks fail to align when plotted against $\frac{\hbar q^2 t_{\mathrm{tof}}}{2\pi m}$. (C) Experimentally measured power spectra $\langle|\tilde{\rho}(q)|^2\rangle$ for a cloud in the cross-over regime with $\omega_{(\perp,\parallel)} = 2\pi \times 1075\,\mathrm{Hz}$ and $18.6\,\mathrm{Hz}$, $N = 6.5 \times 10^4$, $T = 350\,\mathrm{nK}$, $L/\lambda_T \sim 5$, and $\mu/\hbar\omega_\perp = 3.5$.

4.1.2 Local density approximation

Imambekov's result Eq. (4.1) was derived for an infinitely long system with uniform density, however this is not a realistic experimental scenario. Obviously $L = \infty$ is impossible, and generally the confining potential means the system's density will be inhomogeneous, even though homogeneous densities are possible with box traps [129, 163–166]. According to [93] corrections for finite length can be neglected if,

$$\frac{mL}{\hbar t}\min\left(L, K\xi/a\right) \gg 1, \tag{4.4}$$

where $K = \pi\hbar n_{1\mathrm{D}}/mc$ is the Luttinger liquid parameter, and c is the speed of sound, if only the lowest transverse mode is occupied then $c = \sqrt{2\hbar\omega_\perp n_{1\mathrm{D}}a/m}$. This is easily satisfied within our experimental parameters. If Eq. (4.4) holds then the density inhomogeneity can be accounted for using the local-density approximation (LDA) by averaging Eq. (4.1) over many smaller parts of the gas, each with different homogeneous densities. This approach was suggested in [93] but has been used and developed mainly by the Paris group [95, 96, 145, 167]. For systems with $L \gg \lambda_T$ and $\hbar q t_{\mathrm{tof}}/m$, and if we only consider wavevectors greater than the inverse cloud length $q \gg 1/L$, the region of cloud that contributes to the density fluctuations at position y is much smaller than L justifying the use of the LDA [96]. Implementing the LDA calculates Eq. (4.1) with the local density $n_0(y)$ and averages over the length of the gas, this is expressed by [96],

$$\langle|\tilde{\rho}(q)|^2\rangle = \int dy \langle|\rho_{n_0(y)}(q)|^2\rangle. \tag{4.5}$$

They find excellent agreement with the result from a complete calculation based on the Bogoliubov modes [96, 145]. A comparison between the two results is shown in Fig. 4.2, however the choice of density to make a fair comparison with the LDA isn't obvious. For the LDA the density profile $n(y)$ is assumed to be Thomas-Fermi, to compare with the homogeneous we can either use the peak density $n(0)$ or the average density N/L, both results are shown Fig. 4.2 though the correct density is seemingly arbitrary. Though, this highlights the limitation of a comparison between an infinite homogeneous system and a finite inhomogeneous system.
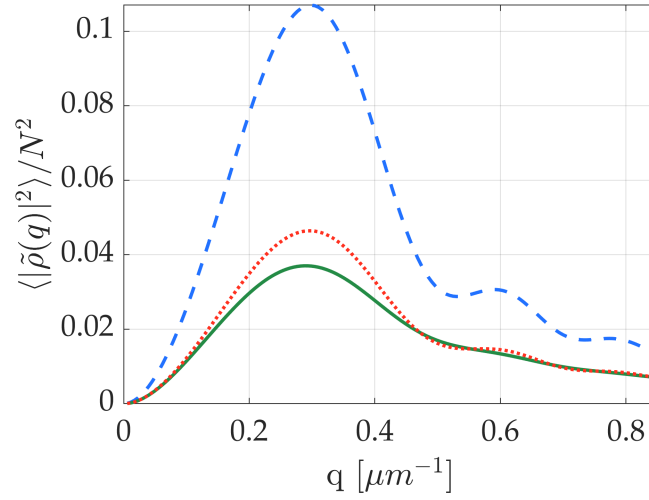
FIGURE 4.2: Density ripple power spectra $\langle|\tilde{\rho}(q)|^2\rangle$ calculated with Eq. (2.67) in the homogeneous case for two densities, (blue, dashed) $n_{1D} = N/L$, and (green, solid) $n_{1D} = n(0)$ the peak density of the longitudinal density profile (assumed to be Thomas-Fermi), finally using the LDA (red, dotted). Cloud parameters are taken from an experimentally measured values of a 1D gas, where $(\omega_\perp, \omega_\parallel) = 2\pi \times 1235\,\mathrm{Hz}$ and $16.1\,\mathrm{Hz}$, $N = 6.7 \times 10^3$, $T = 105\,\mathrm{nK}$, $L/\lambda_T = 9.5$, and $\mu/\hbar\omega_\perp = 0.87$.

Both the homogeneous and LDA results have been used to perform thermometry, a measured power spectrum or $g^{(2)}$ can be fitted with the analytical result (with an imaging correction applied) where T is the only free parameter. The homogeneous result was used in [94], and the LDA in [95, 96, 145, 167]. An example thermometry measurement using the LDA is shown in Fig. 4.3, for a 1D cloud we observe an agreement (albeit weak) with the standard wing fitting procedure (see Section 3.3.1), however in the crossover regime we observe that the LDA underestimates the temperature by a factor of 2-3.
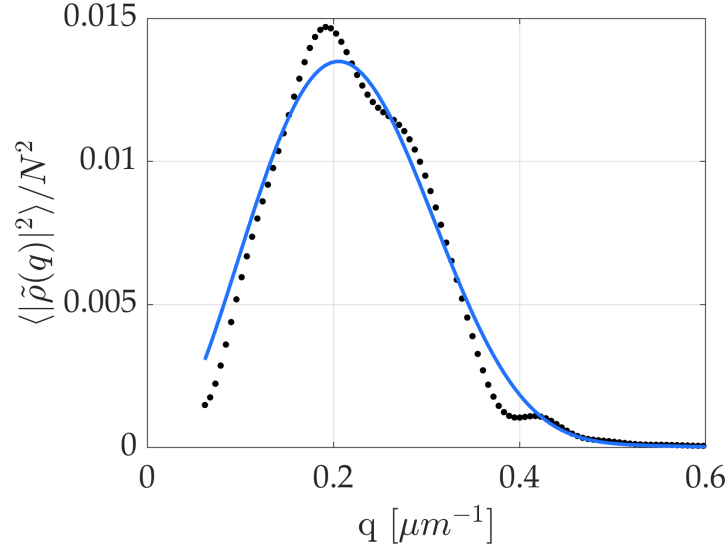
FIGURE 4.3: Temperature measurement using the LDA simulation. Measured density ripple power spectrum (black, dots) of a 1D cloud after $34\,\text{ms}$ time-of-flight fitted with the LDA simulation (blue, solid line). Fitting returns a temperature of $T = (77 \pm 15)\,\text{nK}$, whereas standard wing fitting (see Section 3.3.1) gives $T = (105 \pm 32)\,\text{nK}$, which are consistent within the error (determined from statistical variations). The large error in the temperature T from wing fitting procedure is attributed to the low atom number, as the optical density of the thermal component at low atom numbers and long time of flight is very small and hence the signal to noise is also low. Measured cloud parameters $(\omega_\perp, \omega_\parallel) = 2\pi \times 1235\,\text{Hz}$ and $16.1\,\text{Hz}$, $N = 6.7 \times 10^3$ $\mu/\hbar\omega_\perp = 0.87$, with $\sigma_\text{psf} = 4\,\mu\text{m}$.

4.1.3 Dettmer result

In 2001 an experiment was performed analysing the nature of phase fluctuations in elongated 3D BECs [32, 33]. Acknowledging the fact that interactions will play a role during time-of-flight they presented a model that incorporates it, however it assumes that the phase fluctuations remain small with respect to the overall density profile of the cloud, which should be valid in 3D. The initial assumption of the distribution of phase was taken from [31] which was evaluated for elongated 3D condensates. Fluctuations arise from excitations of two groups: high-energy particle-like excitations $\epsilon_j > \hbar\omega_\perp$ and low energy collective excitations $\epsilon_j < \hbar\omega_\perp$. Here, $\epsilon_j = \hbar\omega_\parallel \sqrt{j(j+3)/4}$ is the excitation spectrum and is calculated by solving the Bogoliubov-de-Gennes equations for the case of an elongated 3D condensate [31, 168]. High-energy excitations have wavelengths smaller than both the radial and longitudinal size of the condensate and therefore have "3D character" and can only provide small phase fluctuations. In contrast, low-energy excitations have wavelengths larger than the radial size but smaller than the longitudinal size and as such have "1D character". The low-energy excitations are expected to be the dominant contribution to the phase fluctuations [31].
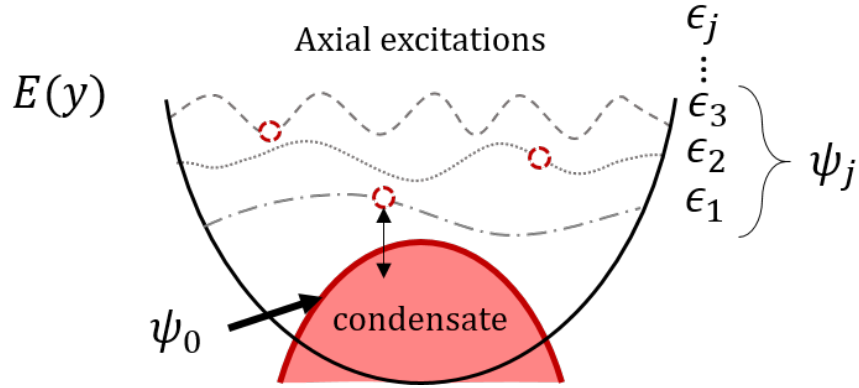
FIGURE 4.4: Visualisation of the axial spectrum of low-energy excitations. The quasi-condensate consists of a highly occupied groundstate ψ_0 and numerous low-energy excitations ψ_j. These excitations are phonons (or quasi-particles) and can be viewed as density oscillations within the atomic cloud [169].

The low-energy axial excitation spectrum is visualised in Fig. 4.4, the occupation is given by $N_j = [\exp(\epsilon_j/k_B T) - 1]^{-1}$ in accordance with Bose-Einstein statistics. The total phase distribution $\theta(y)$ is evaluated by a sum over the phase contributions from each axial mode i.e. $\theta(y) = \sum_{j=1}^{\infty} \theta_j(y)$. Contributions from each mode are weighted by their occupation number N_j, however random thermal fluctuations will drive transitions between different modes. The phase distribution of a single mode j is [32]

$$\theta_j(y) = \left[\frac{(j+2)(2j+3)g}{4\pi R_\perp^2 L \epsilon_j (j+1)} \right]^{1/2} P_j^{(1,1)} \left(\frac{y}{L} \right) \frac{(\alpha_j + \alpha_j^*)}{2}, \tag{4.6}$$

where $P_j^{(1,1)} \left(\frac{y}{L} \right)$ are Jacobi polynomials, α_j and α_j^* are complex Gaussian random variables that have replaced the creation and annihilation operators, as is typical in a c-field approximation. The random variables α_j and α_j^* capture changes in the occupation of each mode that arise from thermal fluctuations. Examples of phase distributions calculated according to Eq. (4.6) are shown in Fig. 4.5 for various temperatures, in both 1D and 3D configurations. It can be seen that the 3D configuration gives rise to more axially phase-coherent clouds.
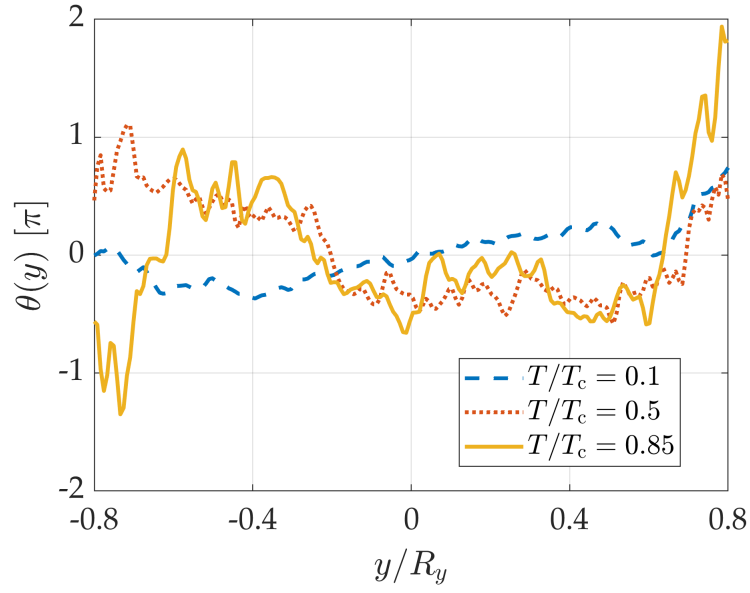
(A)
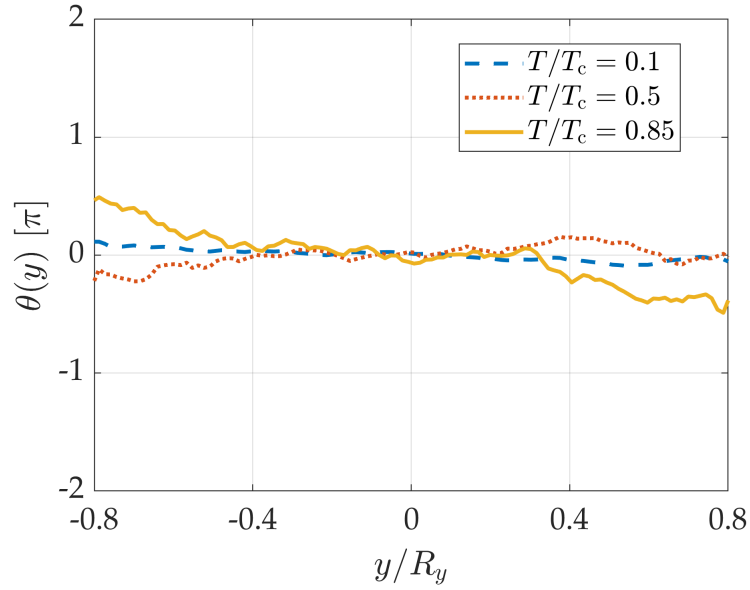
(B)

FIGURE 4.5: Numerically simulated phase distributions produced by Eq. (4.6) at different reduced temperatures T/T_c. (A) 1D cloud with $(\omega_\perp, \omega_\parallel) = 2\pi \times 1235\,\text{Hz}$ and $16.1\,\text{Hz}$, $N = 6.7 \times 10^3$, $\mu/\hbar\omega_\perp = 0.87$, and $L/\lambda_T = 1.35$, 6.75 and 11.5 respectively. (B) 3D cloud with $(\omega_\perp, \omega_\parallel) = 2\pi \times 395\,\text{Hz}$ and $33.7\,\text{Hz}$, $N = 9.6 \times 10^4$, $\mu/\hbar\omega_\perp = 8.37$, and $L/\lambda_T = 0.05$, 0.25 and 0.42 respectively.

By linearising the 3D Gross–Pitaevskii equation with respect to small fluctuations of the phase and density, and imprinting the phase $\theta(y)$ on the in-trap wavefunction, they arrive at the following analytical expression for the relative density fluctuations

after time of flight,

$$\frac{\delta n(y)}{n_0(y)} = 2 \sum_j \sin \left[\frac{\epsilon_j^2 t_{\text{tof}}}{\hbar\mu(1 - (y/L)^2)} \right] (\omega_\perp t_{\text{tof}})^{-(\epsilon_j/\hbar\omega_\perp)^2} \theta_j(y), \tag{4.7}$$

and demonstrated that this expression reproduces the result obtained from a full 3D numerical solution of the GPE for a given time-of-flight. Using this equation we can generate density ripples after time-of-flight and measure the power spectrum through,

$$\langle |\tilde{\rho}(q)|^2 \rangle = \langle | \int dy \delta\rho(y) e^{-iqy}|^2 \rangle. \tag{4.8}$$

Here $\delta\rho(y) = \rho(y) - \langle\rho(y)\rangle$ are the density perturbations from the mean. An example is shown in Fig. 4.6, where it has been plotted with the analytical result for a homogeneous density as well as the local density approximation. Since Eq. (4.7) provides a spectrum of a single cloud we have to take the mean of many realisations, the random nature of the fluctuations means that spectra can look slightly deformed for a low number of realisations (see Fig. A.3).
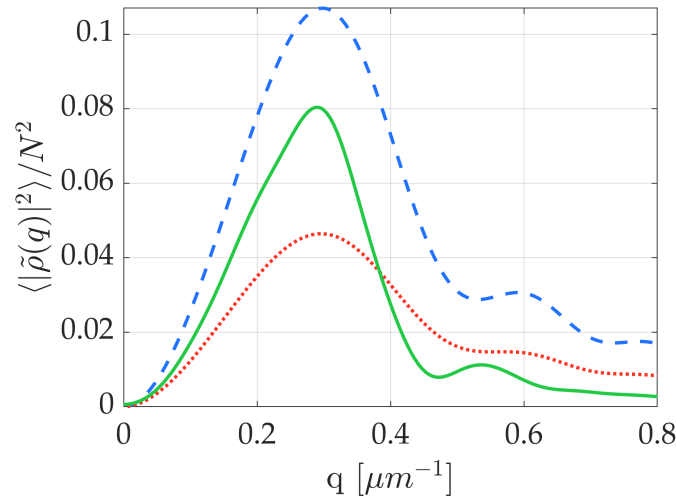

FIGURE 4.6: Density ripple power spectra for the homogeneous case with $n_{1D} = n(0)$ (blue, dashed) calculated with Eq. (2.67), the numerically simulated LDA (red, dotted), and Dettmers result from Eq. (4.7) (green, solid) a mean from 200 realisations. Cloud parameters $(\omega_\perp, \omega_\parallel) = 2\pi \times 1235\,\text{Hz}$ and $16.1\,\text{Hz}$, $N = 6.7 \times 10^3$ $\mu/\hbar\omega_\perp = 0.87$, with $\sigma_{\text{psf}} = 4\,\mu\text{m}$.

In the experiment [32, 33], the expression for the ripples after time-of-flight Eq. (4.7) is used to further obtain a closed-form expression for the mean square density fluctuations in the central region of the cloud σ_{BEC}/n_0,

$$(\sigma_{\text{BEC}}/n_0)^2 = \frac{T}{\lambda T_\phi} \sqrt{\frac{\ln\tau}{\pi}} \left(\left[1 + \left[1 + \left(\frac{\hbar\omega_\perp\tau}{\mu\ln\tau} \right)^2 \right]^{1/2} \right]^{1/2} - \sqrt{2} \right). \tag{4.9}$$

Here, $\tau = \omega_\perp t_{\text{tof}}$, $\lambda = \omega_\perp/\omega_\parallel$, and T_ϕ is a characteristic temperature given by,

$$T_\phi = \frac{15}{32} \frac{(\hbar\omega_\parallel)^2 N_{\text{tot}}}{\mu k_{\text{B}}}. \tag{4.10}$$

In the temperature interval $T_\phi < T < T_c$ the phase will fluctuate at a length scale smaller than the length of the cloud, it is an equivalent parameter to the phase coherence length i.e. $L/\lambda_T \approx T/T_\phi$ [31]. They measure σ_{BEC}/n_0 smaller than the prediction of Eq. (4.9) by a factor of approximately two, and attribute this discrepancy to a small tilt in the imaging beam. A similar measurement with our data is shown in Fig. 4.7b, instead here we have compared the experimental data to the numerical simulation. The quantity σ_{BEC}/n_0 is the relative standard deviation of density fluctuations, in Eq. (4.9) this quantity is evaluated at the cloud centre. To extract this quantity from our measured data and the numerical simulations we have taken the mean standard deviation over a half-width about the cloud centre. The numerical simulation and the analytical result of Eq. (4.9) assume that the phase fluctuations remain small, thus, we have noted the amplitude of the power spectrum $\langle|\tilde{\rho}(q_1^{\text{max}})|^2\rangle$ in the color scale. From Fig. 4.5a we observe that even the numerical simulations are inconsistent with Eq. (4.9), and for the most part the discrepancy is larger when $\langle|\tilde{\rho}(q_1^{\text{max}})|^2\rangle$ is large. A comparison of the numerical simulation with experimental measurements is shown in Fig. 4.7b. From a linear fit to the data we observe that the experimentally measured values of σ_{BEC}/n_0 are approximately 60% of those generated by the numerical simulation. This is not far from the factor of two disparity observed in [32], however in our case we have accounted the tilt of the imaging beam Section 3.3.3. Therefore, this may indicate that the assumption of small phase fluctuations is invalid.
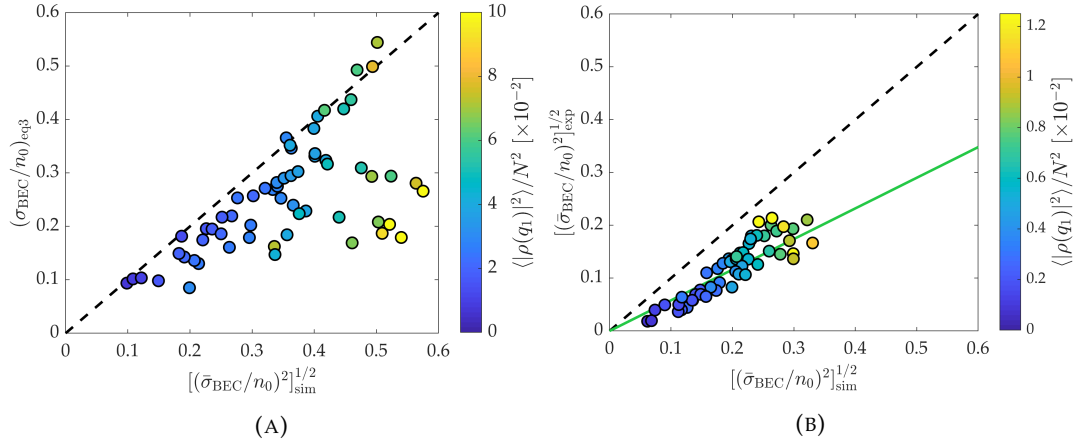
FIGURE 4.7: (A) Relative standard deviation of the density fluctuations $\sigma_{\mathrm{BEC}}/n_0$ calculated from the analytical result in Eq. (4.9) compared to the numerical simulation. The dashed line is guide to the eye at a gradient of one indicating agreement between the numerical simulation and Eq. (4.9). The colourbar indicates the amplitude of the power spectrum $\langle|\tilde{\rho}(q_1^{\mathrm{max}})|^2\rangle$ generated by the numerical simulation. (B) Comparison of $\sigma_{\mathrm{BEC}}/n_0$ measured experimentally and the numerical simulation. In this plot the effect of the imaging has been taken into account. The black-dashed line is a guide to the eye with a gradient of one, and the green-solid line is fit to the data and has a gradient of ~ 0.6. The colourbar indicates the amplitude of the power spectrum $\langle|\tilde{\rho}(q_1^{\mathrm{max}})|^2\rangle$ measured experimentally.

The publication [96] calculates a correction to the LDA to account for the interactions based on Dettmer's result [32, 33], and amounts to multiplying the power spectrum by a frequency-dependent function

$$\mathcal{C}_{\mathrm{int}} = (\omega_\perp t_{\mathrm{tof}})^{-(cq/\omega_\perp)^2}. \tag{4.11}$$

In their experiment $\mathcal{C}_{\mathrm{int}}$ was always >0.95, meaning they could neglect interactions. For our experimental parameter space this correction factor can be significant, in particular for the clouds closer to the 3D regime, due to the dependency of $\mathcal{C}_{\mathrm{int}}$ on $\omega_\perp$, see Eq. (4.11). Considering wavevectors from DC to $q = 2\pi \times 0.4\,\mu\mathrm{m}^{-1}$, $\mathcal{C}_{\mathrm{int}}$ can be as low as 0.4.
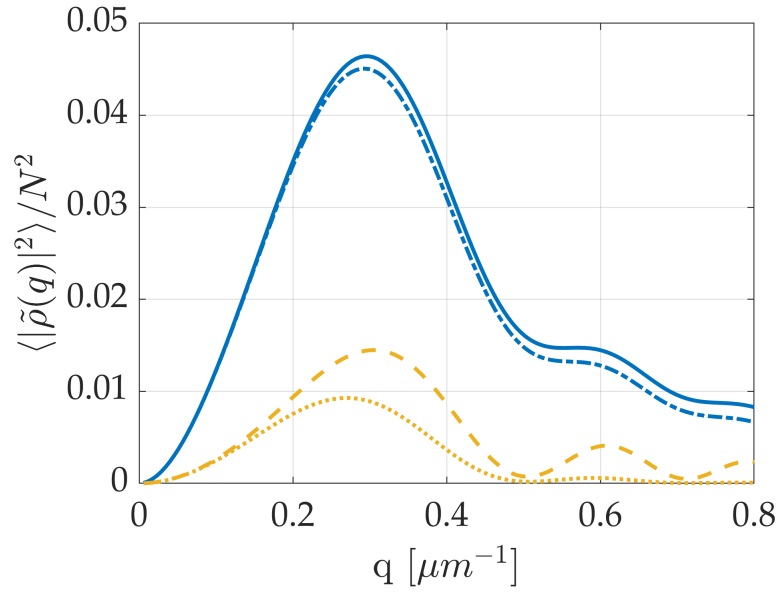
FIGURE 4.8: Effect of interactions during time-of-flight on the power spectra generated from the LDA simulation (see Eq. (4.5)) according to the correction factor $\mathcal{C}_{\text{int}}$ from Eq. (4.11). (Blue, dash-dotted) 1D cloud interaction-corrected, (blue, solid) 1D cloud no interaction correction, (yellow, dotted) 3D cloud interaction-corrected, and (yellow, dashed) 3D cloud no interaction correction. 1D cloud parameters $(\omega_\perp, \omega_\parallel) = 2\pi\times$ 1235 Hz and 16.1 Hz, $N = 6.7 \times 10^3$, $\mu/\hbar\omega_\perp = 0.87$, and $L/\lambda_T = 9.5$. 3D cloud parameters $(\omega_\perp, \omega_\parallel) = 2\pi\times$ 395 Hz and 33.7 Hz, $N = 9.6 \times 10^4$, $\mu/\hbar\omega_\perp = 8.37$, and $L/\lambda_T = 0.33$.

4.1.4 Ornstein-Uhlenbeck process

This numerical approach was developed by the experimental group in Vienna [94, 170–174] and has been used as a thermometry tool in many of their recent publications. The method relies on generating the phase pattern by an Ornstein-Uhlenbeck stochastic process [170, 175]. The original application of the Ornstein-Uhlenbeck (OU) process was in modelling Brownian motion [176]. The main result is that the phase pattern can be generated by,

$$\theta(y + dy) = \theta(y) + \sqrt{\frac{2dy}{\lambda_T(y)}}\mathcal{N}(0, 1), \tag{4.12}$$

where $\mathcal{N}(0, 1)$ is a random number of Gaussian distribution and a standard deviation of 1. The updating formula is useful as it allows us to alter λ_T to match the local density $n(y)$. The generated phase patterns are displayed in Fig. 4.9. Figure 4.10 shows that the phase pattern generated via Eq. (4.12) results in the same spatial correlation properties as in Eq. (4.6).
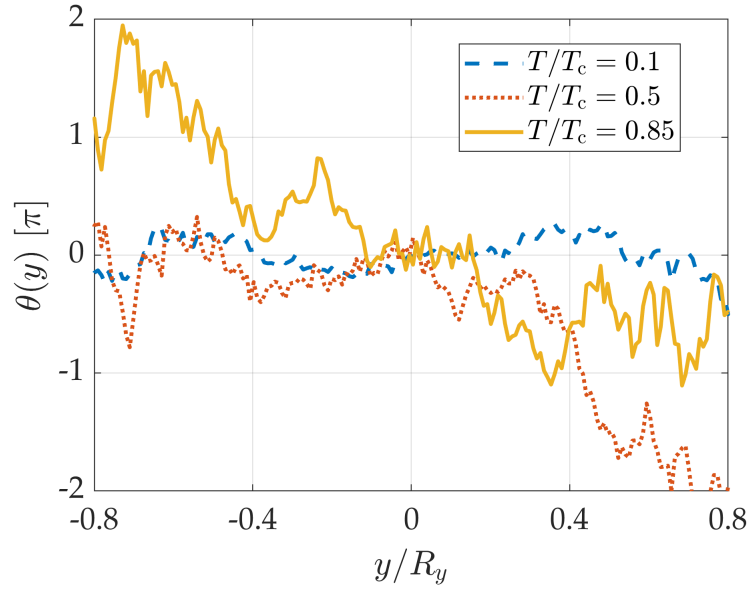
(A)
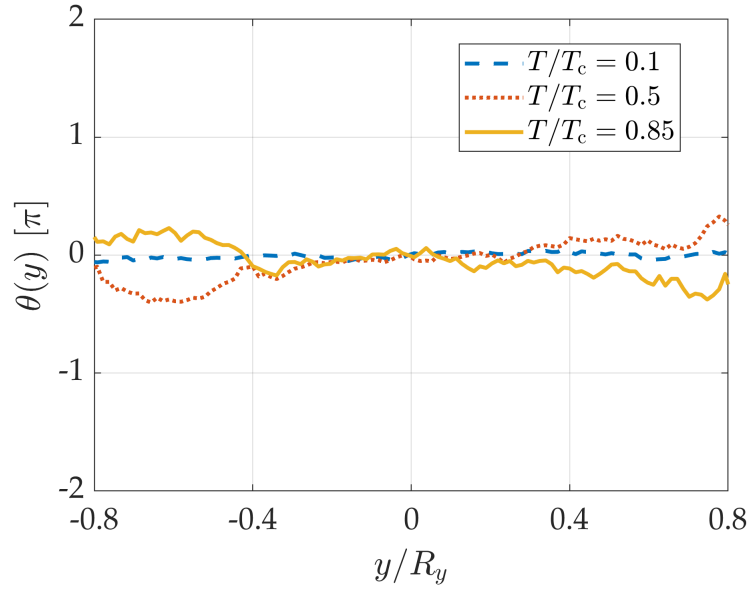
(B)

FIGURE 4.9: Phase patterns produced by Eq. (4.12) at different reduced temperatures T/T_c. (A) 1D cloud with $(\omega_\perp, \omega_\parallel) = 2\pi \times 1235\,\text{Hz}$ and $16.1\,\text{Hz}$, $N = 6.7 \times 10^3$, $\mu/\hbar\omega_\perp = 0.87$, and $L/\lambda_T = 1.35$, 6.75 and 11.5 respectively. (B) 3D cloud with $(\omega_\perp, \omega_\parallel) = 2\pi \times 395\,\text{Hz}$ and $33.7\,\text{Hz}$, $N = 9.6 \times 10^4$, $\mu/\hbar\omega_\perp = 8.37$, and $L/\lambda_T = 0.05$, 0.25 and 0.42 respectively.
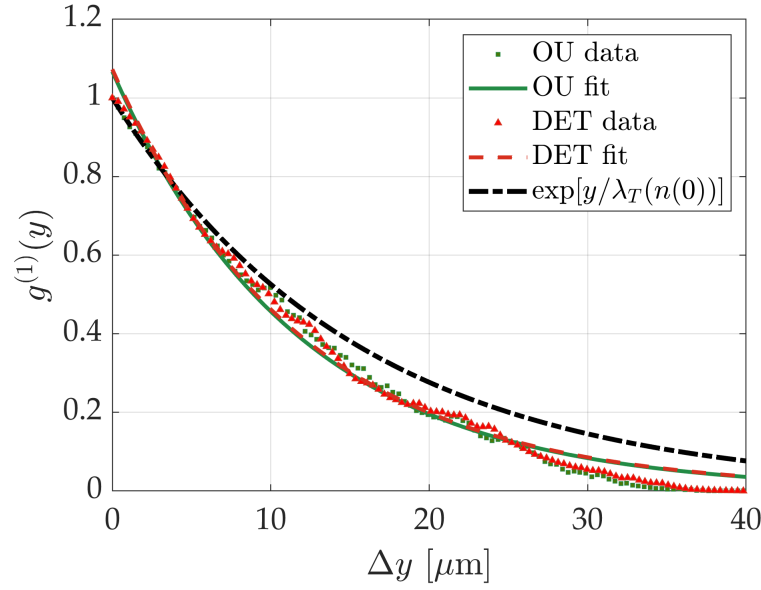
FIGURE 4.10: Correlation functions of the in-situ phase generated by the OU method (green, squares) Eq. (4.12), and the Dettmer method (red, triangles) Eq. (4.6). The black dash-dotted line indicates the expected exponentially decaying correlation function for a homogeneous gas with density equal to that of the peak density from a 1D Thomas-Fermi density profile, here $\lambda_T(n(0)) = \sim 16\,\mu$m. Both methods agree, and their exponential fits (fit to OU solid green curve, and the fit to DET is the dashed red curve) give $\lambda_T = \sim 12\,\mu$m, in reality the decay shouldn't be a pure exponential, as λ_T is spatially dependent in the inhomogenous case.

Once the phase pattern is known it can be imprinted onto the wave function which (neglecting density fluctuations) has the form of,

$$\psi(y, t = 0) = \sqrt{n_{1D}(y)} e^{i\theta(y)}. \tag{4.13}$$

The wave function after time-of-flight is then evaluated by applying the propagation operator $U(t_{\text{tof}}, 0)^2$,

$$\psi(y, t_{\text{tof}}) = \exp\left(-\frac{it_{\text{tof}}}{\hbar} \hat{H}\right) \psi(y, t = 0). \tag{4.14}$$

At $t = 0$ the potential is instantaneously switched off, assuming ballistic expansion i.e. interactions are neglected, then the Hamiltonian reduces to the kinetic energy term $\hat{H} = \frac{\hat{p}^2}{2m} = \frac{\hbar^2}{2m}\frac{\partial^2}{\partial y^2}$. The propagation is easily performed in Fourier space as a differentiation in real space becomes a multiplication in k-space. The propagator is then,

$$\mathcal{F}\left[\exp\left(-\frac{it_{\text{tof}}}{\hbar}\hat{H}\right)\right] \Rightarrow \exp\left(-i\frac{\hbar k^2}{2m}t_{\text{tof}}\right), \tag{4.15}$$

---

[2]This is only true if the Hamiltonian is time-independent.

and wave function after expansion is then [177],

$$\psi(y, t_{\text{tof}}) = \mathcal{F}^{-1}\left[\exp\left(-i\frac{\hbar k^2}{2m}t_{\text{tof}}\right)\mathcal{F}\left[\psi(y, t = 0)\right]\right]. \tag{4.16}$$

The density after time-of-flight is then simply $\rho_{1D}(y, t_{\text{tof}}) = |\psi(y, t_{\text{tof}})|^2$, and the power spectrum can be calculated with Eq. (4.8). A comparison of the four models for a 1D cloud is shown in Fig. 4.11.
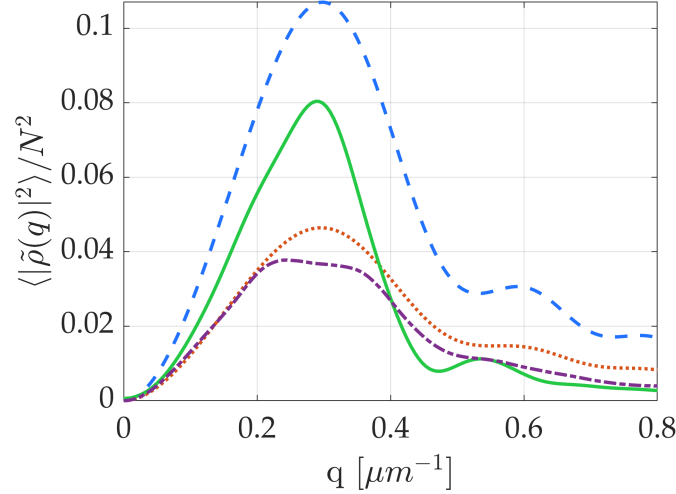

FIGURE 4.11: Theoretical predictions of density ripple power spectra for the homogeneous case with $n_{1D} = n(0)$ (blue, dashed), the LDA simulation (red, dotted), simulation based on Dettmers result Eq. (4.7) average of 200 realisations (green, solid), and the OU simulation average of 200 realisations (purple, dash-dotted). Cloud parameters $(\omega_\perp, \omega_\parallel) = 2\pi \times 1235\,\text{Hz}$ and $16.1\,\text{Hz}$, $N = 6.7 \times 10^3$ $\mu/\hbar\omega_\perp = 0.87$, with $\sigma_{\text{psf}} = 4\,\mu\text{m}$.

We observe that the OU and LDA approach give good agreement. This is useful for numerical calculations, as the LDA is simply calculated from an analytical formula, whereas the OU method requires perform multiple Fourier transforms across many realisations. Though the question remains, which method is more accurate in predicting experimental observations? We shall explore the answer to this question in the next section 4.2. It is expected that Dettmer's result should differ from the LDA and OU methods, as it takes into account interactions during the initial period of expansion after trap switch-off and also assumes relatively small fluctuations of the phase. What is unusual is that the amplitude of the first peak is significantly higher, which is in contrast to what one might expect for a model that assumes small fluctuations *a priori*. It also predicts the amplitude of $\langle|\tilde{\rho}(q)|^2\rangle/N^2$ at high q is lower than in the other models.

4.1.5   Stochastic Gross-Pitaevskii Equation

We should note that another theoretical model not discussed in this thesis is the application of the stochastic Gross-Pitaevskii equation (SGPE) [178, 179] to generate the distrubtion of the phase within the gas. The SGPE adds a complex noise term to the GPE to account for density and phase fluctuations from low lying modes and in contrast to the regular GPE it is able to model clouds at finite temperature. It has been used to analyse previous experimental work, [180–182]. We are considering extending the research reported in this thesis to include this model, however to this date the work has not been carried out.

4.2   Equilibrium properties: experiment

This section describes the data acquisition and analysis procedure, presents the results, and discusses our findings.

4.2.1   Acquisition and analysis procedure

The aim of our acquisition process is to extract measurements of the power spectra and second order correlation function, for varying trap parameters, and across the 1D-3D crossover regime.

Step 1 - Absorption images are captured of many realisations (we typically take ~ 500 images for each cloud) of the same cloud parameters, i.e. trap frequencies $\omega_\perp$ and $\omega_\parallel$, atom number N, and temperature T. The optical densities are obtained and a fringe removal algorithm (see Fig. 3.24) is applied, the OD images are then fitted and the column density distribution is extracted.
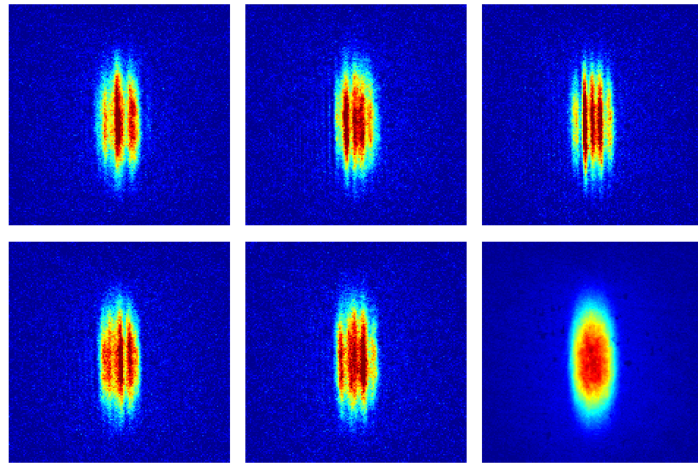

FIGURE 4.12: Five single shot optical density images from one data set, clearly showing the fluctuations are randomly changing shot to shot. The final image is an average of 250 shots, the random nature of the fluctuations means that the density profile of the mean is smooth.

Step 2 - Images are fitted to extract size, atom number, and temperature (see Section 3.3.1), an example is shown in Fig. 4.13. We then post-select the data by atom number N, and Thomas-Fermi radius R_y, in order to reduce the spread of these parameters in the data set, in theory only atom number N should need to be used, however our experiment is prone to temperature drifts which have a secondary knock-on effect that can cause the trap frequencies to vary slightly. Post-selection typically leaves >200 images, though this varies depending on the experimental stability during the acquisition.
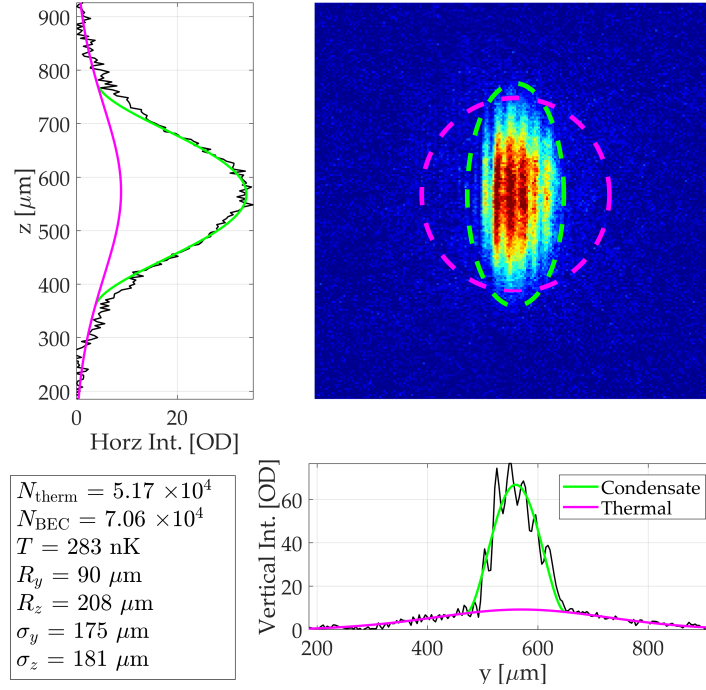

FIGURE 4.13: Example of fit of bimodal cloud, consisting of thermal part (magenta) together with a phase-fluctuating BEC (green), with trap frequencies $\omega_\perp = 2\pi \times 1005\,\mathrm{Hz}$, and $\omega_\parallel = 2\pi \times 16.9\,\mathrm{Hz}$.

Step 3 - Post-selected images are then processed to obtain the density residuals, $\delta\rho(y)_j$. First the thermal component is removed by subtracting its contribution using the fit. This ensures that atom number variation in the thermal fraction does not play a role, although these variations would only contribute to the low/DC part of the spectrum, we consider it good practice to remove it. We then crop out the background such that only the condensate remains, thereby minimising any contribution to the power spectrum from detector noise. After cropping, the image is vertically integrated to get the line density $\rho(y, t_{\mathrm{tof}})$. The density residual for each shot is calculated by subtracting the mean of all shots. This process is shown in Fig. 4.14.
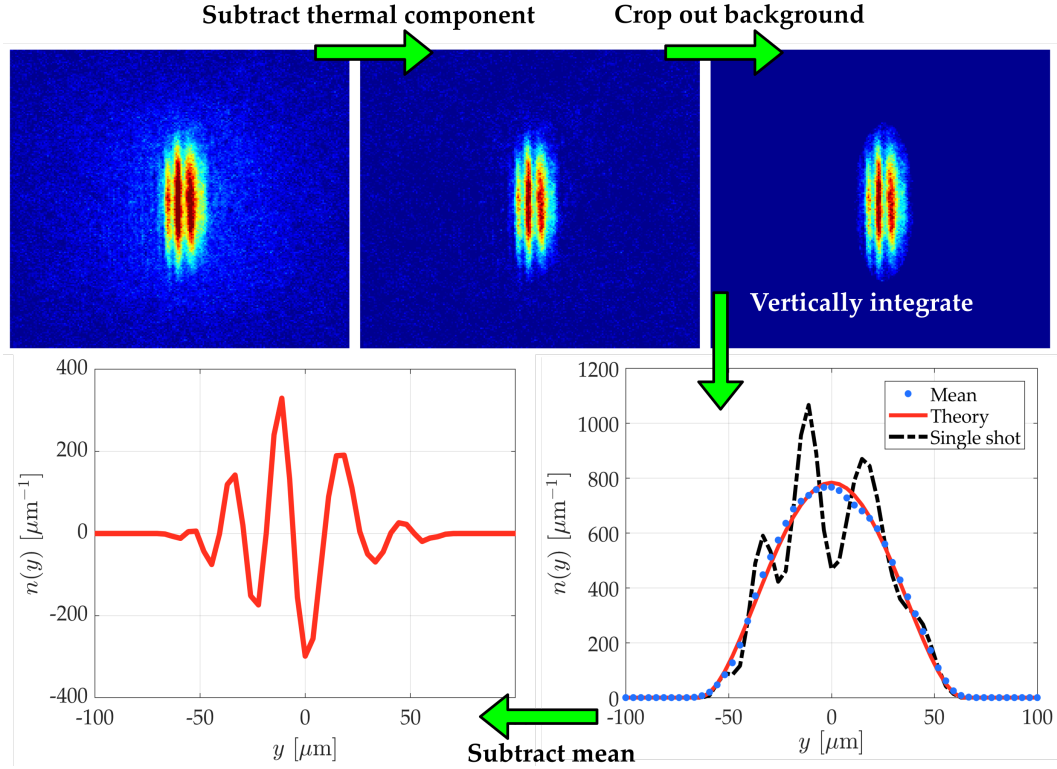
FIGURE 4.14: Image processing to extract $\delta\rho(y)_i$ from absorption images of a phase fluctuating cloud. The original optical density image is shown in the the top left, using the fit the thermal component is subtracted. An elliptical crop is performed using R_y and R_z obtained from fitting. The cropped image is then vertically integrated and converted from optical density into atomic density (black dashed line, bottom right). Finally the mean line density (blue dots, bottom right) is subtracted to obtain the residual density fluctuations $\delta\rho(y)$ (red solid line, bottom left). Here the prediction for the density profile after time-of-flight is plotted (red solid line, bottom right) using the self similar solutions from [183] which is valid in the Thomas-Fermi regime.

Step 4a - Calculate power spectrum of the density ripples, $\langle|\tilde{\rho}(q)|^2\rangle/N^2$, using Eq. (4.8). For each residual $\delta\rho(y)$ the modulus square of the Fourier transform is calculated and then normalised by atom number to get power spectrum of a single cloud $|\tilde{\rho}_j(q)|^2/N_j^2$, where j is the shot number. Artificial fringes can arise in the residuals, $\delta\rho(y)_j = \rho_j(y) - \langle\rho(y)\rangle$, if there is positional variation of the cloud along y, this is accounted for by centering each density profile. The mean of the spectra is then computed to get $\langle|\tilde{\rho}(q)|^2\rangle/N^2$. Examples of the single shot spectra and their corresponding mean are shown in Fig. 4.15. Once we have obtained the mean power spectrum we fit the measurement with the LDA Eq. (4.5), and extract two features, the peak position $q_1^{\max}$, and the peak amplitude $\langle|\tilde{\rho}(q_1^{\max})|^2\rangle/N^2$, which can be seen in Fig. 4.15. Evaluation the shot noise of the camera found a noise floor well below ($\ll 1\,\%$) the smallest $\langle|\tilde{\rho}(q_1^{\max})|^2\rangle/N^2$ measured.
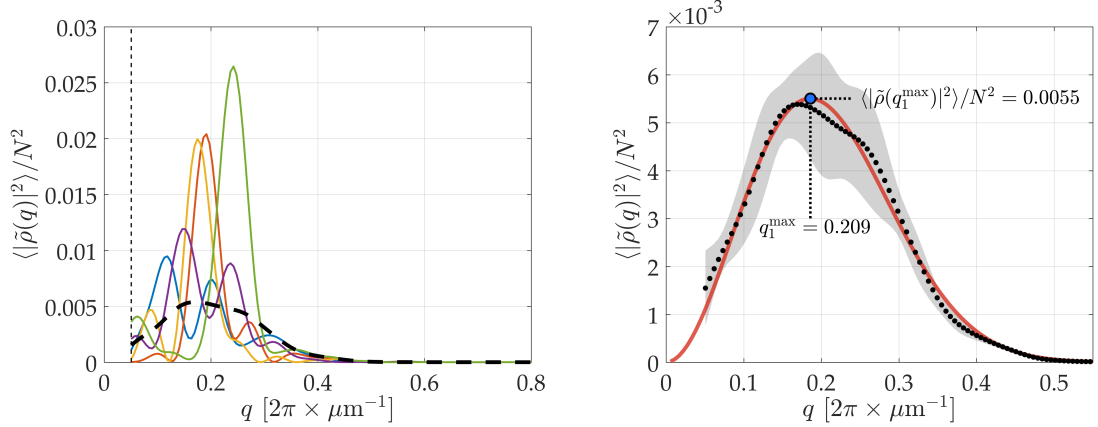
FIGURE 4.15: (Left) Mean power spectrum $\langle|\tilde{\rho}(q)|^2\rangle/N^2$ of a phase fluctuating cloud (black, dashed), five example spectra of single shots are shown (solid, coloured). The mean of the spectra is taken from a total of 250 shots. The inverse cloud length is indicated by the black dashed line, contributions below this line typically come from variations in total atom number. (Right) Fit with the LDA simulation (red, solid) to the measured spectrum (black, dotted) which has uncertainty indicated by the grey shaded region, all fit parameters (N, T, t_{tof}, and σ_{psf}) have been left free to give the best fit (as opposed to Fig. 4.3 where only T is a free parameter so the temperature can be estimated). The magnitude and position of the peak is extracted, as indicated in the plot.

Step 4b - Calculate density-density correlations, in this case we use the averaged two-point correlation function $\tilde{g}^{(2)}(y)$, introduced in [94]. The autocorrelation for each density profile is computed $G_j^{(2)} = \int \rho_j(u)\rho_j(u+y)du$, and the mean taken to attain $G^{(2)} = \langle \int \rho(u)\rho(u+y)du \rangle$. This result is then normalised with the autocorrelation of the mean density profile,

$$\tilde{g}^{(2)}(y) = \frac{\langle \int \rho(u)\rho(u+y)du \rangle}{\int \langle \rho(u) \rangle \langle \rho(u+y) \rangle du}. \tag{4.17}$$

An example measurement is displayed in Fig. 4.16, the corresponding power spectrum can also be seen in Fig. 4.15. The theoretical prediction for a homogeneous gas with the same temperature, and peak density is plotted in comparison.
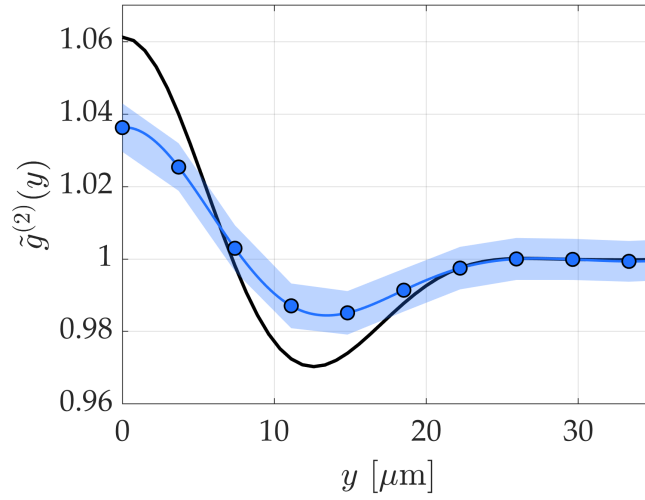
FIGURE 4.16: Normalised two-point density correlation function for a phase fluctuating cloud. (Blue dots) Experimentally measured $\tilde{g}^{(2)}(y)$, the surrounding blue shaded area indicates the statistical uncertainty. (Black solid line) Theoretical prediction for a homogeneous gas [93] using Eq. (4.1) and Eq. (2.66).

4.2.2 Results and Discussion

In this section I present our results, and also discuss our conclusions. First I review the theoretical models mention in the previous section, second the effect of interactions during time of flight, and finally the driving parameters of the 3D-1D crossover.

Comparison of theoretical models and hydrodynamic expansion

A comparison of the power spectrum $\langle|\tilde{\rho}(q)|^2\rangle/N^2$ predicted by all models with an experimental measurement of a 1D cloud is displayed in Fig. 4.17. We see that the Ornstein-Uhlenbeck simulation gives the best match. The prediction from the LDA is also a near match, this method has its advantages as mentioned in Section 4.1.2 it is computationally much simpler than the OU method.
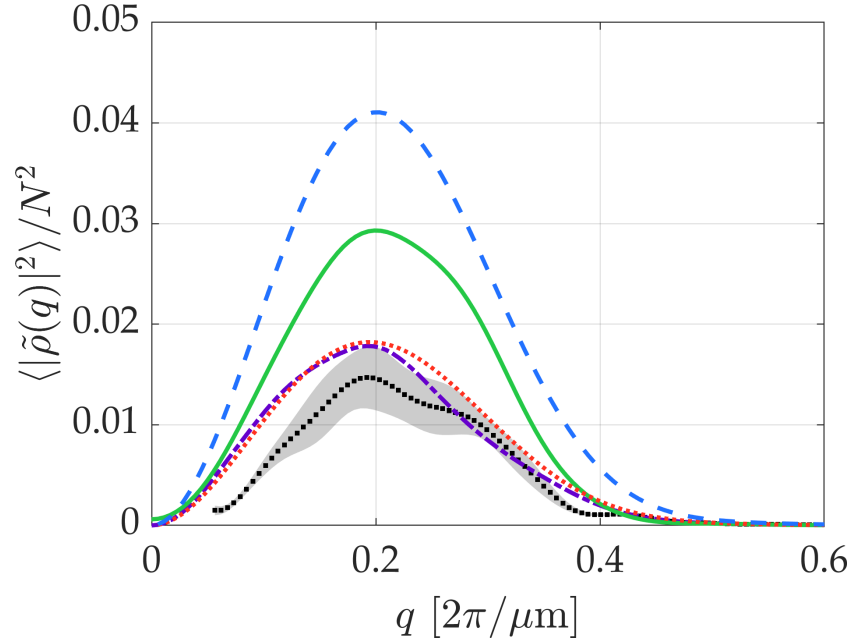
FIGURE 4.17: Density ripple power spectra from the homogeneous case with $n_{1D} = n(0)$ (blue, dashed), the LDA (red, dotted), the Dettmer model with 200 realisations (green, solid), the OU model with 200 realisations (purple, dash-dotted), and the experimental measurement (black squares) the shaded region indicates the statistical uncertainty. The interaction correction $\mathcal{C}_{\text{int}}$ has been applied to the OU and LDA spectra. The cloud parameters are $(\omega_\perp, \omega_\parallel) = 2\pi \times 1235\,\text{Hz}$ and $16.1\,\text{Hz}$, $N = 6.7 \times 10^3$ $\mu/\hbar\omega_\perp = 0.84$, with $\sigma_{\text{PSF}} = 4\,\mu\text{m}$.

To give a quantitative measure of the agreement between the theory and the data we define a quantity δ_ρ,

$$\delta_\rho = \frac{\int dq |\langle|\rho(q)|\rangle_{\text{theory}} - \langle|\rho(q)|\rangle_{\text{exp}}|}{\int dq \langle|\rho(q)|\rangle_{\text{exp}}}, \tag{4.18}$$

which can be understood as the relative difference between the theory and the measurement. In other words, if $\delta_\rho = 0$ then the theoretical prediction is a perfect match to the measurement. This quantity is plotted versus L/λ_T in Fig. 4.18.
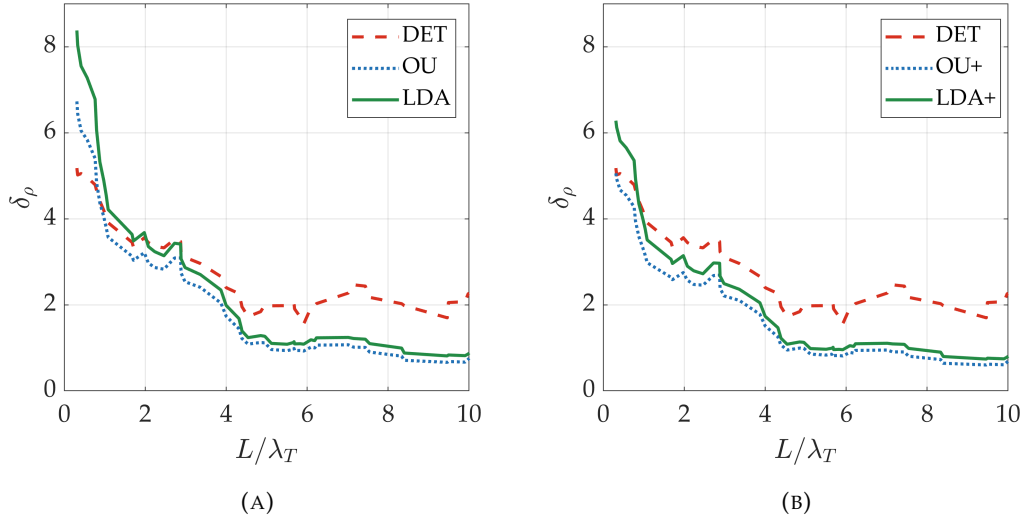
FIGURE 4.18: Moving mean of δ_ρ plotted versus L/λ_T. The moving mean (an average over $\pm$ 3 data points) is used in order to extract the general trend of the data. (A) The three inhomogeneous density models are compared, (red, dashed) Dettmer, (blue, dotted) OU, (green, solid) LDA. (B) The interaction correction $\mathcal{C}_{\text{int}}$ is applied on the OU and LDA, (red, dashed) Dettmer, (blue, dotted) OU+, (green, solid) LDA+.

We observe that the OU method gives best the agreement across the most of the parameter space, however it only gives a good agreement ($\delta_\rho \lesssim 1$) in the 1D regime. Whilst our experiment does not probe deep into the 1D regime, the OU method has been used successfully in other experiments that do [172–174, 184]. Towards the 3D end of the parameter space ($L/\lambda_T \leq 1$), we see that Dettmer's model becomes the best predictor of the power spectrum, however δ_ρ is high, Fig. 4.19 shows an example of the spectra for $L/\lambda_T \sim 0.5$. Dettmer's model appears to correctly predict the peak position q_1^{max}, but not the peak amplitude $\langle|\tilde{\rho}(q_1^{\text{max}})|^2\rangle/N^2$, diverging significantly from other models around $L/\lambda_T \sim 4$. Applying the interaction correction $\mathcal{C}_{\text{int}}$ (Eq. (4.11)) given in [96] to the OU model (from hence forth I will refer to the interaction corrected OU/LDA models as OU+/LDA+), partially recovers Dettmer's prediction (this can be seen in Fig. 4.19 and Fig. 4.18b) indicating that the derivation of $\mathcal{C}_{\text{int}}$ is valid.
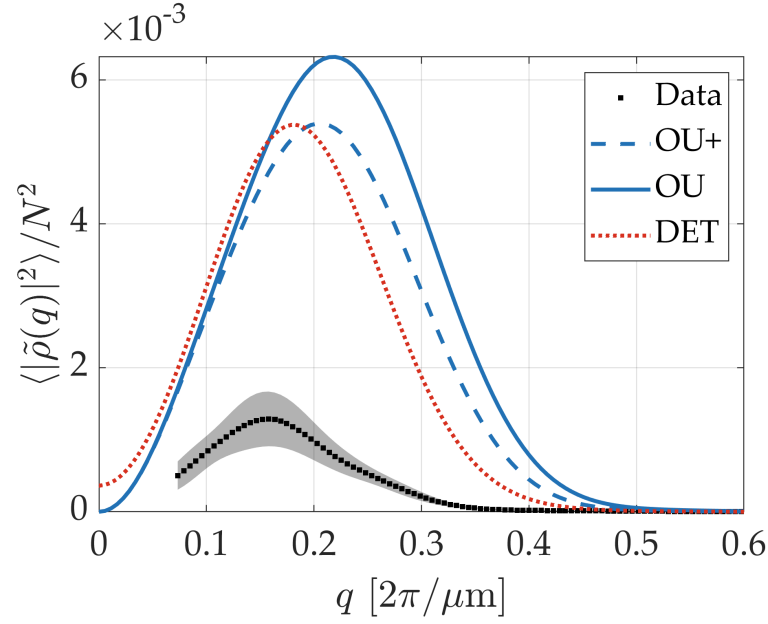
FIGURE 4.19: Density ripple power spectra $\langle|\tilde{\rho}(q)|^2\rangle/N^2$ for a cloud in the 3D limit with $L/\lambda_T = 0.42$ and $\mu/\hbar\omega_\perp = 7.1$ (black squares, shaded region indicates statistical uncertainty), with theoretical predictions of Dettmer (red, dotted), OU (blue, solid), and OU+ (blue, dashed).

A qualitative explanation of the effects of interactions can be understood as follows, immediately after the trapping potential is switched off the cloud undergoes hydrodynamic expansion, in this stage the interaction energy still plays a role, however it is quickly converted into kinetic energy causing the gas to undergo accelerated expansion in the radial direction. Once the interaction energy becomes negligible the expansion is ballistic, and size increases at a constant rate. In the Thomas-Fermi regime the radial size during expansion is given by, $R_\perp(t) = R_\perp(0)\sqrt{1 + (\omega_\perp t)^2}$ [183], in 1D the scaling is the same except $R_\perp$ is replaced with $a_\perp$ (see Eq. (2.51)). The timescale of hydrodynamic expansion is determined by the inverse of the trapping frequency $t_{\text{hydro}} = (\omega_\perp/2\pi)^{-1}$, in our experiment this ranges from $0.75\,\text{ms}$ to $2.5\,\text{ms}$. Thus for weaker radial confinement the hydrodynamic expansion time is longer, and whilst in this regime momentum transfer can occur between the radial and axial directions. This creates an additional axial velocity to the velocity field already present from the phase gradients, causing the density to spread out further than would be observed without interactions. Hence the separation of the density fringes will increase shifting q_1^{max} to a lower spatial frequency. This effect was observed in a 2D gas [98] and described theoretically in [162], in 2D systems the effect of interactions are stronger as the cloud only expands fast in one dimension.
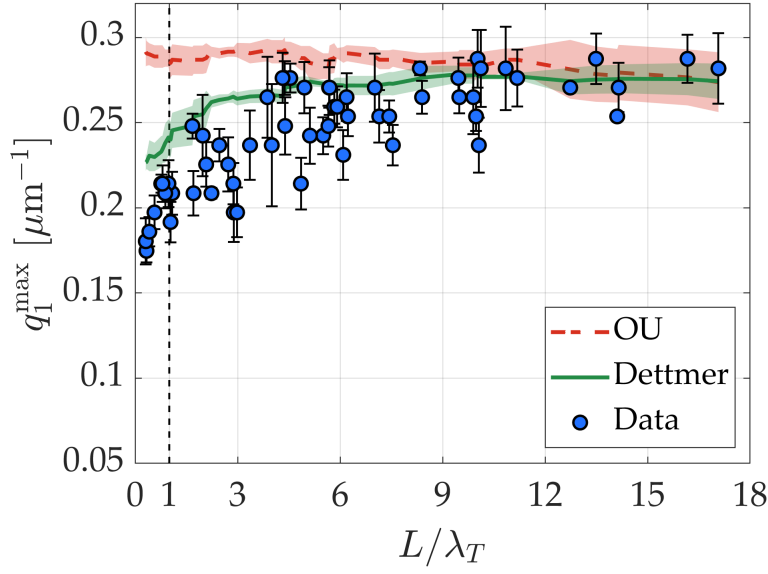
(A)
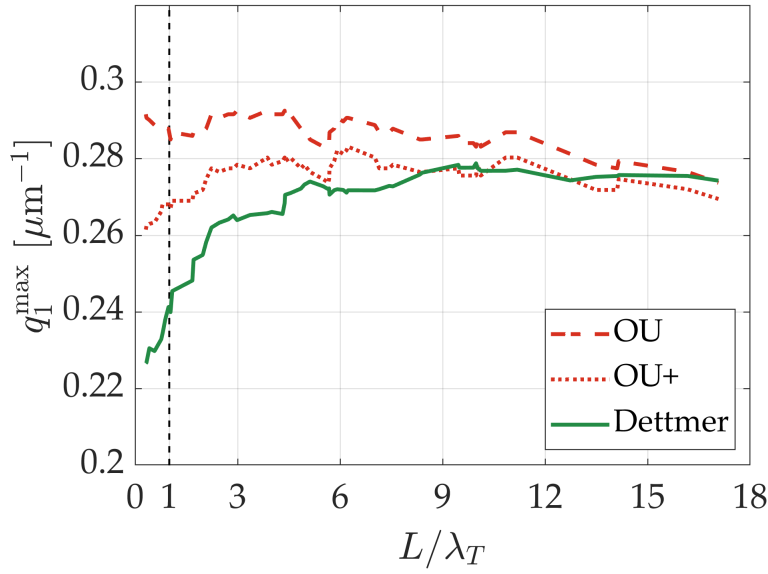
(B)

FIGURE 4.20: (A) Peak position q_1^{max} versus L/λ_T, blue dots indicate the measured data, the errorbars display the statistical uncertainty. For visibility the moving mean of the theoretical predictions, OU (red, dashed), Dettmer (green, solid), have been plotted, the shaded regions indicate the moving standard deviation. (B) Applying the interaction correction $\mathcal{C}_{\mathrm{int}}$ to the OU model almost recovers the predictions of Dettmer's model. (Red, dashed) OU model, (red, dotted) OU+ model, and (green, solid) Dettmer.

Figure 4.20 shows the peak position versus L/λ_T, which is loosely related to t_{hydro} as weaker transverse confinement decreases L and increases λ_T (assuming N, T, and $\omega_\parallel$ remain fixed). In general, at high L/λ_T interactions become negligible and the peak

position should be determined by t_{tof} (see Eq. (4.3b)) only. Since time-of-flight is fixed $q_1^{\max}$ should be constant, at sufficiently high L/λ_T we observe in the data and theory a convergence of the peak position to a constant value of $q_1^{\max} = \sim 0.28\,\mu\text{m}^{-1}$. As L/λ_T becomes smaller the cloud behaves more and more like a true BEC, and as a side effect (from manipulating the trapping potential) the interactions during time-of-flight become important, thus shifting $q_1^{\max}$ to lower values. Again this behaviour is observed in the data and Dettmer's prediction, however the magnitude of the measured shift is greater than predicted, and as expected this shift is not observed in the OU model. Applying the interaction correction (Eq. (4.11)) somewhat successfully replicates Dettmer's model in terms of peak position, the OU+ model now shows a shift of $q_1^{\max}$ but to a lesser extent than Dettmer's model (see Fig. 4.20b).

In conclusion Dettmer's approximation is qualitatively valid in explaining the effect of interactions on the spatial frequency of the density ripples, however it incorrectly estimates the size of the resulting density fluctuations. The OU model provides a better estimate on the size of the fluctuation, and adapting the model with the interaction correction from [96] gives a good approximation of Dettmer's result, therefore we find that the OU+ model is the best estimate of the density ripples in the crossover.

1D-3D crossover regime

In this section we explore the drivers of phase fluctuations throughout the dimensional crossover. Figure 4.21 displays the parameter space sampled with our data and compares it to previous experimental work, showing that our data spans a large range of the crossover.
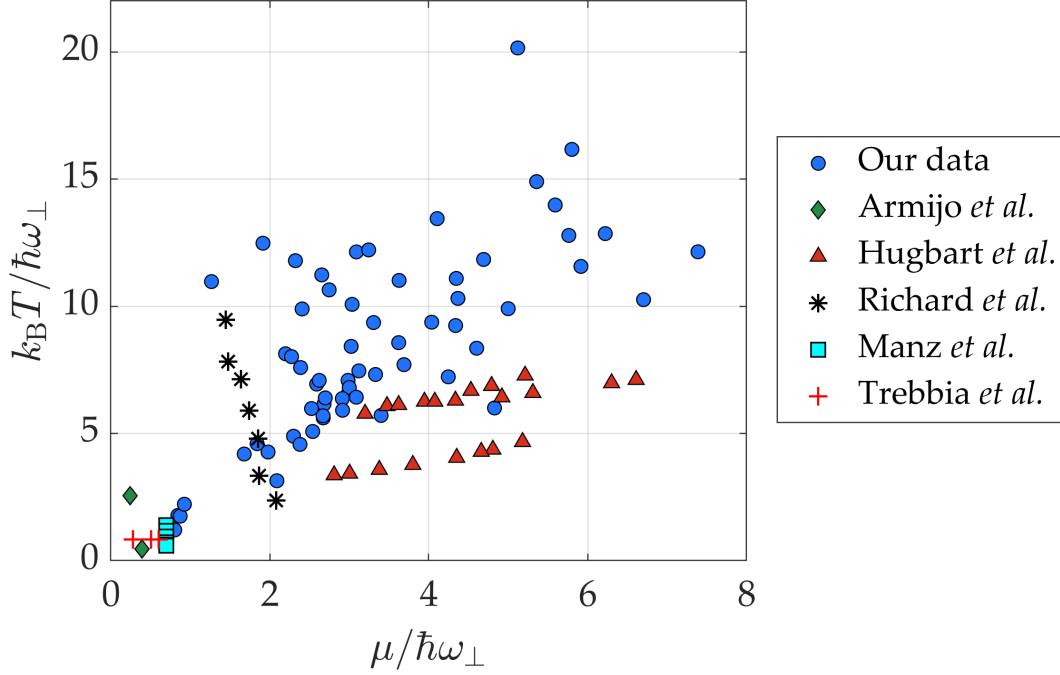

FIGURE 4.21: Dimensional parameter space explored in terms of $\mu/\hbar\omega_\perp$ and $k_\mathrm{B}T/\hbar\omega_\perp$ with comparison to previous experimental work. Our data (blue, dots), Armijo *et al.* [28] (green, diamonds), Hugbart *et al.* [37] (red, triangles), Richard *et al.* [36] (black, stars), Manz *et al.* [94] (cyan, squares), and Trebbia *et al.* [185] (red, crosses).

From the results in Section 4.2.2 we postulate that peak position q_1^max is influenced in the majority by interactions during time-of-flight, and therefore, is not a direct indicator of "3D-ness". The peak position is also affected by the finite optical imaging resolution, however, this is only a technical limitation and the affect is the same on all of the data. To parameterise the strength of the fluctuations we use the quantity $\tilde{g}^{(2)}(0)$, from Eq. (4.17) (similarly the peak of the power spectrum can also be used $\langle|\tilde{\rho}(q_1^\mathrm{max})|^2\rangle$, since they are related as a Fourier transform pair by the Wiener-Khinchin theorem [186, 187]). This is the likelihood of finding two particles in the same location, relative to the mean density. A fully coherent 3D BEC would not experience any fluctuations and the single shot density would be equal to the mean density giving $\tilde{g}^{(2)}(y) = 1$. As fluctuations appear bunching in the density ripples is observed and $\tilde{g}^{(2)}(y) > 1$.

We probe the dimensional crossover up to $\mu/\hbar\omega_\perp \lesssim 1$ and $k_\mathrm{B}T/\hbar\omega_\perp \gtrsim 1$, partly due to experimental limitations and also the fact that the deeply 1D regime $(\mu, k_\mathrm{B}T)/\hbar\omega_\perp \ll 1$ has already been thoroughly explored [27, 28, 94, 142, 173, 188]. It has also been

observed that the physics of the degenerate part is effectively 1D if $\mu/\hbar\omega_\perp < 1$ even though the thermal condition $k_B T/\hbar\omega_\perp < 1$ is not satisfied [5, 25].
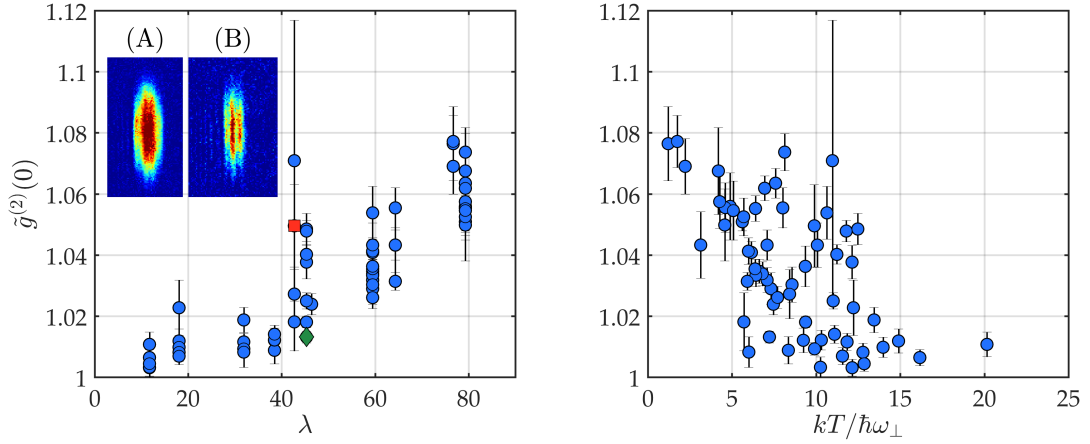

FIGURE 4.22: (Left) $\tilde{g}^{(2)}(0)$ vs. aspect ratio ($\lambda = \omega_\perp/\omega_\parallel$), the errorbars indicate the statistical uncertainty. Inset (A)/(B) is a single shot optical density image taken from the data-set indicated by the green diamond/red square. (Right) $\tilde{g}^{(2)}(0)$ vs. $kT/\hbar\omega_\perp$, errorbars indicate the statistical uncertainty.

Our experiment measures multiple clouds in the parameter space given in Section 3.4.1. From Fig. 4.22 we observe that aspect ratio doesn't appear to have a true bearing on the "1D-ness" of the system, as at a fixed aspect ratio there can be a wide range of fluctuation strength $\tilde{g}^{(2)}(0)$. Using $\lambda \sim 45$ as an example $\tilde{g}^{(2)}(0)$ varies from 1.01 to 1.07, example optical density images are shown in Fig. 4.22. Instead aspect ratio should be thought of as a practical tool that allows for the presence 1D or 3D system, i.e. it is easier to make a 1D system with high aspect ratios and a 3D system with low aspect ratios. Figure 4.22 also shows that the 1D thermal parameter $k_B T/\hbar\omega_\perp$ is only very weakly correlated with $\tilde{g}^{(2)}(0)$, implying that $k_B T/\hbar\omega_\perp$ is not a relevant parameter when determining the dimensionality of the gas.
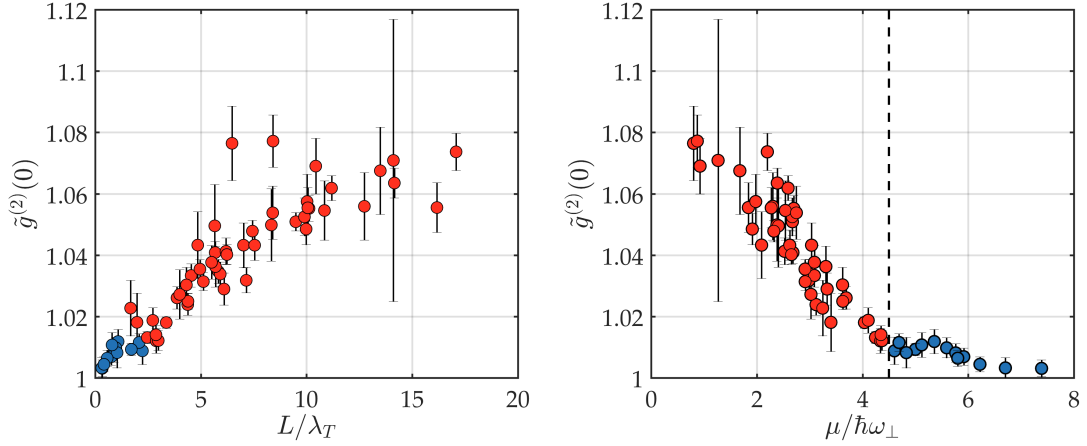
FIGURE 4.23: (Left) $\tilde{g}^{(2)}(0)$ vs. L/λ_T, red points indicate clouds with $\mu/\hbar\omega_\perp < 4.5$, and the errorbars indicate the statistical uncertainty. (Right) $\tilde{g}^{(2)}(0)$ vs. $\mu/\hbar\omega_\perp$, the black dashed line indicates an approximate threshold value of $\mu/\hbar\omega_\perp \sim 4.5$. Above the threshold fluctuations start to increase significantly.

Figure 4.23 shows the significance of $\mu/\hbar\omega_\perp$, we see a threshold value at ~ 4.5, surpassing this threshold the magnitude of fluctuations rapidly increases. Indicating that the onset of phase fluctuations is driven by the chemical potential $\mu/\hbar\omega_\perp$. We also observe a strong correlation between $\tilde{g}^{(2)}(0)$ and L/λ_T, however we suggest instead this should be thought of as a change in "sampling window", the degree of fluctuation increases when a larger window is viewed, but the physics is still set by the chemical potential $\mu/\hbar\omega_\perp$. Consider an elongated gas that is quasi-1D ($\mu/\hbar\omega_\perp \ll 1$), viewing a section of the gas of length equal to λ_T, you would observe a fully phase coherent object, however the radial degrees of freedom remain frozen out and so the dimensionality has not changed.
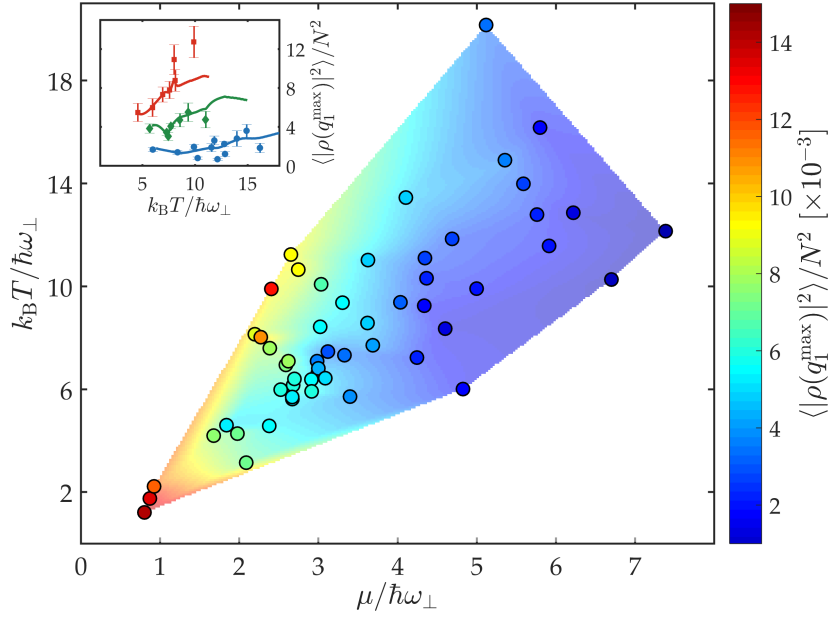
FIGURE 4.24: (Visualisation of the parameter space in terms of dimensional quantities, $k_{\mathrm{B}}T/\hbar\omega_{\perp}$ and $\mu/\hbar\omega_{\perp}$. The surface is a 2D interpolation of the acquired data (dots), here the colourscale shows the amplitude of the power spectrum $\langle|\rho(q_1^{\mathrm{max}})|^2\rangle/N^2$. (Inset) $\langle|\rho(q_1^{\mathrm{max}})|^2\rangle/N^2$ versus $k_{\mathrm{B}}/\hbar\omega_{\perp}$ for (blue, dots) $\mu/\hbar\omega_{\perp} > 4.5$, (green, diamonds) $\mu/\hbar\omega_{\perp} \sim 3.4$, and (red, squares) $\mu/\hbar\omega_{\perp} \sim 2.3$. The solid lines are cuts through the 2D interpolation shown in the main figure.

In Fig. 4.24 we explore the data in terms of the two stricter one-dimensional parameters $\mu/\hbar\omega_{\perp}$ and $k_{\mathrm{B}}T/\hbar\omega_{\perp}$. We see that the strength of the phase fluctuations is more strongly influenced by temperature $k_{\mathrm{B}}T/\hbar\omega_{\perp}$ when the chemical potential $\mu/\hbar\omega_{\perp}$ is low. It appears if the chemical potential $\mu/\hbar\omega_{\perp}$ is sufficiently high phase fluctuations remain small regardless of $k_{\mathrm{B}}T/\hbar\omega_{\perp}$, this can be seen in the inset of Fig. 4.24. This figure supports the conclusion from Fig. 4.23 that the chemical potential is the driver of dimensionality, but also reveals the importance of $k_{\mathrm{B}}T/\hbar\omega_{\perp}$ at lower $\mu/\hbar\omega_{\perp}$ which cannot be deduced from Fig. 4.22.
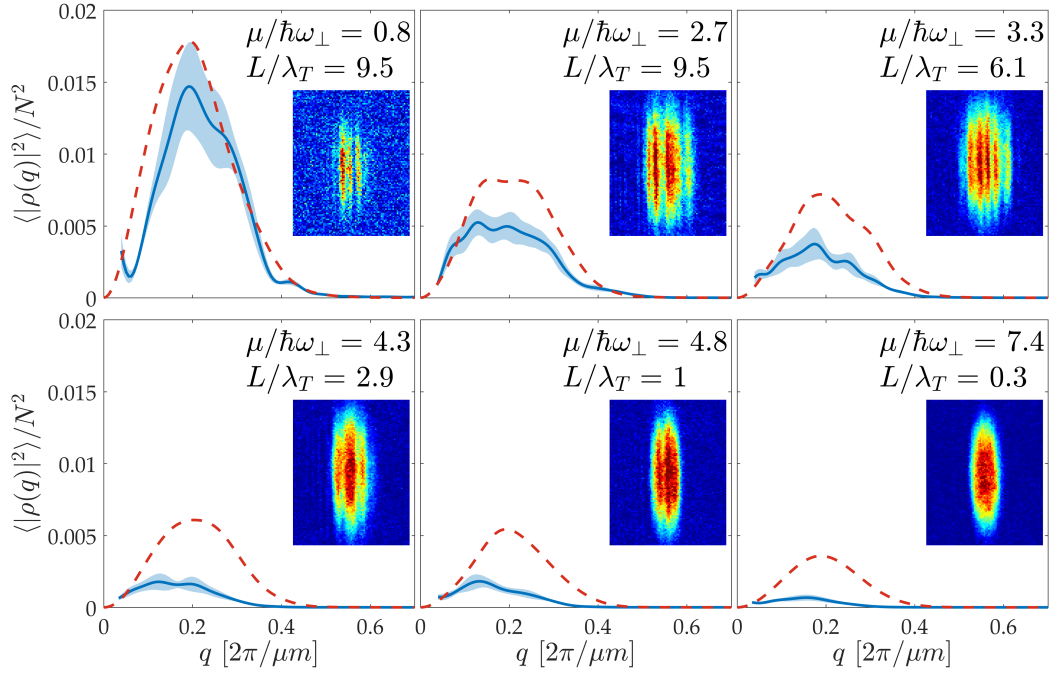
FIGURE 4.25: Six examples of a measured power spectrum (blue, solid) with varying values of L/λ_T and $\mu/\hbar\omega_\perp$ are compared to the prediction from the OU+ model (red, dashed). The blue shaded region indicates the statistical uncertainty on the measured data. In each plot, included is an optical density image of a single shot from within the total dataset. The discrepancy between prediction and measurement grows as the system becomes more coherent.

Examples of how the power spectrum of the density ripples $\langle|\tilde{\rho}(q)|^2\rangle/N^2$ changes with increasing coherence is visible in Fig. 4.25. Interestingly, there are still fluctuations (albeit very small) in what we would consider a 3D gas (bottom right of Fig. 4.25), this shows that there is no sharp transition to full phase coherence at $\lambda_T \gtrsim L$, this behaviour was also observed in reference [37] however in that article the coherence properties were characterised in terms of T/T_ϕ.

FIGURE 4.26: (Left) Measured mean power spectra of three clouds spanning the 1D-3D crossover, 1D (blue, dots) $\mu/\hbar\omega_\perp = 0.84$ and $L/\lambda_T = 9.5$, crossover (red, squares) $\mu/\hbar\omega_\perp = 3.3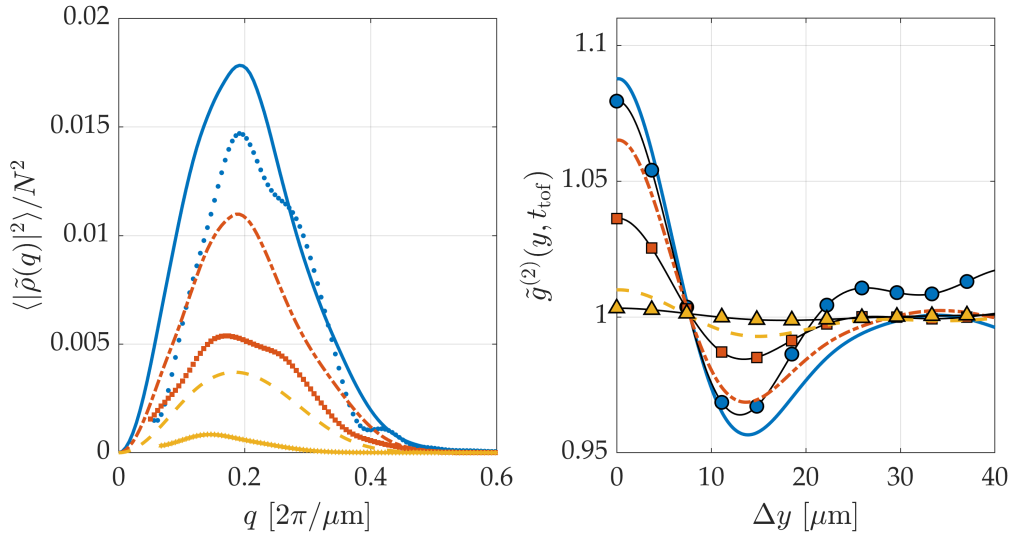$ and $L/\lambda_T = 5.7$, and 3D (yellow, triangles) $\mu/\hbar\omega_\perp = 6.7$ and $L/\lambda_T = 0.31$. For comparison the prediction from the OU+ model is plotted alongside, 1D (blue, solid), crossover (red, dash-dotted), and 3D (yellow, dashed). (Right) Normalised two-body correlation function $\tilde{g}^{(2)}(y)$, for the same three clouds, alongside the prediction from the OU+ model. The same labelling is used as in the left figure.

In Fig. 4.26 we have plotted the power spectrum $\langle|\tilde{\rho}(q)|^2\rangle/N^2$, and the normalised two-body correlation function $\tilde{g}^{(2)}(y)$, for three clouds spanning the 1D-3D crossover. In the 3D case we measure an almost flat $\tilde{g}^{(2)}(y) \approx 1$, as expected for a BEC, this is not reproduced by the OU+ prediction which overestimates the size of the fluctuations significantly, the disparity is clearer in power spectrum. In the 1D case the phase fluctuations become large and $\tilde{g}^{(2)}(0)$ grows, and the minima decreases, typical of the bunching/anti-bunching features observed in interference patterns. For the data of the 1D cloud in Fig. 4.26 (blue dots) at $\Delta y > 20\,\mu$m we see deviation from the expected value of ~ 1. We believe this could be due to a lower number of shots acquired (in this data-set there are ~ 100 shots, whereas typically each data-set contains around 200 shots) combined with the fact that density fluctuations are large compared to the mean density.

We have also investigated our data in terms of the number of low-energy axial excitations (introduced in Section 4.1.3) as they contribute to the phase fluctuations [31]. We compute the total occupation of the modes N_{1D}, which have a spectrum given by $\epsilon_j = \hbar\omega_\parallel\sqrt{j(j+3)/4}$. If $k_BT \gg \hbar\omega_\parallel$ (this is true for all of our data) the Bose occupation function can be approximated to $N_j = k_BT/\epsilon_j$. Excitations can be considered low-energy up until $\epsilon_j = \hbar\omega_\perp$, at this point the excitation becomes particle-like and do not contribute to the phase fluctuations. Thus, the total number of low-energy excitations

can be computed by,

$$N_{1D} = \sum_{j}^{\epsilon_j < \hbar\omega_\perp} k_B T / \epsilon_j. \tag{4.19}$$

We postulate that the strength of the phase fluctuations will be related to the number of coherent atoms N_{BEC} and the number of low-energy excitations N_{1D}. This appears to be confirmed in Fig. 4.27, in this figure the ratio N_{1D}/N_{BEC} is plotted against the amplitude of the power spectrum $\langle|\tilde{\rho}(q_1^{max})|^2\rangle$. We observe an approximately linear relationship between the two quantities. Even though our data covers a wide parameter space (see Fig. 4.21) we observe a collapse onto a single curve. This is strong evidence that the phase fluctuations are well described by the theoretical description in [31].
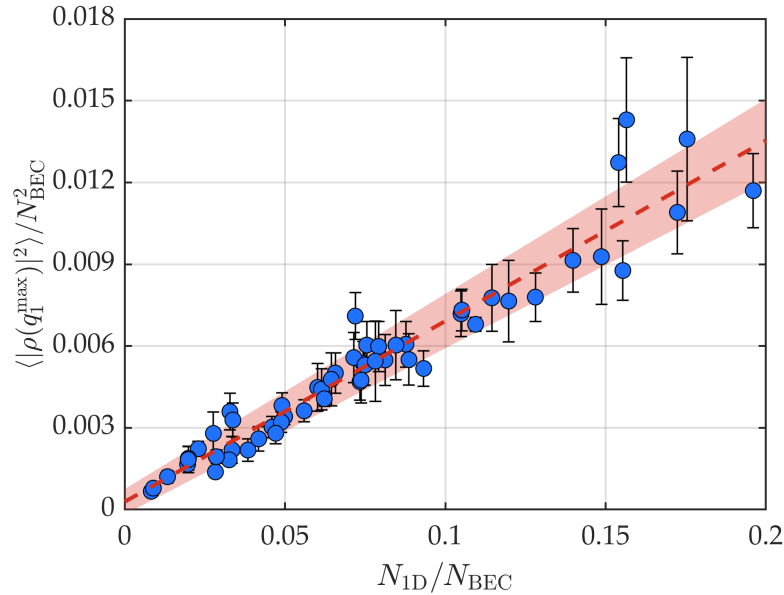
FIGURE 4.27: Relationship between the strength of the phase fluctuations $\langle|\rho(q_1^{max})|^2\rangle$ and the relative number of low-energy exciations N_{1D}/N_{BEC}. (Blue, dots) Acquired data with errorbars indicating statistical uncertainty, (red, dashed) a linear fit to the data with 95% confidence bounds represented by the shaded region.

Figure 4.27 has shown that the strength of the phase fluctuations are determined by the number of low-energy excitations N_{1D}/N_{BEC}, rather than $\mu/\hbar\omega_\perp$ or $k_B T/\hbar\omega_\perp$. This implies that the strength of phase fluctuations is not directly related to dimensionality but rather an indication of one-dimensional behaviour. In Fig. 4.24 and Fig. 4.23, we see that the phase fluctuations only become significant when the chemical potential $\mu/\hbar\omega_\perp$ is small, as such, it is the chemical potential $\mu/\hbar\omega_\perp$ that sets the dimensionality. Once the dimensionality is low enough the phase can fluctuate at an arbitrary strength set by N_{1D}/N_{BEC}.

Chapter 5

Summary and Outlook

The work reported in this thesis is summarised in this chapter, and followed up with an outlook for future extensions to the research carried out.

A number of theoretical models were described, all of which can give predictions for the power spectrum of the density ripples $\langle|\tilde{\rho}(q)|^2\rangle/N^2$, and the second-order correlation function $\tilde{g}^{(2)}(y)$. The predictions from each of the models were compared to measurements of $\langle|\tilde{\rho}(q)|^2\rangle/N^2$ and $\tilde{g}^{(2)}(y)$. We have shown that the model (from those reviewed in this thesis[1]) that fits our observations best is the interaction-corrected Ornstein-Uhlenbeck model (OU+), Section 4.1.4. The interaction-correction condenses part of Dettmer's model (Section 4.1.3) which evaluates the time-of-flight expansion into a frequency-dependent correction term $\mathcal{C}_{\text{int}}$ Eq. (4.11) taken from [96]. We have also shown that the properties of the phase-distribution $\theta(y)$ in Dettmer's model (Eq. (4.6) taken from [31]) agrees with that generated by the OU model in Eq. (4.12) (see Fig. 4.10).

The interaction-correction can also be applied to the LDA (see Section 4.1.2), the LDA+ model. The resulting predictions are only slightly worse than that of the OU+ model in the 1D regime, though the disparity increases as the 3D regime is approached (see Fig. 4.18). However, it has an advantage in the fact that it is computationally much quicker to calculate. That being said, the OU+ model is still a poor predictor of our observations in the 3D regime and consistently over estimates the size of the density ripples observed in our measurements throughout the 1D-3D crossover. However, the predictions do start to converge with experimental observations at the 1D end of the crossover.

We observe that interactions during time-of-flight act to "spread out" the density ripples, shifting density fringes to lower spatial frequencies Section 4.2.2. Whilst the interaction correction $\mathcal{C}_{\text{int}}$ improves on the results of the LDA and OU models, it does not completely recover the peak position q_1^{max} obtained from Dettmer's model (see Fig. 4.20).

Dimensional parameters, $\mu/\hbar\omega_\perp$, $k_{\text{B}}T/\hbar\omega_\perp$, $\omega_\perp/\omega_\parallel$, and L/λ_T were explored in the 1D-3D crossover regime in Section 4.2.2. We found that neither aspect ratio $\omega_\perp/\omega_\parallel$ nor L/λ_T had a real bearing on dimensionality. In contrast to the expectations from [45] and the findings of [28], we found that $k_{\text{B}}T/\hbar\omega_\perp$ did not characterise dimensionality in

---

[1]We note that use of the SGPE may provide better predictions, and requires further investigation.

the crossover well (see Section 4.2.2). Instead we observed that the chemical potential $\mu/\hbar\omega_\perp$ was the key parameter that drove 1D behaviour, supporting the claims from previous experiments [5, 25]. Finally, we saw that the size of the phase fluctuations can be determined by the total occupation of low-energy axial excitations N_{1D}/N_{BEC}. However, this quantity cannot be directly related to dimensionality, although a non-zero value indicates the presence of 1D behaviour.

Our experiment suffered a number of limitations that could be improved for the future generations of the experiment. Our poor optical imaging resolution of $\sim 10\,\mu m$ suppresses information of the high frequency end of the density ripple spectra. Preliminary designs with custom-built optics suggest this could be improved to $\sim 3\,\mu m$ with our current science chamber. This could be further improved by increasing the numerical aperture, for example by using a recessed window. A high imaging resolution coupled with a long time-of-flight should make it possible to resolve q_2^{max}, which to date, has not been observed in a 1D gas.

The range of accessible aspect ratios λ was ultimately limited by fragmentation effects (see Section 3.2.3), which were observed at distances of $100\,\mu m$ from the chip surface, this is relatively large distance compared to other experiments [57]. A replacement atom chip has been manufactured, which we hope has a much smaller surface roughness. Whilst it was possible to create traps of lower aspect ratios (without fragmentation) than used in this thesis, the cloud tilt (see Section 3.3.3) became too large to image density ripples effectively. Reducing the fragmentation would allow us to trap the atoms closer to the chip surface, reducing the magnitude of the tilt, and also give us access to larger $\omega_\perp$, thus expanding both the low and high end of accessible aspect ratios λ.

Dimensional quench

One possible extension to this research would be to analyse the non-equilibrium dynamics of the phase within a system. Starting with a 3D system and rapidly changing the potential to change dimensionality to 1D (or other way around). Such a rapid change to the system is often referred to as a "quench". As such this experiment would be to perform a dimensional quench, the concept is shown in Fig. 5.1. Initial attempts at the dimensional quench show the excitation of breathing modes [189]. A measurement of the breathing mode frequency is displayed in Fig. 5.2.
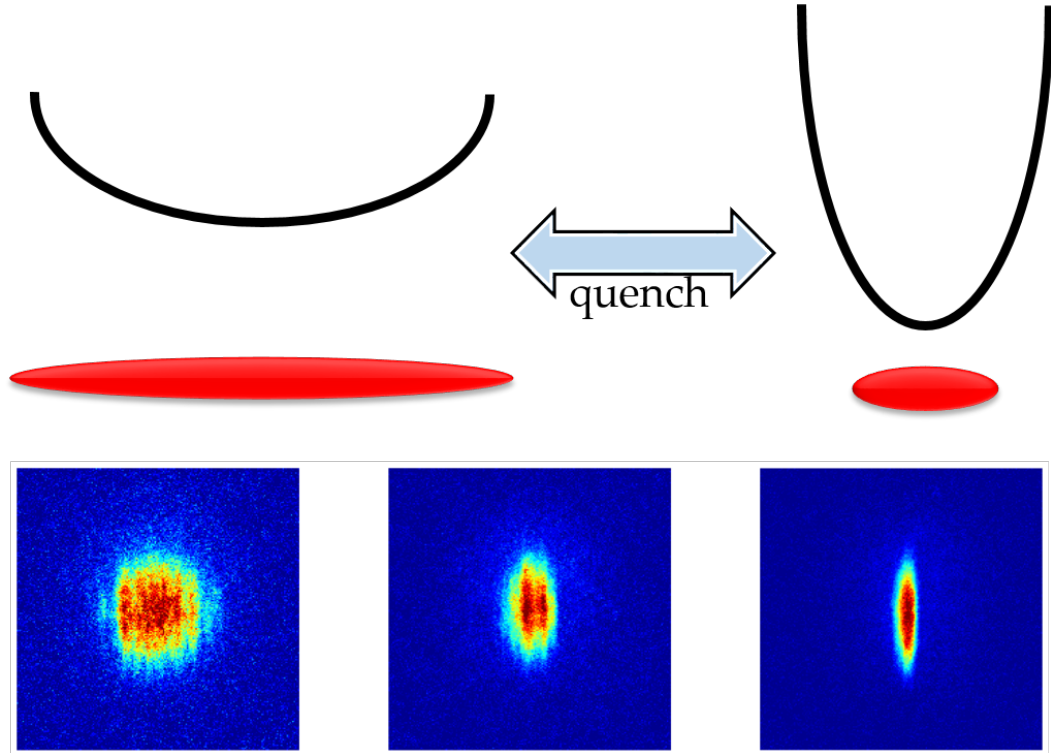
FIGURE 5.1: (Top) Dimensional quench concept, rapidly changing the to potential to change the dimensions of the system such that $\mu/\hbar\omega_\perp$ changes from <1 to >1 or vice versa. (Bottom) Preliminary results, so far we have been unable to perform the quench without exciting breathing mode oscillations, and it may not be possible to do so. Here, example optical density images are shown of the cloud through half an oscillation period.

Interesting questions can be asked within the context of breathing, like how the phase changes throughout an oscillation, does an originally phase fluctuating cloud become more coherent, and can the same be said for the reverse process? Does the phase coherence length change with time, and how fast can it respond? A similar experiment was performed in [184], they observed a scale invariant behaviour of the excitation spectrum, and a oscillatory time dependent temperature.
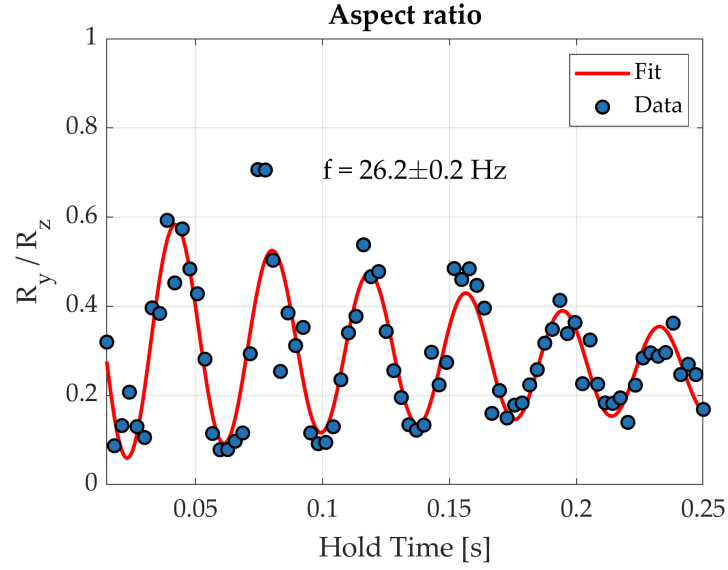
FIGURE 5.2: Excitation of the quadrupole breathing mode, in a trap of $\omega_\parallel = 2\pi \times 17.7\,\mathrm{Hz}$ and $\omega_\perp = 2\pi \times 800\,\mathrm{Hz}$. For a BEC in cigar shaped potential breathing oscillation frequency is $\omega_{\mathrm{BM}} = \sqrt{\frac{5}{2}}\omega_\parallel = 1.58\omega_\parallel$ [190], from our measurement we measure $\omega_{\mathrm{BM}}/\omega_\parallel \approx 1.47$. As of yet we are unsure of the source of the $6\,\%$ discrepancy.

Digital micro-mirror devices

The recent application of Digital Micro-mirror Devices (DMD) in ultracold atom experiments provided a new way of creating arbitrary potentials [129, 165, 166, 191, 192]. The DMD consists of an array of micron sized flip mirrors, that each have an on or off state, this allows for precise control of the optical potential, and has been used to counteract fragmentation effects [129], and even imprint artistic depictions of Bose and Einstein onto a condensate [165].

FIGURE 5.3: Image of a ViAIUX V-9501 DMD module [193], includes a Texes Instruments DLP9500 DMD chip [194]. 1080×1920 square mirrors of width $10.8\,\mu m$.

Use of this technology can give access to a wealth of new experiments due to the greater tuneability of potentials. For example one could use the DMD in to create box shaped potentials and investigate the crossover with clouds of homogeneous densities. It may provide a better way to perform a dimensional quench, for example by rapidly changing the length of the cloud by introducing a hard wall potential to cut off the edges (see Fig. 5.4). Using a box potential this could provide a direct way to investigate L/λ_T versus $\mu/\hbar\omega_\perp$, as the density would remain fixed after the quench and only L would change. This could prove an interesting way to refine the conclusions of our experiment.
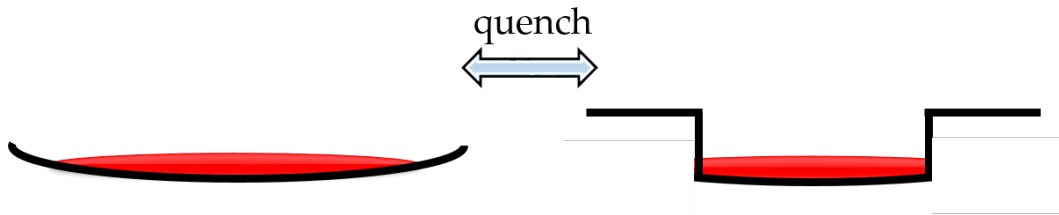
FIGURE 5.4: Alternative concept to perform a dimensional quench. The length of the system is suddenly changed by introduction of a hard wall potential.

Additional Experiments

Recently, we implemented RF dressing of potentials to manipulate the trapping potential and we are now attempting to create a triple-well potential. Our aim is to test the thought experiment outlined in [195], which suggests a method to test if "relative quantum phase" is transitive. If the phase difference $\Delta\phi$ between 2 of 3

isolated systems, A, B, and C, can be measured (i.e. $\Delta\phi_{AB} = \phi_A - \phi_B$ and $\Delta\phi_{BC} = \phi_B - \phi_C$) is the following relation true $\Delta\phi_{AC} = \Delta\phi_{AB} + \Delta\phi_{BC}$. Alternatively we could create a double-well potential [122, 196], and probe correlations in the gas by measuring the relative phase between two condensates along their axial direction. This analysis has been done in previous experiments which have used the double well to probe correlations in the equilibrium setting [173], and the non-equilibrium setting [197–199].

The Kibble-Zurek mechanism (KZM) [200, 201] is a theory that was devised to describe non-equilibrium dynamics after a spontaneous symmetry breaking phase transition and predicts the formation of topological defects. Originating in cosmology it was later proposed to occur in other scenarios including condensed matter systems [202]. The phenomenon has been observed in a number of ultracold atom experiments [203–206]. In the context of these ultracold atom experiments, an initially decoherent (thermal) gas is quenched through the critical temperature to a coherent state (BEC). The rapid quench prevents full coherence from being established, and the topological defects that arise are vortex filaments. An interesting measurement would be to observe the behaviour in the crossover regime, where the final equilibrium state is not totally coherent (BEC) but only partially coherent (quasi-condensate). Another interesting question that could be investigated is whether the KZM would occur in a dimensional quench from 1D to 3D?

Generalised hydrodynamics is a theory that recently emerged [207, 208] to explain non-equilibrium dynamics of integrable systems. It can be seen a dynamical extension to the Yang-Yang model, however in contrast to the conventional hydrodynamic (CHD) approach it does not assume local thermal equilibrium [97]. It has been shown to successfully predict the dynamical evolution of density in expansion [97] where CHD fails. Recently this model was extended to the dimensional crossover regime ($\mu/\hbar\omega_\perp \ll 1$, $k_B T/\hbar\omega_\perp \sim 1$) [209] and gave good agreement with an experiment [210]. However, this is a thermally driven dimensional crossover ($k_B T/\hbar\omega_\perp \gtrsim 1$), and as we have observed in our measurements the chemical crossover may more important, it would be interesting to see if it can be used to predict the evolution in a chemically driven crossover ($\mu/\hbar\omega_\perp \gtrsim 1$).

The experiment reported in this thesis has performed a thorough characterisation of the phase coherence in the 1D-3D crossover - in equilibrium. However, the experimental set-up developed is also well suited to study quantum many-body systems out-of-equilibrium, its application may shed light on other fundamental questions.

"Tempus edax rerum. Time, the devourer of all things." — OVID, Metamorphoses, XV. 234

Appendix A

1D-3D crossover regime - supplementary material

A.1 Measurements

In this section I include supplementary analysis of the data reported in Section 4.2.2. Figure A.1 plots the peak position $q_1^{\max}$ against the additional "1D parameters" that are not shown in Fig. 4.20a.
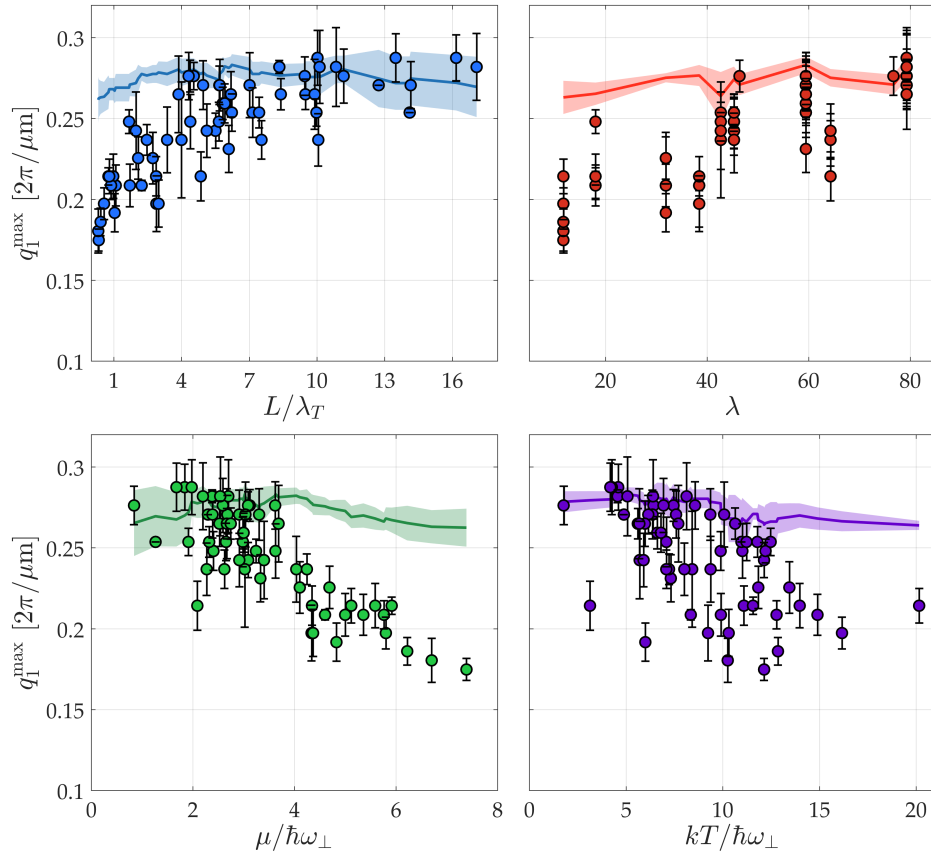

FIGURE A.1: "1D parameters" versus peak position $q_1^{\max}$. Dots indicate experimental measurements, and the errorbars come from the statistical uncertainty. The solid lines are the moving mean of the predictions from the OU+ model, and the shaded area indicates the corresponding moving standard deviation.

As discussed in Section 4.2.2 $q_1^{\max}$ is mainly effected by interactions. Here, the shift of $q_1^{\max}$ is related to an increase in t_{hydro}, and is indirectly related to the "3D end" of the parameter space (low L/λ_T and λ, and high $\mu/\hbar\omega_\perp$ and $k_B T/\hbar\omega_\perp$). This is qualitatively reproduced in the data.
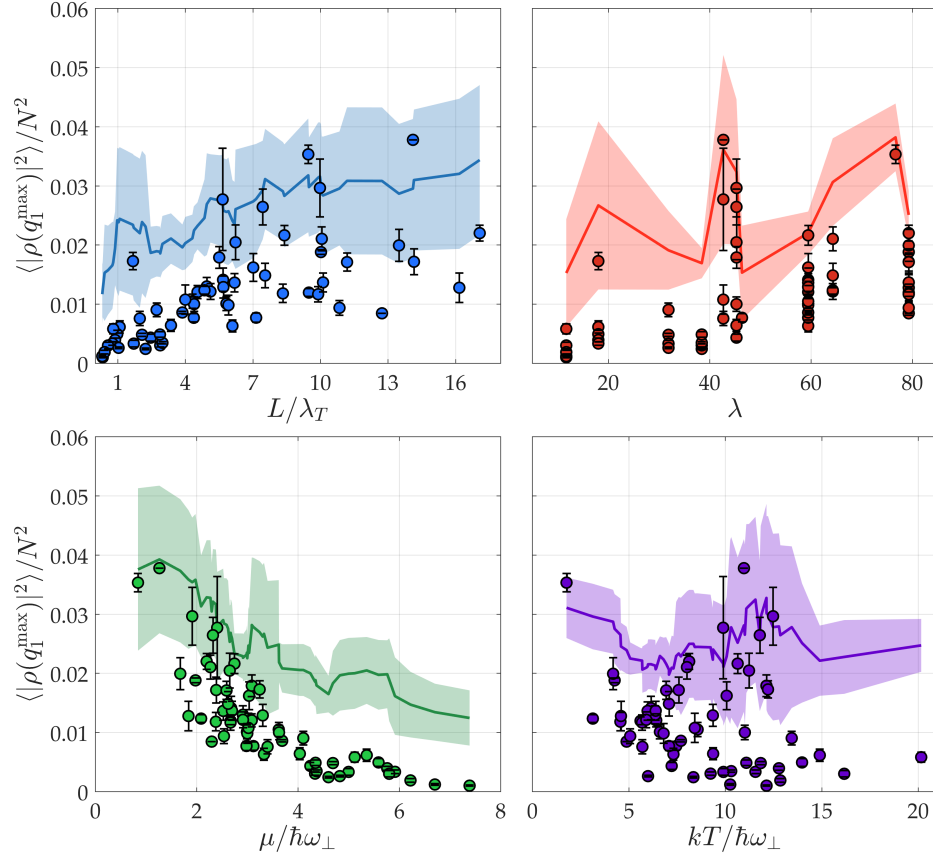
FIGURE A.2: "1D parameters" versus peak amplitude $\langle|\tilde{\rho}(q_1^{\max})|^2\rangle/N^2$. Dots indicate experimental measurements, and the errorbars come from the statistical uncertainty. The solid lines are the moving mean from the predictions of the OU+ model, and the shaded area indicates the corresponding moving standard deviation.

Another parameter that can be used to evaluate the strength of the fluctuations is the peak amplitude $\langle|\tilde{\rho}(q_1^{\max})|^2\rangle/N^2$. In the main text we choose $\tilde{g}^{(2)}(0)$ because this has a better signal to noise, as the parameter is an average over more points. However, we believe it gives similar information on the size of the density fluctuations. The usual 1D parameters are plotted against the peak amplitude in Fig. A.2, which reproduces the same trends that can be seen in Figs. 4.22 and 4.23 where $\tilde{g}^{(2)}(0)$ has been used.

A.2 Simulations

In this section I have included some supporting figures for the Section 4.1 of the main text.
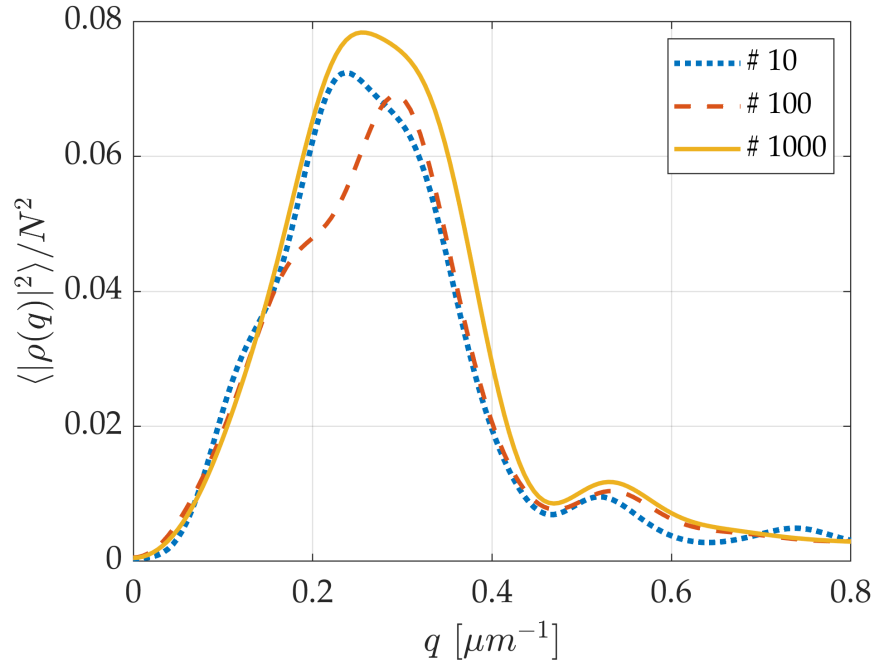
FIGURE A.3: Power spectrum of the density ripples $\langle|\tilde{\rho}(q)|^2\rangle/N^2$ generated by the Dettmer model Section 4.1.3, for a varying number of realisations 10 (blue, dotted), 100 (red, dashed), and 1000 (yellow, solid). Cloud parameters $(\omega_\perp, \omega_\parallel) = 2\pi \times 1235\,\text{Hz}$ and $16.1\,\text{Hz}$, $N = 6.7 \times 10^3$ $\mu/\hbar\omega_\perp = 0.87$.

Figure A.3 shows how the mean power spectrum varies with different number of realisations. Due to the random number generation of density ripples, a low number of realisations can make the mean appear distorted in comparison to the power spectrum obtained from the analytical result of the LDA Section 4.1.2.

Appendix B

Publications

An Environmental Monitoring Network for Quantum Gas Experiments and Devices
T. J. Barrett, W. Evans, A. Gadge, S. Bhumbra, S. Sleegers, R. Shah, J. Fekete, F. Oručević, and P. Krüger
arXiv:2101.12726 **[quant-ph]**
* Submitted to Quantum Science and Technology - 29/01/2021

Phase fluctuations in the 1D-3D crossover
R. Shah, T. J. Barrett, A. Colcelli, F. Oručević, A. Trombettoni, and P. Krüger
* In preparation

Bibliography

[1] H. Bethe. "Zur Theorie der Metalle". *Zeitschrift fur Physik* **71** (1931), pp. 205–226.

[2] M. H. Anderson et al. "Observation of Bose-Einstein Condensation in a Dilute Atomic Vapor". *Science* **269** (1995), pp. 198–201.

[3] K. B. Davis et al. "Bose-Einstein Condensation in a Gas of Sodium Atoms". *Phys. Rev. Lett.* **75** (1995), pp. 3969–3973.

[4] C. C. Bradley et al. "Evidence of Bose-Einstein Condensation in an Atomic Gas with Attractive Interactions". *Phys. Rev. Lett.* **75** (1995), pp. 1687–1690.

[5] A. Görlitz et al. "Realization of Bose-Einstein Condensates in Lower Dimensions". *Phys. Rev. Lett.* **87** (2001), p. 130402.

[6] D. Rychtarik et al. "Two-Dimensional Bose-Einstein Condensate in an Optical Surface Trap". *Phys. Rev. Lett.* **92** (2004), p. 173003.

[7] S. Stock et al. "Observation of Phase Defects in Quasi-Two-Dimensional Bose-Einstein Condensates". *Phys. Rev. Lett.* **95** (2005), p. 190403.

[8] N. L. Smith et al. "Quasi-2D confinement of a BEC in a combined optical and magnetic potential". *Journal of Physics B Atomic Molecular Physics* **38** (2005), pp. 223–235.

[9] T. Kinoshita, T. Wenger, and D. S. Weiss. "Observation of a One-Dimensional Tonks-Girardeau Gas". *Science* **305** (2004), pp. 1125–1128.

[10] B. Paredes et al. "Tonks-Girardeau gas of ultracold atoms in an optical lattice". *Nature* **429** (2004), pp. 277–81.

[11] M. Greiner et al. "Exploring Phase Coherence in a 2D Lattice of Bose-Einstein Condensates". *Phys. Rev. Lett.* **87** (2001), p. 160405.

[12] F. Schreck et al. "Quasipure Bose-Einstein Condensate Immersed in a Fermi Sea". *Phys. Rev. Lett.* **87** (2001), p. 080403.

[13] I. Shvarchuck et al. "Bose-Einstein Condensation into Nonequilibrium States Studied by Condensate Focusing". *Phys. Rev. Lett.* **89** (2002), p. 270404.

[14] D.S. Petrov, D.M. Gangardt, and G.V. Shlyapnikov. "Low-dimensional trapped gases". *J. Phys. IV France* **116** (2004), pp. 5–44.

[15] J. M. Kosterlitz and D. J. Thouless. "Ordering, metastability and phase transitions in two-dimensional systems". *Journal of Physics C Solid State Physics* **6** (1973), pp. 1181–1203.

[16] D. S. Petrov, G. V. Shlyapnikov, and J. T. M. Walraven. "Regimes of Quantum Degeneracy in Trapped 1D Gases". *Phys. Rev. Lett.* **85** (2000), pp. 3745–3749.

[17] T. T. Saraiva et al. "Multiband Material with a Quasi-1D Band as a Robust High-Temperature Superconductor". *Phys. Rev. Lett.* **125** (2020), p. 217003.

[18] M. Uhlmann, Y. Xu, and R. Schützhold. "Aspects of cosmic inflation in expanding Bose-Einstein condensates". *New Journal of Physics* **7** (2005), pp. 248–248.

[19] C.-L. Hung, V. Gurarie, and C. Chin. "From Cosmology to Cold Atoms: Observation of Sakharov Oscillations in a Quenched Atomic Superfluid". *Science* **341** (2013), pp. 1213–1215.

[20] R. Folman et al. "Controlling Cold Atoms using Nanofabricated Surfaces: Atom Chips". *Phys. Rev. Lett.* **84** (2000), pp. 4749–4752.

[21] E. H. Lieb and W. Liniger. "Exact Analysis of an Interacting Bose Gas. I. The General Solution and the Ground State". *Phys. Rev.* **130** (1963), pp. 1605–1616.

[22] E. H. Lieb. "Exact Analysis of an Interacting Bose Gas. II. The Excitation Spectrum". *Phys. Rev.* **130** (1963), pp. 1616–1624.

[23] M. Girardeau. "Relationship between Systems of Impenetrable Bosons and Fermions in One Dimension". *Journal of Mathematical Physics* **1** (1960), pp. 516–523.

[24] C. N. Yang and C. P. Yang. "Thermodynamics of a One-Dimensional System of Bosons with Repulsive Delta-Function Interaction". *Journal of Mathematical Physics* **10** (1969), pp. 1115–1122.

[25] A. H. van Amerongen et al. "Yang-Yang Thermodynamics on an Atom Chip". *Phys. Rev. Lett.* **100** (2008), p. 090402.

[26] T. Jacqmin et al. "Sub-Poissonian Fluctuations in a 1D Bose Gas: From the Quantum Quasicondensate to the Strongly Interacting Regime". *Phys. Rev. Lett.* **106** (2011), p. 230405.

[27] T. Jacqmin et al. "Momentum distribution of 1D Bose gases at the quasi-condensation crossover: theoretical and experimental investigation". *Physical Review A* **86** (2012).

[28] J. Armijo et al. "Mapping out the quasicondensate transition through the dimensional crossover from one to three dimensions". *Phys. Rev. A* **83** (2011), p. 021605.

[29] J. W. Kane and L. P. Kadanoff. "Long-Range Order in Superfluid Helium". *Phys. Rev.* **155** (1967), pp. 80–83.

[30] L. Reatto and G. V. Chester. "Phonons and the Properties of a Bose System". *Phys. Rev.* **155** (1967), pp. 88–100.

[31] D. S. Petrov, G. V. Shlyapnikov, and J. T. M. Walraven. "Phase-Fluctuating 3D Bose-Einstein Condensates in Elongated Traps". *Phys. Rev. Lett.* **87** (2001), p. 050404.

[32] S. Dettmer et al. "Observation of Phase Fluctuations in Elongated Bose-Einstein Condensates". *Phys. Rev. Lett.* **87** (2001), p. 160406.

[33] D. Hellweg et al. "Phase fluctuations in Bose–Einstein condensates". *Applied Physics B* **73** (2001), pp. 781–789.

[34] D. Hellweg et al. "Measurement of the Spatial Correlation Function of Phase Fluctuating Bose-Einstein Condensates". *Phys. Rev. Lett.* **91** (2003), p. 010406.

[35] H. Kreutzmann et al. "Characterization and control of phase fluctuations in elongated Bose–Einstein condensates". *Applied Physics B* **76** (2003), pp. 165–172.

[36] S. Richard et al. "Momentum Spectroscopy of 1D Phase Fluctuations in Bose-Einstein Condensates". *Phys. Rev. Lett.* **91** (2003), p. 010405.

[37] M. Hugbart et al. "Coherence length of an elongated condensate". *The European Physical Journal D - Atomic, Molecular, Optical and Plasma Physics* **35** (2005), pp. 155–163.

[38] T. Barrett. "An Apparatus for the Production of Bose-Einstein Condensates in Tunable Geometries on a Chip". PhD thesis. Univeristy of Nottingham, 2017.

[39] W. Evans. "On the use of additive manufacturing for atom trapping components in quantum technologies". PhD thesis. Univeristy of Sussex, 2020.

[40] W. D. Phillips and H. Metcalf. "Laser Deceleration of an Atomic Beam". *Phys. Rev. Lett.* **48** (1982), pp. 596–599.

[41] S. Chu et al. "Three-dimensional viscous confinement and cooling of atoms by resonance radiation pressure". *Phys. Rev. Lett.* **55** (1985), pp. 48–51.

[42] C. Foot, C. Foot, and D. Foot. *Atomic Physics*. Oxford Master Series in Physics. OUP Oxford, 2005.

[43] H. J. Metcalf and P. van der Straten. "Laser Cooling and Trapping of Neutral Atoms". *The Optics Encyclopedia*. American Cancer Society, 2007.

[44] D. A. Steck. *Rubidium 87 D Line Data*. (2001). URL: http://steck.us/alkalidata (visited on 09/06/2016).

[45] C. Pethick and H. Smith. *Bose–Einstein Condensation in Dilute Gases*. Cambridge University Press, 2008.

[46] R. Folman et al. "Microscopic Atom Optics: From Wires to an Atom Chip". *Advances in Atomic, Molecular, and Optical Physics* **48** (2002), p. 263.

[47] W. H. Wing. "On neutral particle trapping in quasistatic electromagnetic fields". *Progress in Quantum Electronics* **8** (1984), pp. 181–199.

[48] E. Majorana. "Atomi orientati in campo magnetico variabile". *Il Nuovo Cimento (1924-1942)* **9** (1932), pp. 43–50.

[49] D. E. Pritchard. "Cooling Neutral Atoms in a Magnetic Trap for Precision Spectroscopy". *Phys. Rev. Lett.* **51** (1983), pp. 1336–1339.

[50] J. Reichel. "Microchip traps and Bose–Einstein condensation". *Applied Physics B* **74** (2002), pp. 469–487.

[51] J. D. Weinstein and K. G. Libbrecht. "Microscopic magnetic traps for neutral atoms". *Phys. Rev. A* **52** (1995), pp. 4004–4009.

[52] J. Fortagh et al. "Miniaturized Wire Trap for Neutral Atoms". *Phys. Rev. Lett.* **81** (1998), pp. 5310–5313.

[53] J. Denschlag, D. Cassettari, and J. Schmiedmayer. "Guiding Neutral Atoms with a Wire". *Phys. Rev. Lett.* **82** (1999), pp. 2014–2017.

[54] J. Reichel, W. Hänsel, and T. W. Hänsch. "Atomic Micromanipulation with Magnetic Surface Traps". *Phys. Rev. Lett.* **83** (1999), pp. 3398–3401.

[55] J. Fortágh et al. "Surface effects in magnetic microtraps". *Phys. Rev. A* **66** (2002), p. 041604.

[56] S. Groth et al. "Atom Chips: Fabrication and Thermal Properties". *Applied Physics Letters* **85** (2004), p. 2980.

[57] P. Krüger et al. "Potential roughness near lithographically fabricated atom chips". *Phys. Rev. A* **76** (2007), p. 063621.

[58] S. Wildermuth et al. "Optimized magneto-optical trap for experiments with ultracold atoms near surfaces". *Phys. Rev. A* **69** (2004), p. 030901.

[59] J. H. Thywissen et al. "Microfabricated magnetic waveguides for neutral atoms". *The European Physical Journal D - Atomic, Molecular, Optical and Plasma Physics* **7** (1999), pp. 361–367.

[60] W. Hänsel et al. "Magnetic Conveyor Belt for Transporting and Merging Trapped Atom Clouds". *Phys. Rev. Lett.* **86** (2001), pp. 608–611.

[61] P Hommelhoff et al. "Transporting, splitting and merging of atomic ensembles in a chip trap". *New Journal of Physics* **7** (2005), pp. 3–3.

[62] A. Günther et al. "Combined chips for atom optics". *Phys. Rev. A* **71** (2005), p. 063619.

[63] W. Ketterle, D. S. Durfee, and D. M. Stamper-Kurn. "Making, probing and understanding Bose-Einstein condensates". *arXiv e-prints*, cond-mat/9904034 (1999), cond–mat/9904034.

[64] O. J. Luiten, M. W. Reynolds, and J. T. M. Walraven. "Kinetic theory of the evaporative cooling of a trapped gas". *Phys. Rev. A* **53** (1996), pp. 381–389.

[65] W. Ketterle and N. V. Druten. "Evaporative Cooling of Trapped Atoms". Ed. by B. Bederson and H. Walther. Vol. 37. Advances In Atomic, Molecular, and Optical Physics. Academic Press, 1996, pp. 181–236.

[66] D. W. Snoke and J. P. Wolfe. "Population dynamics of a Bose gas near saturation". *Phys. Rev. B* **39** (1989), pp. 4030–4037.

[67] F. Dalfovo et al. "Theory of Bose-Einstein condensation in trapped gases". *Rev. Mod. Phys.* **71** (1999), pp. 463–512.

[68] F. Gerbier et al. "Experimental study of the thermodynamics of an interacting trapped Bose-Einstein condensed gas". *Phys. Rev. A* **70** (2004), p. 013607.

[69] C. N. Yang. "Concept of Off-Diagonal Long-Range Order and the Quantum Phases of Liquid He and of Superconductors". *Rev. Mod. Phys.* **34** (1962), pp. 694–704.

[70] P. C. Hohenberg. "Existence of Long-Range Order in One and Two Dimensions". *Phys. Rev.* **158** (1967), pp. 383–386.

[71] R. J. Glauber. "Photon Correlations". *Phys. Rev. Lett.* **10** (1963), pp. 84–86.

[72] R. J. Glauber. "The Quantum Theory of Optical Coherence". *Phys. Rev.* **130** (1963), pp. 2529–2539.

[73] R. J. Glauber. "Coherent and Incoherent States of the Radiation Field". *Phys. Rev.* **131** (1963), pp. 2766–2788.

[74] M. Naraschewski et al. "Interference of Bose condensates". *Phys. Rev. A* **54** (1996), pp. 2185–2196.

[75] M. Naraschewski and R. J. Glauber. "Spatial coherence and density correlations of trapped Bose gases". *Phys. Rev. A* **59** (1999), pp. 4595–4607.

[76] R. H. Brown and R. Twiss. "LXXIV. A new type of interferometer for use in radio astronomy". *The London, Edinburgh, and Dublin Philosophical Magazine and Journal of Science* **45** (1954), pp. 663–682.

[77] R. H. Brown and R. Q. Twiss. "Correlation between Photons in two Coherent Beams of Light". *Nature* **177** (1956), pp. 27–29.

[78] R. Hanbury Brown and R. Q. Twiss. "A Test of a New Type of Stellar Interferometer on Sirius". *Nature* **178** (1956), pp. 1046–1048.

[79] M. Schellekens et al. "Hanbury Brown Twiss Effect for Ultracold Quantum Gases". *Science* **310** (2005), pp. 648–651.

[80] R. J. Dodd et al. "Characterizing the coherence of Bose-Einstein condensates and atom lasers". *Opt. Express* **1** (1997), pp. 284–292.

[81] M. Olshanii. "Atomic Scattering in the Presence of an External Confinement and a Gas of Impenetrable Bosons". *Phys. Rev. Lett.* **81** (1998), pp. 938–941.

[82] C. Menotti and S. Stringari. "Collective oscillations of a one-dimensional trapped Bose-Einstein gas". *Phys. Rev. A* **66** (2002), p. 043610.

[83] Gerbier, F. "Quasi-1D Bose-Einstein condensates in the dimensional crossover regime". *Europhys. Lett.* **66** (2004), pp. 771–777.

[84] I. Bouchoule, N. J. V. Druten, and C. I. Westbrook. *Atom chips and one-dimensional Bose gases*. 2009.

[85] N. D. Mermin and H. Wagner. "Absence of Ferromagnetism or Antiferromagnetism in One- or Two-Dimensional Isotropic Heisenberg Models". *Phys. Rev. Lett.* **17** (1966), pp. 1133–1136.

[86] K. V. Kheruntsyan et al. "Pair Correlations in a Finite-Temperature 1D Bose Gas". *Phys. Rev. Lett.* **91** (2003), p. 040403.

[87] C. Mora and Y. Castin. "Extension of Bogoliubov theory to quasicondensates". *Phys. Rev. A* **67** (2003), p. 053615.

[88] Y. Castin. "Simple theoretical tools for low dimension Bose gases". *J. Phys. IV France* **116** (2004), pp. 89–132.

[89] T. Jacqmin. "Probing correlations in a one-dimensional gas of bosons on an atom chip". PhD thesis. Université Paris Sud, 2012.

[90] J. V. Gomes et al. "Theory for a Hanbury Brown Twiss experiment with a ballistically expanding cloud of cold atoms". *Phys. Rev. A* **74** (2006), p. 053607.

[91] R. G. Dall et al. "Observation of atomic speckle and Hanbury Brown–Twiss correlations in guided matter waves". *Nature Communications* **2** (2011), p. 291.

[92] P. E. S. Tavares et al. "Matter wave speckle observed in an out-of-equilibrium quantum fluid". *Proceedings of the National Academy of Sciences* **114** (2017), pp. 12691–12695.

[93] A. Imambekov et al. "Density ripples in expanding low-dimensional gases as a probe of correlations". *Phys. Rev. A* **80** (2009), p. 033604.

[94] S. Manz et al. "Two-point density correlations of quasicondensates in free expansion". *Physical Review A* **81** (2010), p. 031610.

[95] M. Schemmer and I. Bouchoule. "Cooling a Bose Gas by Three-Body Losses". *Phys. Rev. Lett.* **121** (2018), p. 200401.

[96] M. Schemmer, A. Johnson, and I. Bouchoule. "Monitoring squeezed collective modes of a one-dimensional Bose gas after an interaction quench using density-ripple analysis". *Phys. Rev. A* **98** (2018), p. 043604.

[97] M. Schemmer et al. "Generalized Hydrodynamics on an Atom Chip". *Phys. Rev. Lett.* **122** (2019), p. 090601.

[98] S. W. Seo, J.-y. Choi, and Y.-i. Shin. "Scaling behavior of density fluctuations in an expanding quasi-two-dimensional degenerate Bose gas". *Phys. Rev. A* **89** (2014), p. 043606.

[99]   T. James. "Tools and fundamental techniques for Bose-Einstein condensate microscopy". PhD thesis. Univeristy of Sussex, 2019.

[100]   J. H. Shirley. "Modulation transfer processes in optical heterodyne saturation spectroscopy". *Opt. Lett.* **7** (1982), pp. 537–539.

[101]   R. Valenzuela et al. "Frequency stabilisation of AlGaAs lasers to absorption spectrum of rubidium using Zeeman effect". English. *Electronics Letters* **24** (1988), 725–726(1).

[102]   C. P. Pearman et al. "Polarization spectroscopy of a closed atomic transition : applications to laser frequency locking." *Journal of physics B : atomic, molecular and optical physics.* **35** (2002), pp. 5141–5151.

[103]   G. C. Bjorklund et al. "Frequency modulation (FM) spectroscopy". *Applied Physics B: Lasers and Optics* **32** (1983), pp. 145–152.

[104]   D. W. Preston. "Doppler-free saturated absorption: Laser spectroscopy". *American Journal of Physics* **64** (1996), pp. 1432–1436.

[105]   J. Kellogg et al. "A compact high-efficiency cold atom beam source". *Applied Physics B* **109** (2011).

[106]   N. Castagna et al. "A novel simplified two-dimensional magneto-optical trap as an intense source of slow cesium atoms". *http://dx.doi.org/10.1051/epjap:2006037* **34** (2006).

[107]   S. Kulas et al. "Miniaturized Lab System for Future Cold Atom Experiments in Microgravity". *Microgravity Science and Technology* **29** (2017), pp. 37–48.

[108]   S. Bourdeauducq et al. "ARTIQ 1.0". *Zenodo. 10.5281/ zenodo.51303.* (2016).

[109]   *Sinara core*. `https://m-labs.hk/experiment-control/sinara-core/`. Accessed: 2021-01-27.

[110]   *InfluxData Inc., InfluxDB: Purpose-Built Open Source Time Series Database*. `https://www.influxdata.com/`. Accessed: 2021-04-27.

[111]   *Grafana Labs, Grafana: The Open Observability Platform*. `https://grafana.com`. Accessed: 2021-04-27.

[112]   T. J. Barrett et al. *An Environmental Monitoring Network for Quantum Gas Experiments and Devices*. 2021.

[113]   F. Sarvar, N. J. Poole, and P. A. Witting. "PCB glass-fibre laminates: Thermal conductivity measurements and their effect on simulation". *Journal of Electronic Materials* **19** (1990), pp. 1345–1350.

[114]   *Rogers   4000   series*. `https : / / rogerscorp . com / advanced – connectivity – solutions / ro4000 – series – laminates / ro4003c – laminates`. Accessed: 2021-02-01.

[115]   *Aluminium Nitride properties*. https://accuratus.com/alumni.html. Accessed: 2021-02-01.

[116]   *Thermal Conductivity of Metals, Metallic Elements and Alloys*. https://www.engineeringtoolbox.com/thermal-conductivity-metals-d_858.html. Accessed: 2021-02-01.

[117]   *Resistivity and Conductivity - Temperature Coefficients for Common Materials*. https://www.engineeringtoolbox.com/resistivity-conductivity-d_418.html. Accessed: 2021-03-15.

[118]   B. Lev. "Fabrication of micro-magnetic traps for cold neutral atoms". *Quantum Inf. Comput.* **3** (2003), pp. 450–464.

[119]   S. Du et al. "Atom-chip Bose-Einstein condensation in a portable vacuum cell". *Phys. Rev. A* **70** (2004), p. 053606.

[120]   Y. Hui et al. "Directly Trapping Atoms in a U-Shaped Magneto-Optical Trap Using a Mini Atom Chip". *Chinese Physics Letters* **25** (2008), pp. 3219–3222.

[121]   J. Armijo, C. Alzar, and I. Bouchoule. "Thermal properties of AlN-based atom chips". *Eur. Phys. J. D.* **56** (2009), pp. 33–39.

[122]   T. Schumm et al. "Matter-wave interferometry in a double well on an atom chip". *Nature Physics* **1** (2005), pp. 57–62.

[123]   A. E. Leanhardt et al. "Propagation of Bose-Einstein Condensates in a Magnetic Waveguide". *Phys. Rev. Lett.* **89** (2002), p. 040401.

[124]   A. E. Leanhardt et al. "Bose-Einstein Condensates near a Microfabricated Surface". *Phys. Rev. Lett.* **90** (2003), p. 100404.

[125]   S Kraft et al. "Anomalous longitudinal magnetic field near the surface of copper conductors". *Journal of Physics B: Atomic, Molecular and Optical Physics* **35** (2002), pp. L469–L474.

[126]   J. Estève et al. "Role of wire imperfections in micromagnetic traps for atoms". *Phys. Rev. A* **70** (2004), p. 043629.

[127]   J.-B. Trebbia et al. "Roughness Suppression via Rapid Current Modulation on an Atom Chip". *Phys. Rev. Lett.* **98** (2007), p. 263201.

[128]   I. Bouchoule, J.-B. Trebbia, and C. L. Garrido Alzar. "Limitations of the modulation method to smooth wire-guide roughness". *Phys. Rev. A* **77** (2008), p. 023624.

[129]   M. Tajik. et al. "Designing arbitrary one-dimensional potentials on an atom chip". *Opt. Express* **27** (2019), pp. 33474–33487.

[130]   P. Krüger et al. "Cold atoms close to surfaces: measuring magnetic field roughness and disorder potentials". *J. Phys.: Conf. Ser. 19 009* (2005).

[131]   S. Wildermuth et al. "Microscopic magnetic-field imaging". *Nature* **435** (2005), pp. 440–440.

[132] M. Vengalattore et al. "High-Resolution Magnetometry with a Spinor Bose-Einstein Condensate". *Phys. Rev. Lett.* **98** (2007), p. 200801.

[133] F. Yang et al. "Scanning Quantum Cryogenic Atom Microscope". *Phys. Rev. Applied* **7** (2017), p. 034026.

[134] F. Yang et al. "Nematic transitions in iron pnictide superconductors imaged with a quantum gas". *Nature Physics* **16** (2020), pp. 514–519.

[135] G Reinaudi et al. "Strong saturation absorption imaging of dense clouds of ultracold atoms". *Optics letters* **32** (2007), pp. 3143–5.

[136] M. Kristensen. "Atom number fluctuations in Bose-Einstein condensates". PhD thesis. Univeristy of Aarhus, 2018.

[137] J. Chabé et al. "Coherent and incoherent multiple scattering". *Phys. Rev. A* **89** (2014), p. 043833.

[138] C. Ockeloen-Korppi et al. "Detection of small atom numbers through image processing". *Physical Review A* **82** (2010), p. 061606.

[139] L. Sirovich and M. Kirby. "Low-dimensional procedure for the characterization of human faces". *J. Opt. Soc. Am. A* **4** (1987), pp. 519–524.

[140] V. Dunjko, V. Lorent, and M. Olshanii. "Bosons in Cigar-Shaped Traps: Thomas-Fermi Regime, Tonks-Girardeau Regime, and In Between". *Phys. Rev. Lett.* **86** (2001), pp. 5413–5416.

[141] L. Salasnich, A. Parola, and L. Reatto. "Effective wave equations for the dynamics of cigar-shaped and disk-shaped Bose condensates". *Phys. Rev. A* **65** (2002), p. 043614.

[142] P. Krüger et al. "Weakly Interacting Bose Gas in the One-Dimensional Limit". *Phys. Rev. Lett.* **105** (2010), p. 265302.

[143] I. Shvarchuck et al. "Hydrodynamic behavior in expanding thermal clouds of ^{87}Rb". *Phys. Rev. A* **68** (2003), p. 063603.

[144] F. Gerbier et al. "Critical Temperature of a Trapped, Weakly Interacting Bose Gas". *Phys. Rev. Lett.* **92** (2004), p. 030405.

[145] M. Schemmer. "Out-of-equilibrium dynamics in 1D Bose gases". PhD thesis. Université Paris-Saclay, 2019.

[146] E. A. Salim et al. "High resolution imaging and optical control of Bose-Einstein condensates in an atom chip magnetic trap". *Applied Physics Letters* **102** (2013), p. 084104.

[147] D. Adu Smith et al. "Absorption Imaging of Ultracold Atoms on Atom Chips". *Optics express* **19** (2011), pp. 8471–85.

[148] T. Ottenstein. "A New Objective for High Resolution Imaging of Bose-Einstein Condensates". PhD thesis. Univeristy of Heidelberg, 2006.

[149] "Lenses and Geometrical Optics". *Fundamentals of Light Microscopy and Electronic Imaging*. John Wiley & Sons, Ltd, 2012. Chap. 4, pp. 53–77.

[150] C.-L. Hung and C. Chin. "<italic>In Situ</italic> Imaging of Atomic Quantum Gases". *Quantum Gas Experiments*. Chap. Chapter 6, pp. 101–120.

[151] A. Lahiri. "Chapter 6 - Fourier Optics". *Basic Optics*. Ed. by A. Lahiri. Amsterdam: Elsevier, 2016, pp. 539–603.

[152] A. Putra et al. "Optimally focused cold atom systems obtained using density-density correlations". *Review of Scientific Instruments* **85** (2014), p. 013110.

[153] H. C. W. Beijerinck. "Heating rates in collisionally opaque alkali-metal atom traps: Role of secondary collisions". *Phys. Rev. A* **62** (2000), p. 063614.

[154] B. Merkel et al. "Magnetic field stabilization system for atomic physics experiments". *Review of Scientific Instruments* **90** (2019), p. 044702.

[155] H. Talbot. "LXXVI. Facts relating to optical science. No. IV". *The London, Edinburgh, and Dublin Philosophical Magazine and Journal of Science* **9** (1836), pp. 401–407.

[156] M. S. Chapman et al. "Near-field imaging of atom diffraction gratings: The atomic Talbot effect". *Phys. Rev. A* **51** (1995), R14–R17.

[157] L. Deng et al. "Temporal, Matter-Wave-Dispersion Talbot Effect". *Phys. Rev. Lett.* **83** (1999), pp. 5407–5411.

[158] M. Mark et al. "Demonstration of the temporal matter-wave Talbot effect for trapped matter waves". *New Journal of Physics - NEW J PHYS* **13** (2011).

[159] B. Santra et al. "Measuring finite-range phase coherence in an optical lattice using Talbot interferometry". *Nature Communications* **8** (2017), p. 15601.

[160] Y. Zhai et al. "Talbot-enhanced, maximum-visibility imaging of condensate interference". *Optica* **5** (2018), pp. 80–85.

[161] V. Makhalov and A. Turlapov. "Order in the Interference of a Long Chain of Bose Condensates with Unrestricted Phases". *Phys. Rev. Lett.* **122** (2019), p. 090403.

[162] I. E. Mazets. "Two-dimensional dynamics of expansion of a degenerate Bose gas". *Phys. Rev. A* **86** (2012), p. 055603.

[163] A. L. Gaunt et al. "Bose-Einstein Condensation of Atoms in a Uniform Potential". *Phys. Rev. Lett.* **110** (2013), p. 200406.

[164] L. Chomaz et al. "Emergence of coherence via transverse condensation in a uniform quasi-two-dimensional Bose gas". *Nature Communications* **6** (2015), p. 6162.

[165] G. Gauthier et al. "Direct imaging of a digital-micromirror device for configurable microscopic optical potentials". *Optica* **3** (2016), pp. 1136–1143.

[166] Y. Q. Zou et al. *Optical control of the density and spin spatial profiles of a planar Bose gas*. 2021.

[167] I. Bouchoule, M. Schemmer, and C. Noûs. "Asymptotic temperature of a lossy condensate". *SciPost Physics* **8** (2020).

[168] P. G. de Gennes. "Superconductivity of metals and alloys" (1966).

[169] T.-L. Ho and M. Ma. "Quasi 1 and 2d Dilute Bose Gas in Magnetic Traps: Existence of Off-Diagonal Order and Anomalous Quantum Fluctuations". *Journal of Low Temperature Physics* **115** (1999), pp. 61–70.

[170] H.-P. Stimming et al. "Fluctuations and Stochastic Processes in One-Dimensional Many-Body Quantum Systems". *Phys. Rev. Lett.* **105** (2010), p. 015301.

[171] T. Betz. "Phase correlations of coupled one-dimensional Bose gases". PhD thesis. TU Wien, 2011.

[172] S. Manz. "Density correlations of expanding one-dimensional Bose gases". PhD thesis. TU Wien, 2011.

[173] T. Betz et al. "Two-Point Phase Correlations of a One-Dimensional Bosonic Josephson Junction". *Phys. Rev. Lett.* **106** (2011), p. 020407.

[174] T. Langen et al. "Prethermalization in one-dimensional Bose gases: Description by a stochastic Ornstein-Uhlenbeck process". *The European Physical Journal Special Topics* **217** (2013), pp. 43–53.

[175] C. Gardiner. "Handbook of stochastic methods for physics, chemistry and the natural sciences, second edition". **25** (1986), p. 3145.

[176] G. E. Uhlenbeck and L. S. Ornstein. "On the Theory of the Brownian Motion". *Phys. Rev.* **36** (1930), pp. 823–841.

[177] M. Feit, J. Fleck, and A Steiger. "Solution of the Schrödinger equation by a spectral method". *Journal of Computational Physics* **47** (1982), pp. 412–433.

[178] H. T. C. Stoof. "Coherent Versus Incoherent Dynamics During Bose-Einstein Condensation in Atomic Gases". *Journal of Low Temperature Physics* **114** (1999), pp. 11–108.

[179] P. Blakie et al. "Dynamics and statistical mechanics of ultra-cold Bose gases using c-field techniques". *Advances in Physics* **57** (2008), pp. 363–455.

[180] S. P. Cockburn, D. Gallucci, and N. P. Proukakis. "Quantitative study of quasi-one-dimensional Bose gas experiments via the stochastic Gross-Pitaevskii equation". *Phys. Rev. A* **84** (2011), p. 023613.

[181] D. Gallucci, S. P. Cockburn, and N. P. Proukakis. "Phase coherence in quasicondensate experiments: An ab initio analysis via the stochastic Gross-Pitaevskii equation". *Phys. Rev. A* **86** (2012), p. 013627.

[182] S. J. Rooney, P. B. Blakie, and A. S. Bradley. "Stochastic projected Gross-Pitaevskii equation". *Phys. Rev. A* **86** (2012), p. 053634.

[183] Y. Castin and R. Dum. "Bose-Einstein Condensates in Time Dependent Traps". *Phys. Rev. Lett.* **77** (1996), pp. 5315–5319.

[184] W. Rohringer et al. "Non-equilibrium scale invariance and shortcuts to adiabaticity in a one-dimensional Bose gas". *Scientific Reports* **5** (2015), p. 9820.

[185] J.-B. Trebbia et al. "Experimental Evidence for the Breakdown of a Hartree-Fock Approach in a Weakly Interacting Bose Gas". *Phys. Rev. Lett.* **97** (2006), p. 250403.

[186] N. Wiener. "Generalized harmonic analysis". *Acta Mathematica* **55** (1930), pp. 117–258.

[187] A. Khintchine. "Korrelationstheorie der stationären stochastischen Prozesse". *Mathematische Annalen* **109** (1934), pp. 604–615.

[188] S. Hofferberth et al. "Non-equilibrium coherence dynamics in one-dimensional Bose gases". *Nature* **449** (2007), pp. 324–327.

[189] S. Stringari. "Collective Excitations of a Trapped Bose-Condensed Gas". *Phys. Rev. Lett.* **77** (1996), pp. 2360–2363.

[190] M.-O. Mewes et al. "Collective Excitations of a Bose-Einstein Condensate in a Magnetic Trap". *Phys. Rev. Lett.* **77** (1996), pp. 988–991.

[191] J. Liang et al. "1.5% root-mean-square flat-intensity laser beam formed using a binary-amplitude spatial light modulator". *Appl. Opt.* **48** (2009), pp. 1955–1962.

[192] P. Zupancic et al. "Ultra-precise holographic beam shaping for microscopic quantum control". *Opt. Express* **24** (2016), pp. 13881–13893.

[193] *Superspeed V Modules*. https://www.vialux.de/en/superspeed-v-modules.html. Accessed: 2021-04-23.

[194] *DLP9500 Product Details*. https://www.ti.com/product/https://www.ti.com/product/DLP9500. Accessed: 2021-04-23.

[195] A. J. Leggett. "Is "relative quantum phase" transitive?" *Foundations of Physics* **25** (1995), pp. 113–122.

[196] I. Lesanovsky et al. "Adiabatic radio-frequency potentials for the coherent manipulation of matter waves". *Phys. Rev. A* **73** (2006), p. 033619.

[197] B. Rauer et al. "Recurrences in an isolated quantum many-body system". *Science* **360** (2018), pp. 307–310.

[198] T. Langen et al. "Local emergence of thermal correlations in an isolated quantum many-body system". *Nature Physics* **9** (2013), pp. 640–643.

[199] M. Kuhnert et al. "Multimode Dynamics and Emergence of a Characteristic Length Scale in a One-Dimensional Quantum System". *Phys. Rev. Lett.* **110** (2013), p. 090405.

[200] T. W. B. Kibble. "Topology of cosmic domains and strings". *Journal of Physics A Mathematical General* **9** (1976), pp. 1387–1398.

[201] W. H. Zurek. "Cosmological experiments in superfluid helium?" *Nature* **317** (1985), pp. 505–508.

[202] A del Campo, T. W. B. Kibble, and W. H. Zurek. "Causality and non-equilibrium second-order phase transitions in inhomogeneous systems". *Journal of Physics: Condensed Matter* **25** (2013), p. 404210.

[203] S. Donadello et al. "Creation and counting of defects in a temperature-quenched Bose-Einstein condensate". *Phys. Rev. A* **94** (2016), p. 023628.

[204] B. Ko, J. W. Park, and Y. Shin. "Kibble–Zurek universality in a strongly interacting Fermi superfluid". *Nature Physics* **15** (2019), pp. 1227–1231.

[205] I.-K. Liu et al. "Dynamical equilibration across a quenched phase transition in a trapped quantum gas". *Communications Physics* **1** (2018), p. 24.

[206] I.-K. Liu et al. "Kibble-Zurek dynamics in a trapped ultracold Bose gas". *Phys. Rev. Research* **2** (2020), p. 033183.

[207] B. Bertini et al. "Transport in Out-of-Equilibrium XXZ Chains: Exact Profiles of Charges and Currents". *Phys. Rev. Lett.* **117** (2016), p. 207201.

[208] O. A. Castro-Alvaredo, B. Doyon, and T. Yoshimura. "Emergent Hydrodynamics in Integrable Quantum Systems Out of Equilibrium". *Phys. Rev. X* **6** (2016), p. 041065.

[209] F. Møller et al. "Extension of the Generalized Hydrodynamics to the Dimensional Crossover Regime". *Phys. Rev. Lett.* **126** (2021), p. 090602.

[210] C. Li et al. "Relaxation of Bosons in One Dimension and the Onset of Dimensional Crossover". *SciPost Phys.* **9** (2020), p. 58.